Australian National University

Epitaxial growth of III-V semiconductors on two-dimensional layered material substrates

Aswani Gopakumar Saraswathy Vilasam

June 2023

A Dissertation Submitted for the Degree of Doctor of Philosophy

of the Australian National University

Department of Electronic Materials Engineering

Research School of Physics

College of Science

The Australian National University

Declaration

I certify that this dissertation does not incorporate, without acknowledgement, any material previously submitted for a degree or diploma in any university and that to the best of my knowledge, it does not contain any material previously published or written by another person except where due reference is made in the text. The work in this dissertation is my own, except for the contributions made by others as described in the Acknowledgements.

Aswani Gopakumar Saraswathy Vilasam

June 2023

Acknowledgements

I am humbled by the invaluable support and guidance I have received throughout my research journey. I would like to express my sincerest appreciation to Prof. Hoe Tan and Prof. Chennupati Jagadish for their unwavering support, mentorship and scholarly expertise. Their dedication to academic excellence has played a pivotal role in shaping my research and fostering my intellectual growth. I am truly grateful for their guidance and encouragement, which have been invaluable to me.

I am also deeply grateful to the Australian National University (ANU) for providing exceptional research facilities and creating an outstanding working environment. The state-of-the-art laboratories, cutting-edge resources, and collaborative atmosphere at ANU have greatly contributed to the success of my research endeavours. The stimulating academic community at ANU has continuously motivated me to explore new horizons and pursue innovative approaches. I would like to extend my special thanks to Prof. Chennupati Jagadish, Prof. Hoe Tan, Prof. Tim Senden, Prof. Lan Fu, HDR convenor Ms. Liudmila Mangos, and the Canberra Innovation Network - Research to Impact program for their instrumental role in shaping my perspectives.

I am profoundly grateful for the funding support I have received from the Australian Government and the Australian Research Council. Their generous investment in the International PhD student scholarship has not only provided financial assistance but has also given me the necessary resources and opportunities to effectively carry out my research work. I am truly thankful for their belief in my academic pursuits and their contribution to my research journey.

I would also like to express my heartfelt gratitude to ANU for their support during the disruptive times of the COVID-19 pandemic. The scholarship extension provided by the university during this challenging period has been instrumental in enabling me to navigate the uncertainties and continue my research effectively. I am grateful for the understanding and flexibility demonstrated by the university, which has greatly eased the impact of the pandemic on my studies.

I am incredibly grateful to my fellow researchers, lab mates and colleagues who have provided unwavering support and collaboration throughout this journey. I extend my heartfelt thanks to Prof. Sudip Chakraborty and Mr. Ponnappa Kechagonda of Harishchandra Research Institute for their immense support in theoretical investigations. Additionally, I would like to express my deep appreciation to Assistant Prof. Xiaoming Yuan, Dr. Felipe Kremer, Dr. Zhe Li, Dr. Vidur Raj, Mr. Bikesh Gupta, Dr. Zahra Azimi, Dr. Julie Tournet, Dr. Naiyin Wang, Dr. Dipankar Chugh, Dr. Sonachand Adhikari, Dr. Li Li, Ms. Gayatri Vaidya, Dr. Mark Lockrey, Dr. Olivier Lee Cheong Lem, Dr. Kaushal Vora and Dr. Mykhaylo Lysevych for their valuable contributions. Their insightful discussions, constructive feedback and technical assistance have played a pivotal role in shaping my research and expanding my perspectives. The camaraderie and the exchange of ideas within this group have greatly enriched my research experience. I am truly grateful for the collaborative environment that fostered intellectual growth and encouraged innovative thinking. Their collective expertise and dedication have been invaluable in overcoming research challenges and achieving meaningful results. I am indebted to each of them for their support and for inspiring me to push the boundaries of knowledge in our field.

I would also like to acknowledge the immense mental support I have received from my supervisors and the Research School of Physics. Their unwavering support during the bush fires, hailstorm damage to the research facilities, and COVID-19 lockdowns has been invaluable. Their guidance, understanding, and encouragement have helped me overcome numerous challenges and maintain focus on my research goals. I am deeply grateful for their dedication and mentorship, which have provided me with the necessary stability and resilience to navigate these difficult times.

I am incredibly grateful for the opportunities I have been fortunate enough to encounter during my time in Canberra, the capital city of Australia. Working as a casual sessional academic, teaching and demonstrating physics and engineering courses has been a truly fulfilling experience. I have thoroughly enjoyed sharing my knowledge with students and witnessing their growth and development.

Participating in Innovation ANU and being part of the top ten teams has been a remarkable achievement. This experience has broadened my vision and compelled me

to think openly and collaboratively with individuals from diverse backgrounds. The Research to Impact fellowship from Canberra Innovation Network has provided me with valuable support and resources to pursue innovative approaches and turn research into tangible outcomes. This fellowship has encouraged me to think beyond the confines of academia and explore the practical applications of my research.

My internship at the science policy team at the Australian Academy of Science has been transformative. It has exposed me to a wide range of topics, including climate change sciences, science communication, and indigenous knowledge and practices. This experience has expanded my understanding and shaped my perspectives in profound ways. The opportunity to engage with experts in these fields has deepened my appreciation for the significance of science in policymaking and its impact on society.

I would like to extend my sincere gratitude to the Syenta (Spark-3D) team. During the time I was writing my thesis, I had the privilege of joining Syenta as a senior research and development engineer. Working alongside this highly motivated and innovative team has been an enriching experience.

I would like to express my appreciation to Dr. Jekaterina Viktorova and Prof. Luke Connal for providing me with the opportunity to be a part of Syenta. Their trust in my abilities and their belief in my potential have been instrumental in my professional growth and development.

I am grateful for the meaningful personal and professional connections I have formed with Dr. Zahra Azimi, Dr. Grishmi Rajbhandari, Ms. Ashleigh Ludwig, Mr. Tiger Chen, Mr. Andrew Simpson, Mr. Zach Dowse, Mr. Ben Wilkinson, Mr. Samuel Dietz, Mr. Duong Pham and Mr. Daniel de Waard. Each of them has contributed to my journey at Syenta, and I value the collaborative spirit and knowledge sharing that has thrived within our team. The dedication and expertise they bring to their work have inspired me to push boundaries and explore innovative solutions. Thank you, Syenta team, for making my experience with the company truly remarkable. Your passion, dedication and collaborative spirit have left a lasting impact on me, both personally and professionally. I am grateful for the opportunities, the friendships, and the knowledge I have gained during my time at Syenta.

I am deeply saddened to acknowledge the loss of several dear friends and family members during my PhD years. Their passing has had a profound impact on me, forcing me to reflect on my own life and gain perspective. I would like to take a moment to honour the memories of my dear friends, Mr. Unnikrishnan Mr. Nijin and my uncle, Mr. Muraleedharan whose departure left a void in my life. Their absence is deeply felt, and I will forever cherish the memories we shared.

In the face of these challenging times, my grandmother emerged as a pillar of strength and unwavering support. Until her passing in 2021, at the remarkable age of 96, she stood by my side, providing me with emotional support and guidance. Her presence in my life served as a constant reminder to persevere, stay focused on my goals and approach obstacles with humility. I am profoundly grateful for the profound influence she had on my life, and her teachings will continue to inspire me.

Additionally, I want to express my heartfelt appreciation for the unwavering support and understanding of my family and friends. Throughout this demanding journey, their love, encouragement, and unwavering belief in my abilities have been a constant source of motivation and strength. Despite the physical distance that separates us, their support has brought solace and reassurance during tough times. I am truly blessed to have such an incredible network of individuals who have stood by me through thick and thin.

While it is impossible to list every person who has supported me during this journey, I want to express my gratitude to Saraswathy Amma (my beloved grandma), my Amma (mom) Geetha Devi, my brother Mr. Arjun Gopakumar, my sister-in-law Ms. Devika Arjun, and my wonderful niece Bala Sundari Arjun and my uncle Mr. Suresh Kumar and family. Your love and support have been unwavering, and I am profoundly grateful to each of you. I also want to extend my appreciation to my friends Ms. Mary Ida Melody, Dr. Haritha Kambalathmana, Ms. Neha K Nasar, Dr. Jyothis Thomas, Mr. Sarath M P, Dr. Manju Perumbil, Dr. Anushree Sivadas, Dr. Yoshika Janapala, Dr. Navneeth Singh, Ms. Seetha Lakshmi, Dr. Fan Lu, Dr. Nikita Gagrani, Dr. Vidur Raj, Ms. Gayatri Vaidya, Ms. Parvathy, Ms. Huma Latheef, Ms. Dige, Ms. Shiyu Wei, Dr. Wei Wen Wong, Mr. Yang Yu, Mr. Yui, Mr. Kosala Dhanwansha, Ms. Anha Bhatt, DR. Rowena Yew, Dr. Maria del Rocio Camacho-Morales, Mr. Shreedhar Manjunath, Dr. Khosro Zangeneth Kamali, Dr.Sreelakshmi Mekkattu Tharayil, Mr. Aswin

Mohanan, Ms. Anneshwa Dey, Mr. Shaunik Nayyar, Mr. Govindh, Dr. Sangeeth Soman, Ms. Raji Sangeeth, Dr. Biveen S Lal, Ms. Krisha and Ms. Deborah Nesbitt for their friendship and support throughout this journey.

I want to take this moment to express my deep love and heartfelt gratitude to my partner, Mr. Varun Raj Kaipalath. Throughout this entire journey, despite the challenges of being in a long-distance relationship, you have stood by my side with unwavering support and understanding. Your presence in my life has been a constant source of strength and inspiration. Your unwavering belief in my abilities and your encouragement have propelled me forward during the difficult moments of this PhD journey. Your love has been a guiding light, keeping me grounded and reminding me of what truly matters.

To all those who have been a part of my life and have shown me kindness, understanding and support, I am truly grateful. Your presence and love have been invaluable, and I am forever indebted to you.

Aswani Gopakumar

Abstract

Direct bandgap semiconductor materials, such as GaAs, InAs, and InP, are widely used in various optoelectronic and electronic applications. Traditionally, these materials are synthesised using conventional epitaxial techniques that rely on thermal and lattice-matched substrates. These techniques utilise the unoccupied bonds on the surface of a bulk crystalline material substrate. However, in 1984, Koma et al. introduced an alternative epitaxial method driven by van der Waals forces, known as van der Waals epitaxy. This approach utilises a 2D material template such as graphene or mica.

van der Waals epitaxy offers several advantages over conventional epitaxy. One significant advantage is that the absence of surface dangling bonds significantly relaxes the requirement for lattice matching between the grown layer and the substrate. As a result, it provides an ideal platform for growing single crystalline materials with reduced defect densities. Additionally, the weak van der Waals bonding allows for easy detachment of the grown layer from the substrate, enabling the fabrication of flexible devices.

The emergence of flexible inorganic device architectures for applications such as the Internet of Things, photovoltaics and sensors has increased the demand for defect-free, large-area, and cost-effective epitaxial growth methods. van der Waals epitaxy addresses these requirements and offers a promising approach to achieve high-quality epitaxial growth. It enables the production of large-area materials with reduced defects, while also facilitating the fabrication of flexible devices.

This thesis investigates the experimental and theoretical approaches to achieve a comprehensive understanding of the growth process of III-V materials, focusing on the synthesis of GaAs and InAs nanowires (NWs), as well as InAs thin films, on 2D atomic layered materials.

The nanostructures/thin films and their interfaces with the van der Waals substrate are thoroughly examined, encompassing detailed characterisation of morphology, crystal structure, optical properties and electrical properties. Notably, this research achieves a high vertical yield of GaAs NWs and sets a record for synthesising GaAs quantum wires with a diameter as small as 5 nm. Additionally, the research attains a high yield of InAs NWs and successfully demonstrates uniform polycrystalline thin film structures over a large area on h-BN surface. These achievements represent significant advancements in the field of heteroepitaxial growth.

Successful synthesis of vertical GaAs NWs on synthetic mica substrates using Au-catalysed vapour-liquid-solid growth with the metalorganic chemical vapour deposition technique is achieved. The influence of growth parameters and pre-flow conditions on NW yield is investigated, and the resulting NWs exhibit high optical quality with emission at 1.43 eV, corresponding to GaAs band edge emission. The bonding between GaAs NWs and mica is found to follow a physisorption-type bonding, enabling easy detachment from the 2D layered mica substrate.

Furthermore, the synthesis and characterisation of GaAs quantum wires with dimensions as small as 5 nm in diameter are accomplished. The quantum wires exhibit excellent crystal morphology, pure zinc blende structure and enhanced negative stress with decreasing wire diameter. Extensive analyses of the electronic structure, surface

properties and bandgap characteristics demonstrate the increased confinement effects and altered electronic properties in GaAs quantum wires below the exciton Bohr radius.

Nanoscale simulations are performed to examine the impact of quantum confinement on optical transition energies in both freestanding quantum wires and those embedded within an AlGaAs passivation layer. The simulation results highlight a more pronounced variation in the bandgap of freestanding quantum wires.

Additionally, the growth of InAs NWs and thin films on h-BN/SiO_2/Si van der Waals substrates without catalysts or surface modifications is systematically studied. The influence of growth parameters on the properties of the NWs and thin films is investigated, and a predominantly mixed wurtzite and zinc blende phase NWs is observed.

Uniform coverage of polycrystalline InAs thin films on h-BN/SiO_2/Si, combined with room temperature photoluminescence and relatively high Hall mobility, demonstrates the potential for large-area, low-temperature growth of III-V thin films directly on van der Waals substrates using the metalorganic chemical vapour deposition technique.

Overall, this thesis significantly contributes to the experimental and theoretical understanding of III-V epitaxial growth on 2D material templates. The findings lay the groundwork for the growth and characterisation of III-V nanowire and planar structures on 2D templates, providing valuable insights for future research and potential applications. The synthesis of ultra-thin GaAs quantum wires also presents an opportunity for further exploration of their properties and potential applications.

Publications

Journal articles.

1. **Aswani Gopakumar Saraswathy Vilasam**, Ponnappa Kechanda Prasanna, Xiaoming Yuan, Zahra Azimi, Felipe Kremer, Chennupati Jagadish, Sudip Chakraborty, and Hark Hoe Tan, "Epitaxial Growth of GaAs Nanowires on Synthetic Mica by Metal–Organic Chemical Vapor Deposition" *ACS Applied Materials & Interfaces* 2022 ***14*** (2), 3395-3403. https://doi.org/10.1021/acsami.1c19236.

2. Doudou Zhang, Wensheng Liang, Astha Sharma, Joshua D. Butson, **Aswani Gopakumar Saraswathyvilasam**, Fiona J. Beck, Kylie R. Catchpole, Siva Karuturi; "Ultrathin HfO_2 passivated silicon photocathodes for efficient alkaline water splitting". *Appl. Phys. Lett.* 8 November 2021; 119 (19): 193901. https://doi.org/10.1063/5.0068087.

3. Azimi, Z., **Gopakumar, A**., Ameruddin, A.S. *et al.* Tuning the crystal structure and optical properties of selective area grown InGaAs nanowires. *Nano Res.* **15**, 3695–3703 (2022). https://doi.org/10.1007/s12274-021-3914-x

4. Raj, V., **Gopakumar, A**., Vaidya, G. *et al.* High-density individually addressable platinum nanoelectrodes for biomedical applications. *Discov Mater* **2**, 6 (2022). https://doi.org/10.1007/s43939-022-00027-1.

5. Z. Azimi, **A. Gopakumar**, L. Li, F. Kremer, M. Lockrey, A. A. Wibowo, H. T. Nguyen, H. H. Tan, C. Jagadish, J. Wong-Leung, Effective Passivation of InGaAs Nanowires for Telecommunication Wavelength Optoelectronics. *Adv. Optical Mater.* 2022, **10**, 2200739. https://doi.org/10.1002/adom.202200739.

6. **Aswani Gopakumar Saraswathy Vilasam,** Adhikari S, Gupta B, Balendhran S, Higashitarumizu N, Tournet J, Li L, Javey A, Crozier KB, Karuturi S, Jagadish C, Tan HH. "Large-area epitaxial growth of InAs nanowires and thin films on hexagonal boron nitride by metal organic chemical vapor deposition". Nanotechnology. 2023 Sep 18;**34**(49). DOI: 10.1088/1361-6528/acf3f1. PMID: 37625398.

7. **Aswani Gopakumar Saraswathy Vilasam**, Zhe Li, Zhicheng Su, Zahra Azimi, Naiyin Wang, Felipe Kremer, Chennupati Jagadish, and Hark Hoe Tan, "Epitaxial growth of free-standing sub-10 nm GaAs quantum wires on synthetic mica by metal organic chemical vapor deposition" (manuscript under preparation).

8. Doudou Zhang, Astha Sharma, Weisheng Pan, Fiona J. Beck, Heping Shen, Olivier Lee Cheong Lem, **Aswani Gopakumar Saraswathy Vilasam**, Cheng Yang, Klaus Weber, Yiliang Wu, Kylie Catchpole, and Siva Krishna Karuturi, "Monolithic Perovskite/Si Tandem Photoanode with Unprecedented Efficiency and Stability for Stand-Alone Photoelectrochemical Water Splitting" (Publication underway).

9. Wei S, Li Z, Murugappan K, Li Z, Zhang F, **Saraswathyvilasam AG**, Lysevych M, Tan HH, Jagadish C, Tricoli A, Fu L. A Self-Powered Portable Nanowire Array Gas Sensor for Dynamic NO_2 Monitoring at Room Temperature. Adv Mater. 2023 Mar;**35**(12): e2207199. doi: 10.1002/adma.202207199. Epub 2023 Jan 1. PMID: 36502280.

Conference papers

1. **A. Gopakumar Saraswathyvilasam**, X. Yuan, F. Kremer, H.H. Tan and C. Jagadish, Compound Semiconductor Week-2021 proceedings "Epitaxial growth of vertically aligned GaAs nanowires on synthetic mica" (Compound semiconductor week (CSW) 2020).

Table of Contents

List of Figures

List of tables

List of abbreviations

AC-STEM	aberration corrected scanning transmission electron microscopy
1D	one-dimensional
2D	two-dimensional
CVD	chemical vapour deposition
DFT	density functional theory
EBL	electron beam lithography
EDX	energy dispersive X-ray spectroscopy
FIB	focused ion beam
FWHM	full-width at half maximum
HAADF	high angle annular dark field
hBN	hexagonal boron nitride
HRTEM	high resolution transmission electron microscopy
LEDs	light emitting diodes
MBE	molecular beam epitaxy
MOCVD	metal-organic chemical vapour deposition
MOVPE	metal-organic vapour phase epitaxy
NW	nanowire
PECVD	plasma-enhanced chemical vapour deposition
PL	photoluminescence
SADP	selective area diffraction pattern
SEM	scanning electron microscopy
STEM	scanning transmission electron microscopy
TEM	transmission electron microscopy

TMAl	trimethylaluminium
TMGa	trimethylgallium
TMIn	trimethylindium
TRPL	time-resolved photoluminescence spectroscopy
vDW	van der Waals
vDWE	van der Waals epitaxy
VLS	vapour-liquid-solid
WZ	wurtzite
ZB	zinc blende

Chapter 1

Introduction

1.1 Heteroepitaxy of III-V using van der Waals Epitaxy

III-V compound semiconductors, such as GaAs, InAs, and InP, are highly esteemed for their exceptional electronic and optoelectronic properties, making them popular for the various devices, including solar cells [1–6], photodetectors [7–9], and lasers [10–16]. Recently, there has been a growing interest in low-temperature-grown semiconducting materials that offer various applications, such as the integration of sensors on integrated circuits (ICs) [17], display technologies [18] and back-end-of-line integration [19]. Low-temperature processing, which refers to processing below 500 °C, is crucial for these applications because high-temperature processes may not be compatible with the substrate or deposited layers involved. Additionally, incorporating low-temperature-grown semiconductor materials on low-cost and flexible substrates also lowers production costs.

In recent years, significant progress has been made in exploring the epitaxial growth of III-V nanowires (NWs) and thin films on conventional substrates such as GaAs [20–22] and Si [12,23–25]. Among the well-established growth techniques for NWs is the vapour-liquid-solid (VLS) mechanism [26]. However, the use of gold as a catalyst raises concerns regarding its incorporation into the grown material. Therefore, alternative growth methods, such as self-catalysed [25,27,28] and catalyst-free growth [29,30] on various types of substrates, have been developed to address these concerns.

The growth of III-V thin films has primarily been studied on substrates that have the same lattice parameters. However, when grown on substrates with different lattice parameters, such as Si, buffer layers have been used to manage the strain resulting from lattice and thermal mismatch. The heteroepitaxial growth of III-Vs on Si or dielectric SiO_2/Si substrates has also shown promise [31]. However, achieving high-quality heteroepitaxy remains challenging, as the deposited material often exhibits nano or micro-scale grain sizes and limited morphology control due to the large lattice and thermal mismatch.

The cost is a critical factor in the development of III-V-based devices. Currently, the high cost of these devices is attributed in part to the expensive single-crystal substrate used for epitaxy, accounting for around one-third of the total cost. As the demand for cost-effective, flexible, and transparent electronic and optoelectronic devices continues to rise, there is a shift towards unconventional substrates, such as two-dimensional (2D) atomic-layered materials, for epitaxy. These 2D materials possess unique properties, such as high flexibility, transparency, and tunable bandgap, making them highly attractive for various applications.

The discovery of graphene, a 2D material, has led to a surge of interest in other 2D materials, such as MoS_2 and hexagonal-BN (h-BN), for electronic and optoelectronic applications. One of the most significant advantages of these materials is their ability to serve as substrates for growing III-V thin films and nanostructures. van der Waals epitaxy (vdWE) is an emerging technique that allows the growth of any material on a 2D substrate or template [32]. In contrast to conventional epitaxy, where covalent bonds form between the III-V epilayers and III-V substrates, vdWE can result in van der Waals

bonding between the III-V epilayers and the 2D substrate. This bonding may alleviate problems associated with lattice and thermal mismatch, enabling the growth of high-quality III-V thin films and nanostructures on 2D substrates.

While there are many ongoing attempts to grow various materials on 2D substrates, few reports exist on growing II-VI and III-V epitaxial layers and nanostructures on 2D templates [33,34]. However, III-V semiconductor epilayers have excellent electronic/optoelectronic properties and can be easily "lifted off" for flexible device applications, making them a promising material for growth on 2D substrates. The ability to integrate III-V nanostructures and thin films on 2D substrates offers exciting new possibilities for low-cost and flexible electronic and optoelectronic devices.

The substrates employed in this thesis are synthetic mica and h-BN, which are 2D materials. Synthetic mica is a widely used dielectric material that has been utilised in capacitors and transformers for many years. Recently, it has garnered attention as a 2D template for vdWE due to its layered stacking structure. The growing number of publications on this topic highlights its increasing popularity [35–43].

h-BN is another 2D-layered material with a crystal structure and lattice parameter like graphene, but differs significantly in its physical properties, such as band structure, optical and electrical characteristics [44–47]. It has been shown that high-quality III-nitrides can be grown on h-BN with excellent crystallinity [48–50]. The unique layered structure of van der Waals substrates allows for the easy peel-off of micro- and nanostructures, as well as thin films grown on them.

The growth of III-V semiconductor NWs on muscovite mica has been sparsely documented, despite the extensive research conducted on thin films and nanostructures. While II-VI semiconductor NWs have been successfully grown on muscovite mica, the growth of III-V compound semiconductors on graphitic substrates has been achieved by Munshi *et. al* [51]. An atomic model has been developed to explain the growth of GaAs on graphitic surfaces, where different adsorption sites on the graphene lattice result in relative rotations of the NWs which have a hexagonal cross-section.

Reports on III-V NW growth using VLS and non-VLS techniques on graphene and other 2D templates have generally resulted in defective structures. A detailed look of previous research is presented in chapter 2. However, Ag-catalysed InAs NWs grown on graphite flakes have displayed a near-perfect wurtzite (WZ) crystal structure, with few stacking faults near the top and base of the NWs [52]. Nevertheless, limited information is available on the polarity of NWs grown on 2D templates. Despite being a polar material, GaAs NWs can orient in either the [111] A or [111] B directions on 2D templates, as there is no pure covalent bonding to dictate its polarity. In the case of ZnO NWs grown on muscovite mica, incommensurate growth was observed with A-polarity, which was attributed to surface dipoles on mica that encourage the formation of the first layer of oxygen atoms in the NWs.

One of the initial efforts to grow a continuous thin film of GaAs on graphene was reported by Alaskar *et al* [53]. They employed molecular beam epitaxy (MBE) on mechanically exfoliated multilayer graphene layers transferred onto SiO_2/Si substrates. The report concluded that the principal obstacle to achieving 2D growth of III-As materials on graphene is the high surface tension, which is caused by the low surface

energy of 2D materials and the low adsorption and migration energy of Ga, In, Al, As species on the graphitic surface.

To address this issue, researchers have investigated various surface modifications to promote epitaxial growth, such as using metal catalysts, annealing, or creating patterned substrates. These modifications can induce local strain and create nucleation sites for the III-V semiconductors. For instance, the use of metal catalysts can lower the activation energy of nucleation, while annealing can improve the quality of the interface between the III-V semiconductor and the 2D material template. These methods are briefly reviewed in the chapter 2. Jeeehwan Kim *et. al* [54] demonstrated the possibility of remote homoepitaxy and that vdWE is not solely confined to 2D materials as seed layers but extends to substrates below these materials. Their density functional theory (DFT) calculations reveal that epitaxial growth can occur through a substrate–epilayer gap of up to 9 Å, accommodating up to three layers of graphene. This approach is validated through homoepitaxial growth of GaAs (001) on GaAs (001) substrates covered with a monolayer of graphene, with successful applications in InP and GaP as well. The resulting single-crystalline films, efficiently released from the graphene-coated substrate, exhibit performance on par with conventionally prepared films in light-emitting devices.

Despite these efforts on graphene, challenges remain in achieving high-quality epitaxy of III-V semiconductors on various 2D material templates. The mismatch in lattice constants between the III-V semiconductor and the 2D material template can lead to defects and strain in the epitaxial layers. Furthermore, the thermal expansion coefficients of the III-V semiconductor and the 2D material template may also differ, leading to thermal strain and cracking of the epitaxial layers during cooling.

Nevertheless, continued research and development in this area hold promise for the growth of high-quality III-V semiconductor films and nanostructures on 2D material templates.

1.2 Thesis Synopsis

This dissertation presents a detailed investigation of the vdWE of III-V nanostructures and thin films on 2D layered materials, such as synthetic mica and h-BN, using the metal organic chemical vapour deposition technique. Chapter 2 provides background information and motivation for the subsequent chapters. Chapter 3 details the experimental techniques used and the underlying theories associated with this dissertation.

Chapter 4 presents a comprehensive growth study of GaAs NWs with a focus on achieving maximum vertical yield and good optical quality, specifically for the pure zinc blende phase. The study also investigates the potential for peeling off the NWs from the synthetic mica substrate for flexible device applications. The chapter includes density functional theory (DFT) calculations that elucidate the van der Waals nature of the NW-mica interface.

In Chapter 5, a high yield of GaAs NWs with diameters 20 nm and below over a large area on synthetic mica substrate is discussed. The chapter investigates the structural, electronic structure, and bandgap properties of these ultra-thin wires in detail. Experimental results of zinc blende crystal structure, binding energy, bandgap and electronic structure properties of ultra-thin nanowires are presented and discussed.

Chapter 6 provides a systematic investigation of various growth conditions for InAs NW and thin film growth on h-BN substrate. This chapter demonstrates the possibility

of achieving a high yield of vertically oriented NWs and uniform thin films on h-BN, representing a significant step towards realizing the high-density growth of III-V NWs and single-crystalline thin films on 2D materials.

Finally, Chapter 7 summarises the findings and provides suggestions for future work.

1.3 References

(1) Kirk, A. P.; Cardwell, D. W.; Wood, J. D.; Wibowo, A.; Forghani, K.; Rowell, D.; Pan, N.; Osowski, M. Recent Progress in Epitaxial Lift-Off Solar Cells. In *2018 IEEE 7th World Conference on Photovoltaic Energy Conversion, WCPEC 2018 - A Joint Conference of 45th IEEE PVSC, 28th PVSEC and 34th EU PVSEC*; 2018. https://doi.org/10.1109/PVSC.2018.8547801.

(2) Park, S.; Simon, J.; Schulte, K. L.; Ptak, A. J.; Wi, J. S.; Young, D. L.; Oh, J. Germanium-on-Nothing for Epitaxial Liftoff of GaAs Solar Cells. *Joule* **2019**. https://doi.org/10.1016/j.joule.2019.05.013.

(3) Tatavarti, R.; Hillier, G.; Dzankovic, A.; Martin, G.; Tuminello, F.; Navaratnarajah, R.; Du, G.; Vu, D. P.; Pan, N. Lightweight, Low Cost GaAs Solar Cells on 4″ Epitaxial Liftoff (ELO) Wafers. In *Conference Record of the IEEE Photovoltaic Specialists Conference*; 2008. https://doi.org/10.1109/PVSC.2008.4922900.

(4) Garnett, E. C.; Brongersma, M. L.; Cui, Y.; McGehee, M. D. Nanowire Solar Cells. *Annu. Rev. Mater. Res.* **2011**, *41*, 269–295. https://doi.org/10.1146/annurev-matsci-062910-100434.

(5) Li, J.; Aierken, A.; Liu, Y.; Zhuang, Y.; Yang, X.; Mo, J. H.; Fan, R. K.; Chen, Q. Y.; Zhang, S. Y.; Huang, Y. M.; Zhang, Q. A Brief Review of High Efficiency III-V Solar Cells for Space Application. *Front. Phys.* **2021**, *8* (February), 1–15. https://doi.org/10.3389/fphy.2020.631925.

(6) Li, Z.; Tan, H. H.; Jagadish, C.; Fu, L. III–V Semiconductor Single Nanowire Solar Cells: A Review. *Adv. Mater. Technol.* **2018**, *3* (9), 1–12. https://doi.org/10.1002/admt.201800005.

(7) Lapierre, R. R.; Robson, M.; Azizur-Rahman, K. M.; Kuyanov, P. A Review of III-V Nanowire Infrared Photodetectors and Sensors. *J. Phys. D. Appl. Phys.* **2017**, *50* (12).

https://doi.org/10.1088/1361-6463/aa5ab3.

(8) Anyebe, E. A.; Sandall, I.; Jin, Z. M.; Sanchez, A. M.; Rajpalke, M. K.; Veal, T. D.; Cao, Y. C.; Li, H. D.; Harvey, R.; Zhuang, Q. D. Optimization of Self-Catalyzed InAs Nanowires on Flexible Graphite for Photovoltaic Infrared Photodetectors. *Sci. Rep.* **2017**, *7* (December 2016), 1–9. https://doi.org/10.1038/srep46110.

(9) Barrigón, E.; Heurlin, M.; Bi, Z.; Monemar, B.; Samuelson, L. Synthesis and Applications of III-V Nanowires. *Chem. Rev.* **2019**, *119* (15), 9170–9220. https://doi.org/10.1021/acs.chemrev.9b00075.

(10) Han, Y.; Yan, Z.; Ng, W. K.; Xue, Y.; Ng, K. W.; Wong, K. S.; Lau, K. M. III-V Micro- And Nano-Lasers Deposited on Amorphous SiO2. *Appl. Phys. Lett.* **2020**, *116* (17). https://doi.org/10.1063/5.0008144.

(11) Wong, W. W.; Su, Z.; Wang, N.; Jagadish, C.; Tan, H. H. Epitaxially Grown InP Micro-Ring Lasers. *Nano Lett.* **2021**, *21* (13), 5681–5688. https://doi.org/10.1021/acs.nanolett.1c01411.

(12) Kim, H.; Chang, T. Y.; Lee, W. J.; Huffaker, D. L. III-V Nanowire Array Telecom Lasers on (001) Silicon-on-Insulator Photonic Platforms. *Appl. Phys. Lett.* **2019**, *115* (21), 3101. https://doi.org/10.1063/1.5126721.

(13) Han, Y.; Yan, Z.; Ng, W. K.; Xue, Y.; Wong, K. S.; Lau, K. M. Bufferless 15 Mm III-V Lasers Grown on Si-Photonics 220 Nm Silicon-on-Insulator Platforms. *Optica* **2020**, *7* (2), 148. https://doi.org/10.1364/optica.381745.

(14) Demir, I.; Elagoz, S. V/III Ratio Effects on High Quality InAlAs for Quantum Cascade Laser Structures. *Superlattices Microstruct.* **2017**, *104*, 140–148. https://doi.org/10.1016/j.spmi.2017.02.022.

(15) Roelkens, G.; Liu, L.; Liang, D.; Jones, R.; Fang, A.; Koch, B.; Bowers, J. III-V/Silicon Photonics for on-Chip and Intra-Chip Optical Interconnects. *Laser Photonics Rev.* **2010**, *4* (6), 751–779. https://doi.org/10.1002/lpor.200900033.

(16) Han, Y.; Lau, K. M. III-V Lasers Selectively Grown on (001) Silicon. *J. Appl. Phys.* **2020**, *128* (20). https://doi.org/10.1063/5.0029804.

(17) Gocalinska, A.; Pescaglini, A.; Secco, E.; Mura, E. E.; Thomas, K.; Curran, A.; Gity, F.; Nagle, R.; Schmidt, M.; Michałowski, P. P.; Hurley, P. K.; Povey, I.; Pelucchi, E.

Next Generation Low Temperature Polycrystalline Materials for above IC Electronics. High Mobility n- And p-Type III–V Metalorganic Vapour Phase Epitaxy Thin Films on Amorphous Substrates. *JPhys Photonics* **2020**, *2* (2). https://doi.org/10.1088/2515-7647/ab7557.

(18) Zhou, Z.; Yin, B.; Michel, J. On-Chip Light Sources for Silicon Photonics. *Light: Science and Applications*. 2015. https://doi.org/10.1038/lsa.2015.131.

(19) Datta, S.; Dutta, S.; Grisafe, B.; Smith, J.; Srinivasa, S.; Ye, H. Back-End-of-Line Compatible Transistors for Monolithic 3-D Integration. *IEEE Micro* **2019**, *39* (6), 8–15. https://doi.org/10.1109/MM.2019.2942978.

(20) Joyce, H. J.; Gao, Q.; Tan, H. H.; Jagadish, C.; Kim, Y.; Fickenscher, M. A.; Perera, S.; Hoang, T. B.; Smith, L. M.; Jackson, H. E.; Yarrison-Rice, J. M.; Zhang, X.; Zou, J. High Purity GaAs Nanowires Free of Planar Defects: Growth and Characterization. *Adv. Funct. Mater.* **2008**, *18* (23), 3794–3800. https://doi.org/10.1002/adfm.200800625.

(21) Chang, S.; Lee, G. J.; Song, Y. M. Recent Advances in Vertically Aligned Nanowires for Photonics Applications. *Micromachines* **2020**, *11* (8). https://doi.org/10.3390/MI11080726.

(22) Saxena, D.; Mokkapati, S.; Parkinson, P.; Jiang, N.; Gao, Q.; Tan, H. H.; Jagadish, C. Optically Pumped Room-Temperature GaAs Nanowire Lasers. *Nat. Photonics* **2013**, *7* (12), 963–968. https://doi.org/10.1038/nphoton.2013.303.

(23) Kostrzewa, M.; Grenet, G.; Regreny, P.; Leclercq, J. L.; Perreau, P.; Jalaguier, E.; Di Cioccio, L.; Hollinger, G. Feasibility of III-V on-Silicon Strain Relaxed Substrates. In *Journal of Crystal Growth*; 2005. https://doi.org/10.1016/j.jcrysgro.2004.10.080.

(24) Benyoucef, M.; Reithmaier, J. P. Direct Growth of III-V Quantum Dots on Silicon Substrates: Structural and Optical Properties. *Semicond. Sci. Technol.* **2013**, *28* (9). https://doi.org/10.1088/0268-1242/28/9/094004.

(25) Plissard, S.; Larrieu, G.; Wallart, X.; Caroff, P. High Yield of Self-Catalyzed GaAs Nanowire Arrays Grown on Silicon via Gallium Droplet Positioning. *Nanotechnology* **2011**, *22* (27), 275602. https://doi.org/10.1088/0957-4484/22/27/275602.

(26) Wagner, R. S.; Ellis, W. C. Vapor-Liquid-Solid Mechanism of Single Crystal Growth.

Appl. Phys. Lett. **1964**, *4* (5), 89–90. https://doi.org/10.1063/1.1753975.

(27) Mandl, B.; Stangl, J.; Hilner, E.; Zakharov, A. A.; Hillerich, K.; Dey, A. W.; Samuelson, L.; Bauer, G.; Deppert, K.; Mikkelsen, A. Growth Mechanism of Self-Catalyzed Group III-V Nanowires. *Nano Lett.* **2010**, *10* (11), 4443–4449. https://doi.org/10.1021/nl1022699.

(28) Tersoff, J. Stable Self-Catalyzed Growth of III-V Nanowires. *Nano Lett.* **2015**, *15* (10), 6609–6613. https://doi.org/10.1021/acs.nanolett.5b02386.

(29) Kanungo, P. Das; Schmid, H.; Björk, M. T.; Gignac, L. M.; Breslin, C.; Bruley, J.; Bessire, C. D.; Riel, H. Selective Area Growth of III-V Nanowires and Their Heterostructures on Silicon in a Nanotube Template: Towards Monolithic Integration of Nano-Devices. *Nanotechnology* **2013**. https://doi.org/10.1088/0957-4484/24/22/225304.

(30) Azimi, Z.; Gopakumar, A.; Ameruddin, A. S.; Li, L.; Truong, T.; Nguyen, H. T.; Tan, H. H.; Jagadish, C.; Wong-Leung, J. Tuning the Crystal Structure and Optical Properties of Selective Area Grown InGaAs Nanowires. *Nano Res.* **2022**, *15* (4), 3695–3703. https://doi.org/10.1007/s12274-021-3914-x.

(31) Du, Y.; Xu, B.; Wang, G.; Miao, Y.; Li, B.; Kong, Z.; Dong, Y.; Wang, W.; Radamson, H. H. Review of Highly Mismatched III-V Heteroepitaxy Growth on (001) Silicon. *Nanomaterials* **2022**, *12* (5), 741. https://doi.org/10.3390/nano12050741.

(32) Koma, A. Van Der Waals Epitaxy for Highly Lattice-Mismatched Systems. *J. Cryst. Growth* **1999**, *201–202*, 236–241. https://doi.org/10.1016/S0022-0248(98)01329-3.

(33) Utama, M. I. B.; Zhang, Q.; Jia, S.; Li, D.; Wang, J.; Xiong, Q. Epitaxial II-VI Tripod Nanocrystals: A Generalization of van Der Waals Epitaxy for Nonplanar Polytypic Nanoarchitectures. *ACS Nano* **2012**, *6* (3), 2281–2288. https://doi.org/10.1021/nn204344z.

(34) Anyebe, E. A.; Kesaria, M. Recent Advances in the Van Der Waals Epitaxy Growth of III-V Semiconductor Nanowires on Graphene. *Nano Sel.* **2021**, *2* (4), 688–711. https://doi.org/10.1002/nano.202000142.

(35) Utama, M. I. B.; Belarre, F. J.; Magen, C.; Peng, B.; Arbiol, J.; Xiong, Q. Incommensurate van Der Waals Epitaxy of Nanowire Arrays: A Case Study with ZnO

on Muscovite Mica Substrates. *Nano Lett.* **2012**, *12* (4), 2146–2152. https://doi.org/10.1021/nl300554t.

(36) Bitla, Y.; Chu, Y. H. MICAtronics: A New Platform for Flexible X-Tronics. *FlatChem*. 2017, pp 26–42. https://doi.org/10.1016/j.flatc.2017.06.003.

(37) Qin, J. K.; Shao, W. Z.; Li, Y.; Xu, C. Y.; Ren, D. D.; Song, X. G.; Zhen, L. Van Der Waals Epitaxy of Large-Area Continuous ReS2films on Mica Substrate. *RSC Adv.* **2017**. https://doi.org/10.1039/c7ra01748k.

(38) Li, H.; Cao, J.; Zheng, W.; Chen, Y.; Wu, D.; Dang, W.; Wang, K.; Peng, H.; Liu, Z. Controlled Synthesis of Topological Insulator Nanoplate Arrays on Mica. *J. Am. Chem. Soc.* **2012**, *134* (14), 6132–6135. https://doi.org/10.1021/ja3021395.

(39) Wang, D.; Li, J. N.; Zhou, Y.; Xu, D. H.; Xiong, X.; Peng, R. W.; Wang, M. Van Der Waals Epitaxy of Ultrathin α-MoO3 Sheets on Mica Substrate with Single-Unit-Cell Thickness. *Appl. Phys. Lett.* **2016**, *108* (5), 1–7. https://doi.org/10.1063/1.4941402.

(40) Ji, Q.; Zhang, Y.; Gao, T.; Zhang, Y.; Ma, D.; Liu, M.; Chen, Y.; Qiao, X.; Tan, P. H.; Kan, M.; Feng, J.; Sun, Q.; Liu, Z. Epitaxial Monolayer MoS2 on Mica with Novel Photoluminescence. *Nano Lett.* **2013**, *13* (8), 3870–3877. https://doi.org/10.1021/nl401938t.

(41) Simbrunner, C.; Schwabegger, G.; Resel, R.; Dingemans, T.; Sitter, H. The Epitaxial Growth of Self-Assembled Ternaphthalene Fibers on Muscovite Mica. *Cryst. Growth Des.* **2014**, *14* (2), 442–449. https://doi.org/10.1021/cg400912t.

(42) Zhang, F.; Zhang, P.; Hou, J.; Yun, X.; Li, W.; Du, Q.; Chen, Y. Large Scale Anomalous Patterns of Muscovite Mica Discovered by Atomic Force Microscopy. *ACS Appl. Mater. Interfaces* **2015**, *7* (16), 8699–8705. https://doi.org/10.1021/acsami.5b00984.

(43) Ginocchio, I. F. Title Synthetic Mica and Its Appplications. **2006**, *124*, 119–124.

(44) Wang, Y.; Xu, L.; Yang, Z.; Xie, H.; Jiang, P.; Dai, J.; Luo, W.; Yao, Y.; Hitz, E.; Yang, R.; Yang, B.; Hu, L. High Temperature Thermal Management with Boron Nitride Nanosheets. *Nanoscale* **2018**, *10* (1), 167–173. https://doi.org/10.1039/c7nr07058f.

(45) Cai, Q.; Scullion, D.; Gan, W.; Falin, A.; Zhang, S.; Watanabe, K.; Taniguchi, T.;

Chen, Y.; Santos, E. J. G.; Li, L. H. High Thermal Conductivity of High-Quality Monolayer Boron Nitride and Its Thermal Expansion. *Sci. Adv.* **2019**, *5* (6), 1–9. https://doi.org/10.1126/sciadv.aav0129.

(46) Pease, R. S. Crystal Structure of Boron Nitride. *Nature* **1950**, *165* (4201), 722–723. https://doi.org/10.1038/165722b0.

(47) Falin, A.; Cai, Q.; Santos, E. J. G.; Scullion, D.; Qian, D.; Zhang, R.; Yang, Z.; Huang, S.; Watanabe, K.; Taniguchi, T.; Barnett, M. R.; Chen, Y.; Ruoff, R. S.; Li, L. H. Mechanical Properties of Atomically Thin Boron Nitride and the Role of Interlayer Interactions. *Nat. Commun.* **2017**, *8*, 1–9. https://doi.org/10.1038/ncomms15815.

(48) Makimoto, T.; Kumakura, K.; Kobayashi, Y.; Akasaka, T.; Yamamoto, H. A Vertical InGaN/GaN Light-Emitting Diode Fabricated on a Flexible Substrate by a Mechanical Transfer Method Using BN. *Appl. Phys. Express* **2012**. https://doi.org/10.1143/APEX.5.072102.

(49) Sundaram, S.; Vuong, P.; Mballo, A.; Ayari, T.; Karrakchou, S.; Patriarche, G.; Voss, P. L.; Salvestrini, J. P.; Ougazzaden, A. MOVPE of GaN-Based Mixed Dimensional Heterostructures on Wafer-Scale Layered 2D Hexagonal Boron Nitride - A Key Enabler of III-Nitride Flexible Optoelectronics. *APL Mater.* **2021**, *9* (6). https://doi.org/10.1063/5.0049306.

(50) Kobayashi, Y.; Kumakura, K.; Akasaka, T.; Makimoto, T. Layered Boron Nitride as a Release Layer for Mechanical Transfer of GaN-Based Devices. *Nature* **2012**, *484* (7393), 223–227. https://doi.org/10.1038/nature10970.

(51) Munshi, A. M.; Dheeraj, D. L.; Fauske, V. T.; Kim, D. C.; Van Helvoort, A. T. J.; Fimland, B. O.; Weman, H. Vertically Aligned GaAs Nanowires on Graphite and Few-Layer Graphene: Generic Model and Epitaxial Growth. *Nano Lett.* **2012**, *12* (9), 4570–4576. https://doi.org/10.1021/nl3018115.

(52) Utama, M. I. B.; Belarre, F. J.; Magen, C.; Peng, B.; Arbiol, J.; Xiong, Q. Incommensurate van Der Waals Epitaxy of Nanowire Arrays: A Case Study with ZnO on Muscovite Mica Substrates. *Nano Lett.* **2012**, *12* (4), 2146–2152. https://doi.org/10.1021/nl300554t.

(53) Alaskar, Y.; Arafin, S.; Wickramaratne, D.; Zurbuchen, M. A.; He, L.; McKay, J.; Lin,

Q.; Goorsky, M. S.; Lake, R. K.; Wang, K. L. Towards van Der Waals Epitaxial Growth of GaAs on Si Using a Graphene Buffer Layer. *Adv. Funct. Mater.* **2014**, *24* (42), 6629–6638. https://doi.org/10.1002/adfm.201400960.

(54) Kim, Y.; Cruz, S. S.; Lee, K.; Alawode, B. O.; Choi, C.; Song, Y.; Johnson, J. M.; Heidelberger, C.; Kong, W.; Choi, S.; Qiao, K.; Almansouri, I.; Fitzgerald, E. A.; Kong, J.; Kolpak, A. M.; Hwang, J.; Kim, J. Remote Epitaxy through Graphene Enables Two-Dimensional Material-Based Layer Transfer. *Nature* **2017**, *544* (7650), 340–343. https://doi.org/10.1038/nature22053.

Chapter 2

Literature Review

2.1 Introduction

This chapter provides the background and motivation for this dissertation. The research presented in this thesis focuses on the growth and characterisation of III-V semiconductor nanostructures on 2D materials using the technique of vdWE. The chapter is outlined as follows:

Section 2.2 provides an overview of the significance of vdWE in the growth of III-V semiconductor nanostructures. This section discusses the advantages of vdWE over conventional epitaxy. A short account of the III-V NW growth on van der Waals substrates is also given to highlight the research that is done in this area.

Section 2.3 introduces the concept of surface energy engineering, which plays a crucial role in the growth of high-quality III-V nanostructures. This section discusses the importance of surface energy engineering in controlling the morphology and crystal quality of the nanostructures.

Section 2.4 is dedicated to the study of III-V nanostructures and thin films, with a focus on the significance of NWs. Subsections 2.4.1 and 2.4.2 present the importance of NWs and their properties in general, respectively. Subsection 2.4.3 provides an overview of III-V NWs and their unique properties. Subsection 2.4.4 discusses the various techniques used for the synthesis of III-V NWs, while subsection 2.4.5 provides an overview of III-Nitride NWs 2.4.6 explains the crystal structure and polarity of NWs. Finally, subsection 2.4.7 emphasises the significance of passivation in improving the performance of III-V NWs.

Section 2.5 focuses on quantum confinement, a phenomenon that arises in low-dimensional systems such as NWs. Subsection 2.5.1 discusses the quantum confinement effect in III-V NWs and its impact on their electronic and optical properties. Subsection 2.5.2 introduces the bond-order-length-strength (B-OLS) mechanism, which is used to understand the impact of quantum confinement on the properties of NWs.

Overall, this chapter covers the fundamental principles and concepts that underpin the experimental and theoretical results.

2.2 Significance of van der Waals Epitaxy (vdWE)

Over the past three decades, there has been numerous research to integrate III-V compound semiconductors on Si.[1–3] Efficient optoelectronic devices such as light emitting diodes[4,5], laser diodes[1,6–12] and photodetectors[13–16] can be made of these semiconductor materials, with a goal of integrating them to Si, thanks to the direct bandgap and high carrier mobility properties of III-V compounds. Another very important goal in this direction of research is to develop efficient optoelectronic devices grown directly on inorganic flexible substrates or alternative methods that allows easy peel off after growth from the substrates to achieve flexibility.

Among various integration approaches, direct epitaxial growth of III-V compounds on 2D templates such as graphene, mica, hexagonal boron nitride (h-BN) and transition metal dichalcogenides, have attracted much interest in the past decade.[17,18,19,10,20] However, this is not obvious as it has many challenges such as dissimilar chemical bonding, surface dangling bonds, lattice mismatch and thermal expansion mismatch to name a few. In 1984, Koma published the work on unconventional, noncovalent heteroepitaxy which he called van der Waals Epitaxy.[21] He successfully demonstrated

how vdWE technique could be used to largely eliminate the serious problem of lattice mismatch encountered in conventional epitaxy. Over the past decade there has been a growing interest in epitaxial growth of III-V semiconductors on 2D templates, whether for achieving integration on Si or making flexible devices.[20,17,18,22]

Epitaxial growth of III-V semiconductor materials on 2D layers is not trivial. Due to the absence of reactive dangling bonds on 2D substrates, the wettability is poor, leading to the suppression of nucleation and hindering the growth of single-crystalline NWs structures. This challenge is even greater for the growth of 2D thin films, which tend to form rough surfaces and result in the growth of clusters following the Volmer-Weber growth. Additionally, the weak interaction between 2D layers and single-crystalline thin films grown through vdWE growth could result in incommensurate short-range ordering, leading to partial epilayer-substrate epitaxial alignment across the epitaxial films and the growth of polycrystalline layers with textured grain structure.

The need for flexible, high-performance, and cost-effective optoelectronic nanodevices has led to an increasing interest in integrating NWs with graphene. Over the last decade, significant progress has been made in the growth and applications of III-V semiconductor NWs on graphene, the review article by Ezekiel Anyebe and Manoj Kesaria focuses on recent advances in the vdWE growth of III-V semiconductor NWs on graphene and provides useful strategies for fabricating graphene-based NWs devices.[20] Although there are limited reports of NW/graphene hybrid devices, the review aims to facilitate an increase in NW-based graphene device applications.

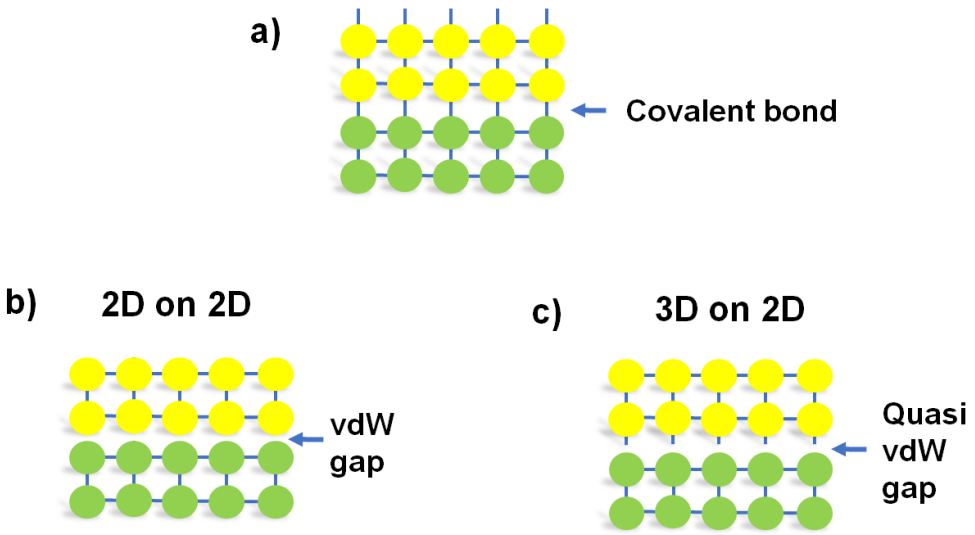

Fig 2.1 a) Conventional epitaxial interface with covalent bonding. b) van der Waals gap is present at the interface of a 2D material over grown on a 2D substrate. c) A quasi-van der Waals gap appears when a 3D material is grown on a 2D template.

There is a significant difference between conventional epitaxy and vdWE. Figure 2.1 illustrates the difference in interfacial bonding. Conventional epitaxy methods are used to grow large-area single crystal epitaxial materials by controlling their domain orientation on single-crystal substrates. The interaction between the epitaxial layer and the substrate is covalent in traditional three-dimensional, covalently-bonded materials, which have strong chemical bonding at the interface. The epitaxy can be achieved through homoepitaxy, where the substrate and the epitaxial layer are of the same material, or heteroepitaxy, where they are different. However, heteroepitaxy can lead to strain in the epilayer or misfit dislocations at the interface due to the lattice mismatch between the substrate and the epitaxial layer. A rigid lattice matching is demanded in traditional 3D materials epitaxy limiting the viable material combinations in heteroepitaxy. vdWE on the other hand, is a different type of epitaxy that relies on van der Waals (vdW) interaction between the substrate and epilayer, rather than strong chemical bonding as in conventional epitaxy. This means that vdWE can be achieved

in bulk materials with passivated surface dangling bonds or in vdW materials with naturally terminated surfaces, including 2D materials. Unlike conventional epitaxy, vdWE does not require strict lattice matching, allowing for larger lattice mismatches of up to 50%. As a result, vdWE can be used to extend heteroepitaxial systems and has attracted attention for 2D single crystal preparation. Furthermore, single-crystal 2D materials can serve as vdW substrates for the fabrication of many functional materials, including III-V compound semiconductors, metals, and macromolecular polymers. However, the nuances of epitaxy mechanisms on different substrates are not well understood and require further exploration to achieve controllable synthesis of large-scale high-quality single-crystal 2D materials.

A successful strategy when it comes to NW growth, is based on vapor liquid solid VLS growth technique. According to Wallentin *et al,* growing vertical NWs on graphitic substrates such as graphene or graphite is a challenging task.[23] One of the major hurdles is the small size of the graphene lattice, which is less than half the bond length of III−Vs. As a result, III−V atoms must occupy positions where only some of the available sites in the graphene lattice are occupied, potentially with an in-plane lattice rotation. Another challenge is the inert nature of graphene layers, which makes it difficult for III-V atoms to bond with carbon atoms. Hong and Fukui suggested that weak van der Waals bonding between the carbon atoms in graphene and the semiconductor atoms is responsible for InAs NW growth, rather than covalent bonding.[24] This weak bonding results in a high interfacial energy between the two materials.

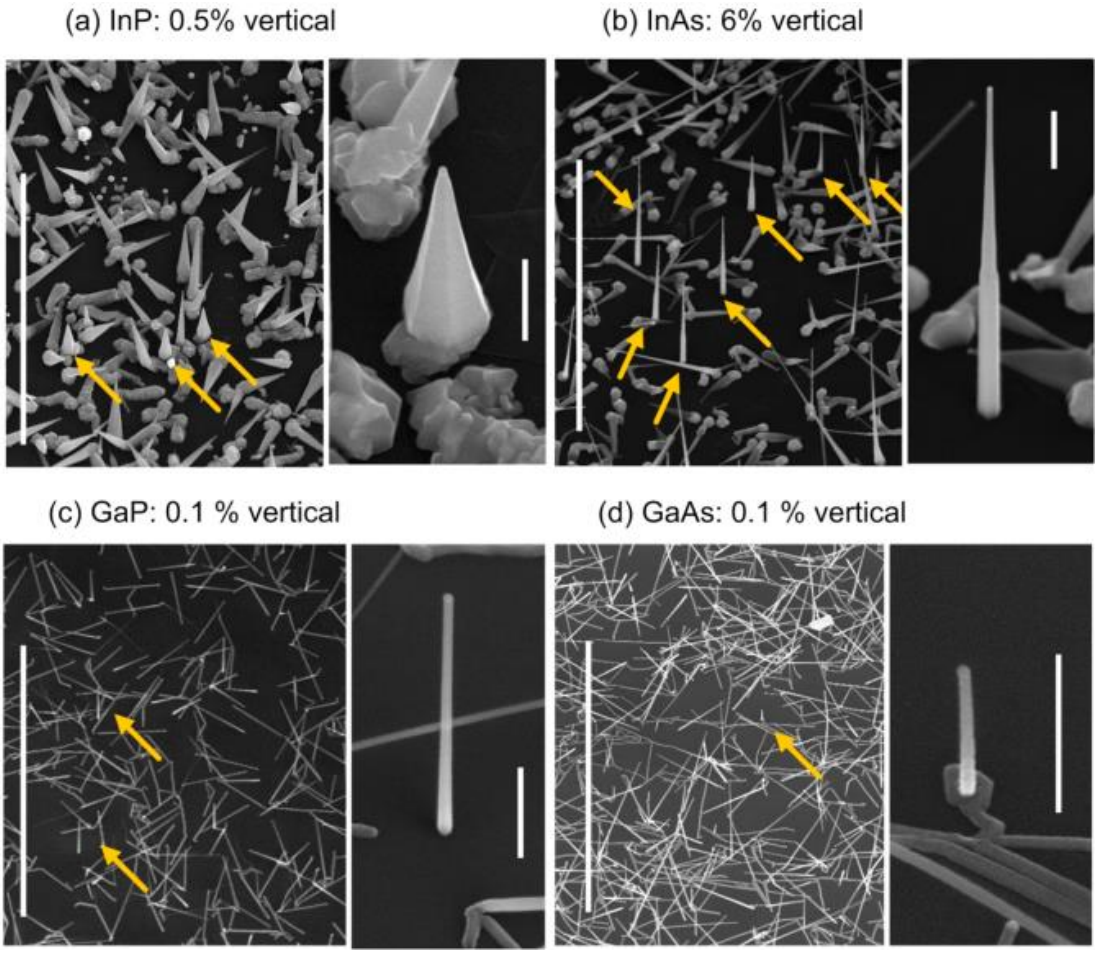

Figure 2.2 SEM of 30 degrees tilted various NWs grown on graphite: (a) InP, (b) InAs, (c) GaP and (d) GaAs. Scale bars are 10 μm. Insets show higher magnification images, with 0.5 μm scale bars. Arrows indicate vertical NWs. Reproduced from ref 23.

They investigated the growth of Au-seeded NWs of four common III−V materials, including InAs, InP, GaP and GaAs, on highly ordered pyrolytic graphite (HOPG) as the substrate. Despite the significant variation in lattice parameters between the materials and graphite, the study found that it is possible to grow vertical III−V NWs on graphite regardless of the material, but the yield of vertically grown NWs is low or very low, with some NWs observed to have grown along the substrate instead of vertically. Figure 2.2 summarises their NW vertical yield. The maximum vertical yield was as low as 0.5% for InP, 6% for InAs and 0.1% for both GaP and GaAs. However,

once the NWs began growing vertically, they were typically stable and continued in the same direction. The researchers also reported that the addition of Zn before growth improved the yield of vertically grown NWs for GaP and GaAs. Essentially, they have shown that the Zn improves the wetting compared with just Ga, although the effect is difficult to quantify.

Meyer-Holdt investigated the use of Ag as a catalyst for InAs NW growth on transferable graphite flakes (GFs) instead of the commonly used Au. [25] The study found that mostly vertically aligned InAs NWs in the [111]/[0001] direction grew selectively on the GFs with a high aspect ratio, while growth did not proceed on the bare InAs substrate as shown in Figure 2.3. The use of Ag as a catalyst is suggested to be the reason for this selective growth due to the shorter diffusion length compared to Au on graphitic substrate. TEM analysis showed that the Ag terminated NWs had a pure WZ crystal structure with occasional stacking faults near the top and bottom. The NW/GF ensembles can be transferred to a preferred substrate for further characterisation and device fabrication with significant potential for various applications. The study suggests a highly promising pathway for obtaining novel electronic and optical devices based on NW/GF hybrid systems.

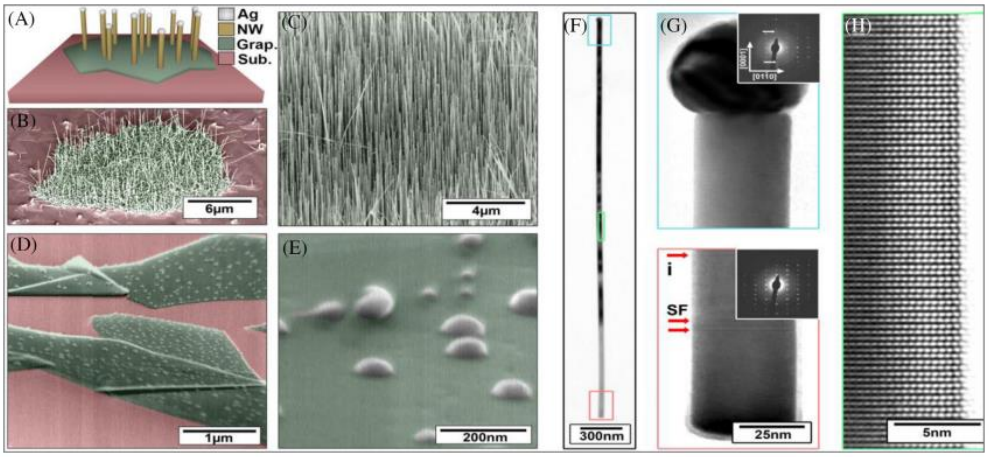

Figure 2.3 Ag-seeded NW growth on graphitic flakes (GF). (a) Sketch of the ensemble of NWs. (b)–(e) 45° tilted SEM micrographs of the pre and post growth. (b) A typical GF with Ag-seeded InAs NWs. (c) Zoomed in micrograph of vertical Ag-seeded InAs NWs from (b). (d) Micrograph of Ag particles on GFs. No Ag particles are visible on the bare InAs substrates. (e) Zoomed in SEM image of the post-annealed Ag droplets on a GF from (d) showing a hemispherical shape. (f)–(h) TEM micrographs of a Ag seeded NW grown on GF. The inset displays a selected area TEM diffraction pattern with the electron incident beam along the InAs [2-1-10] zone axis with additional peaks along the [0001] direction presumably from the seed particle (white arrows). (h) HRTEM image of a representative middle section of a NW demonstrating pure WZ structure. Reproduced from ref. 25.

It is important to note that traditional VLS growth techniques that use catalysts like Au or Ag can cause metal diffusion into the NWs, potentially affecting their properties. To address this concern, researchers have explored alternative growth methods like self-catalysed and catalyst-free approaches for growing NWs on 2D templates. Munshi et al.'s work is an example of such alternative methods, which demonstrated the feasibility of growing high-quality GaAs NW/graphene hybrid heterostructures using MBE with the self-catalysed technique.[26] They proposed a generic atomic model to describe the

possible epitaxial growth configurations for III-V NWs on graphene and experimentally verified it through the growth of vertically aligned GaAs NWs on graphene surfaces using MBE. The authors demonstrated that high-quality GaAs NW/graphene hybrid heterostructures can be realised using the self-catalysed technique and fabricated a single GaAs NW photodetector with high responsivity. The proposed heteroepitaxial growth configurations could be used to develop new types of NW/graphite and NW/graphene hybrid device systems.

Similarly, Sundaram *et. al*, employed an MOCVD process to fabricate wafer-scale arrays of 1D nanorod device structures in a one-step process on 2D h-BN.[27] Based on electron microscopy analysis, the 2D-1D hetero-interface was found to be clean and abrupt, with nanorods growing on a thin AlN seed layer. Although the AlN layer exhibited poor crystal orientation, the growth of GaN was predominantly along the c-axis due to rapid competitive growth, which suppressed growth along other directions. Furthermore, the authors successfully grown them on various substrates, including sapphire, silicon, and quartz, and demonstrated the mechanical transfer of the nanorod structures onto a copper tape. Notably, the growth of III-nitride semiconductor heterostructures on h-BN/Si has the potential for heterogeneous integration with Si devices. This study has broad implications for the scalable integration of semiconductor nanostructures with various substrates, including glass and plastics, which are particularly relevant to the development of wearable and flexible technologies. Despite the growing interest in this field, only a few reports on the growth of III-V NWs and thin films on 2D material substrates are available.

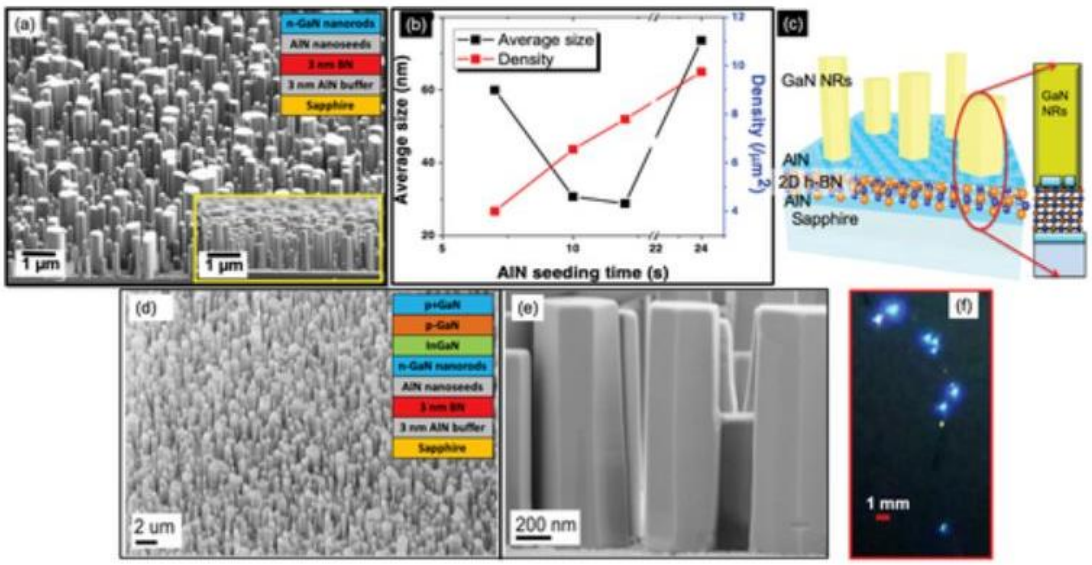

Figure 2.4 a) SEM image of the vertical GaN nanorod structure grown on h-BN/AlN/sapphire substrate. The inset shows a higher magnification cross-sectional view of the GaN nanostructures. b) Variation of nucleation density and average size (diameter) of GaN nanorods with AlN seeding time. c) Illustration of the nanorods grown on h-BN/AlN/sapphire substrate. d) SEM image of p-GaN/i-InGaN/n-GaN p-i-n nanorod structure on h-BN/AlN/sapphire substrate. Inset shows a schematic of the nanorod structure. e) High magnification cross-sectional SEM image of the p-i-n nanorod structures showing the vertical alignment and flat-topped hexagonal columns. f) Blue light emission from the p-i-n nanorod structures under electrical injection. Reproduced from ref. 27.

2.3 Surface Energy Engineering

The growth of III-V semiconductors on 2D templates is a complex process due to the low surface energy of these materials. For instance, to grow NWs, the contact angle between the gold nanoparticle and the substrate is important for determining the direction and crystal phase of the resulting NW. This angle is determined by the surface

energy of the nanoparticle and substrate at the growth temperature. In a review by Yuan et.al., the role of surface energy in NW growth and polarity is discussed in detail.[28] By engineering the contact angle, the vertical yield, crystal phase, and NW polarity can be controlled. It is best to have a medium-to-large contact angle for perpendicular NW growth, as a low contact angle results in in-plane/crawling NWs and an extremely large angle causes de-wetting and no NW growth. The substrate surface energy can be changed using surfactants or passivation. Altering the nanoparticle volume by incorporating Zn or a group III atom can also change the substrate surface energy and contact angle. In-situ TEM measurements have shown that the AsH_3 flow rate and V/III ratio affect the gold contact angle and crystal phase selection during GaAs NW growth.

Surface engineering can be done ex-situ to modify the 2D material surface prior to growth. Hong et. al. and Fukui et. al. have demonstrated this method, identifying the key factors necessary to produce inorganic nanomaterials on graphitic substrates.[29,30] In their work, they found that the in-plane lattice coherency and controlled surface atomic layer ledge of graphitic substrates contributed to the formation of vertical InAs NW arrays using vdW heteroepitaxy. Through a combination of dry etching and substrate patterning, they were able to achieve controlled, selective-area vdW heteroepitaxy of InAs NW arrays on graphitic films. This method allows for high-yield, uniform vertical NWs to be produced in a controlled manner, opening possibilities for the fabrication of various semiconductor devices on carbon honeycomb lattices.

2.4 III-V Compound semiconductors

III-V compound semiconductor nanostructures and thin films are of great importance in various applications such as light emitting diodes (LEDs), lasers, sensors and solar cells.

2.4.1 Significance of NWs

Semiconductor NWs offer unique advantages as building blocks for future electronic and photonic devices. Due to their reduced dimensionality, NWs exhibit outstanding materials properties, high surface-to-volume ratio and can be assembled from the bottom-up, making them highly promising for nanoscale device integration. Within the past decade, a wide range of NW-based electronic and photonic devices have been developed, including NW solar cells [31–34], photodetectors [15,16,34], waveguides [37], LEDs [4,5,38,39], lasers [1,9,11,12,40], single photon sources [41–43]and biological and chemical sensors [36,44,45].

2.4.2 NW Properties

NWs are quasi-one-dimensional nanostructures with diameters typically less than 100 nm and lengths greater than 1 μm. Their unique geometry confers significant advantages over conventional planar structures. If the NW diameter is sufficiently small, these structures can exhibit quantum confinement in two dimensions. NWs have high surface-to-volume ratio, making them ideal for sensing applications. NWs can also function as interconnects, in addition to their function as active device elements. Device architectures based on vertically-standing NWs will allow ultrahigh density device integration into a single chip. Furthermore, NWs can be tailored into unique axial and radial heterostructures, which greatly expands the range of device possibilities.

2.4.3 III-V NWs

Among semiconductor NWs, III-V NWs show promise due to their superior electrical and optical properties. GaAs NWs, for instance, have significant merits associated with their direct bandgap and high electron mobility, making them ideal for electronic and optoelectronic device applications, such as lasers, solar cells and photodetectors. InAs NWs feature a narrow bandgap and very high electron mobility, which make them

highly promising for use in future high-frequency electronic devices. InGaAs NWs have significant potential due to their suitable bandgap energy for applications in long wavelength optical transmission and integrated photonics. Moreover, III-V NWs can be grown epitaxially on Si without antiphase defects or misfit dislocations, enabling monolithic integration of III-V NW optoelectronic devices with the well-established Si microelectronics technology.

2.4.4 III-V NW synthesis

There are two primary methods for fabricating III-V NWs: top-down and bottom-up. Top-down methods involve using lithography and etching techniques, such as electron beam lithography or focused ion beam milling, to pattern NWs from bulk material. [46] While top-down fabrication methods are routinely used in the microelectronics industry, they become increasingly problematic as device length scales shrink in accordance with Moore's law. These techniques have limited resolution, which makes it difficult to define smaller features and diminishes the quality of nanostructures. Additionally, the etching and patterning processes introduce surface defects that can adversely affect nanostructure properties, and the process is inherently wasteful.

Bottom-up methods, on the other hand, involve the chemical synthesis of NWs, which can be controlled and tuned during growth. These NWs can be used as building blocks to assemble more complex nanoscale devices and architectures. Bottom-up methods allow for the fabrication of atomically precise and complex devices that are not possible with conventional top-down technologies. As a result, this paradigm is expected to lead to the next generation of nanoscale electronics. The bottom-up approach mimics the growth of living organisms, where macro-molecules assemble into larger and more complex structures. Combining the top down and bottom up approaches may allow best of both worlds such as directed self-assembly.

2.4.5 III-Nitride NWs

Although this thesis focuses on the MOCVD growth of III-As NWs and characterizations. It is important to note that notable advances in III-nitrides have also been achieved in the past few decades.

These III-nitride nanowires can be grown without a catalyst on Si (001) substrates in the wurtzite crystalline form, with the c-axis aligned along the growth direction. They show great promise in advancing the development of visible LEDs and lasers. An illustrative example of this potential is the successful demonstration of an electrically pumped laser emitting green light (λ= 533 nm) by Ooi and Bhattacharya *et. al* [47]. This was achieved using an edge-emitting InGaN/GaN disk-in-nanowire array on a (001) silicon substrate.

Prabaswara and Ooi *et. al* have successfully demonstrated the direct growth and fabrication of a III-nitride NW-based LEDs on amorphous quartz. [48] The proof-of-concept device exhibited a low turn-on voltage of 2.6 V and achieved approximately 40% transparency across the visible wavelength. They maintained electrical conductivity by utilising a TiN/Ti interlayer on quartz as a translucent conducting layer.

Mi and colleagues explored extensively the molecular beam epitaxial (MBE) growth and characterisation of Al-rich AlGaN nanowire heterostructures on a silicon substrate. [49] They successfully showcased the functionality of electrically injected AlGaN nanowire lasers operating at approximately 239 nm, featuring an impressively low threshold current of 0.3 mA at room temperature. Their investigation concentrated on overcoming the obstacles associated with achieving electrically injected AlGaN quantum well lasers in the UV-C band (100-280 nm), a critical requirement for

applications like surface treatment, bio-agent detection, and the manufacturing of microelectronics.

2.4.6 NW Crystal Structure and Polarity

III-V NWs have been found to exhibit a variety of crystal structures, with the two most common being the cubic zinc blende (ZB) structure and the hexagonal wurtzite (WZ) structure. MOCVD-grown GaAs and GaP NWs often adopt the ZB structure, while the WZ structure has been observed in MOCVD-grown InP NWs and MBE-grown GaAs NWs. The stacking of the bilayers that make up the crystal determines whether the structure is ZB or WZ. Twin planes and stacking faults are common types of planar defects in NWs. Twin planes occur in ZB structures when a single bilayer is faultily stacked, resulting in a reversed stacking sequence from ABC to CBA. Stacking faults in WZ structures occur when a single bilayer is misplaced.

The growth parameters determine the crystal structure of the NWs and the density of planar crystallographic defects. NW crystal structure can be determined by tilting the NW to the (110) zone axis in TEM, which allows ZB phases, WZ phases, twin defects and stacking faults to be distinguished. All TEM images and diffraction patterns presented in this thesis were taken along the (110) zone axis.

Ionic crystals have internal electric fields that impact many physical properties, such as the electronic structure and local charge distribution. Polarity in compound semiconductors arises from partial ionicity in chemical bonds, forming atomic pairs with opposite partial charges, called "dumbbells". [50] In NWs, only a specific polarity drives unidirectional growth and can influence growth mechanisms, orientation and even lead to new nanostructure formation. Polarity-driven growth mechanisms can explain kinking in some semiconductor NW heterostructures. However, maintaining

polarity along the NW and through twin boundaries remains an important issue. Twins occur from 180° rotations of the structure along the [111] or [0001] growth axes, with 'ortho' twins conserving polarity across the boundary and 'para' twins not. Figure 2.5 shows an example of typical GaAs NW polarity.

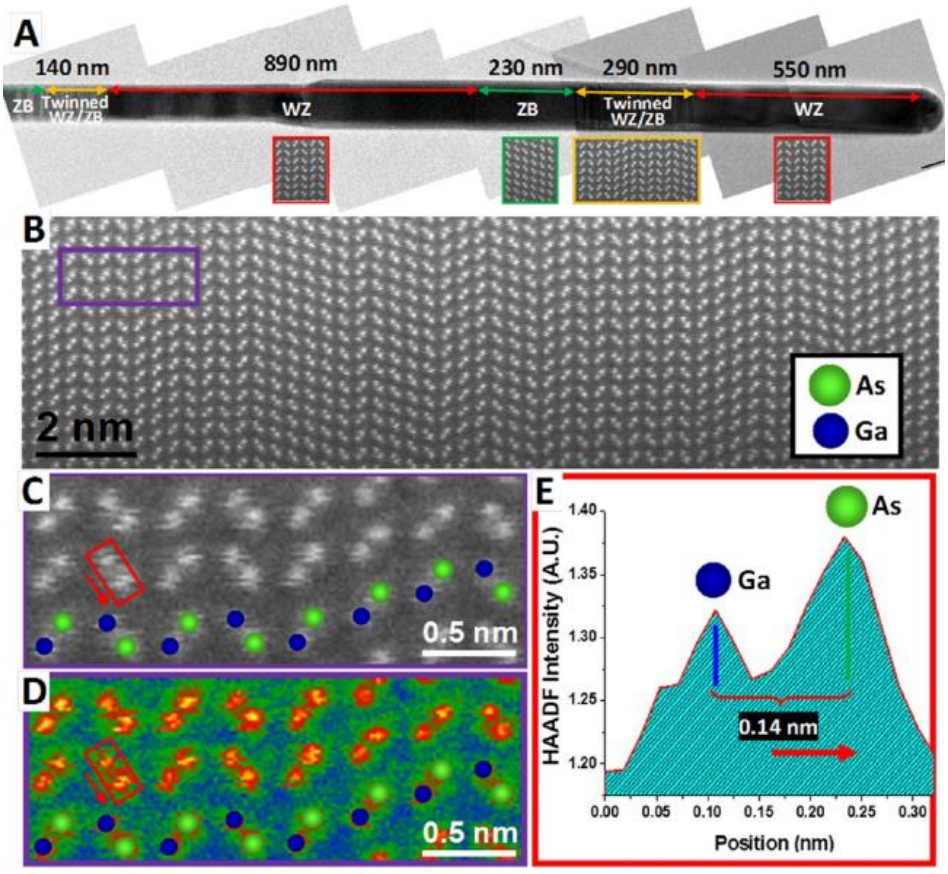

Figure 2.5 (A) TEM view of the GaAs NWs with modulated polytypic structure. (B) Atomic resolution aberration corrected HAADF-STEM detail of the Ga−As dumbbell pairs in a selected region of the visualised GaAs NW. (C) Raw HAADF-STEM magnified detail of the squared region in B. (D) False colour detail of the same region in (C) to enhance the contrast. (E) HAADF intensity profile obtained across the Ga−As dumbbell pair indicated by the red squared region in (C) and (D). The red arrow points the growth direction.[50]

2.4.7 Significance of passivation

Although NWs offer superior and unique properties compared to bulk material, they do have one significant disadvantage: their high surface-to-volume ratio leads to a high density of surface states.[51] The surface states can function as nonradiative recombination centres or surface charge traps, creating additional electronic states within the bandgap, which can cause the Fermi level to be pinned (bent) at the surface.

III-V NWs, such as GaAs and InP, are particularly susceptible to this problem, with the severity of the pinning depending on the native oxide type and NW diameter. GaAs NWs are known to have the highest surface recombination velocity of charge carriers, resulting in strong Fermi level pinning. [52,53] In contrast, InP NWs have a significantly lower surface recombination velocity. [54] To use NWs in functional devices, effective passivating materials need to be explored to provide some degree of passivation and long-term protection from oxidation.

2.5 Quantum confinement

When the dimension of a crystal is reduced, quantum confinement significantly modifies the density of states. Rather than a smooth and continuous distribution, the energy states become packed in a narrow energy range. This concentration of discrete energy levels enhances the oscillator strength of the lowest level transitions. The magnitude of the density of states in the valence and conduction bands, as well as the overlap of the wavefunctions of electrons and holes, affect the oscillator strength of an inter-band optical transition. [55] In Type I semiconductors, both factors lead to a larger enhancement of the oscillator strength with increasing quantum confinement. Quantum dots, which are the most confined structures, maximise the oscillator strength. This effect is observed at any temperature. [56] Figure 2.6 depicts the density of states vs. energy for bulk material, quantum well, quantum wire and quantum dot.

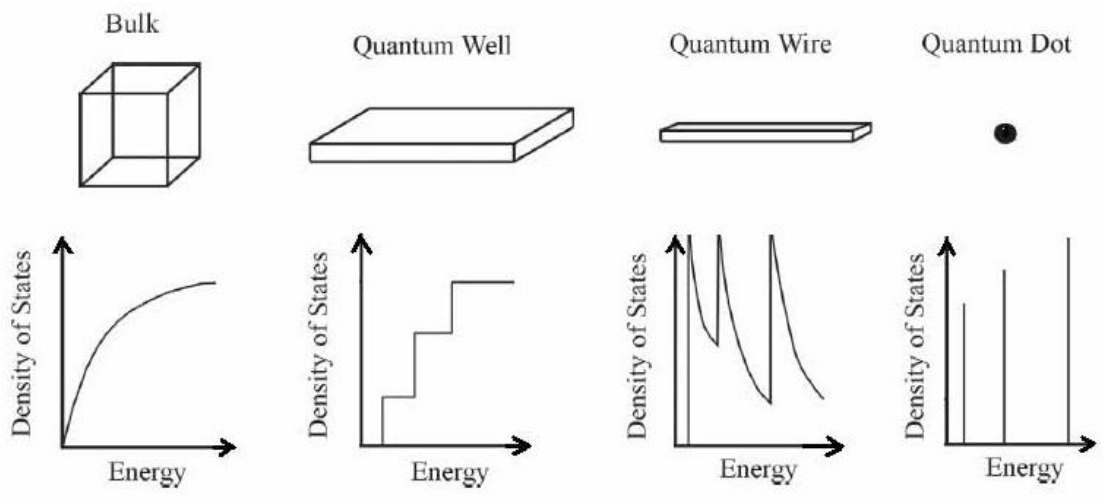

Figure 2.6 Density of states vs. energy for bulk material, quantum well, quantum wire and quantum dot. Reproduced from ref 49.

The quantum and interfacial effects become increasingly significant, leading to changes in the band structure of nanoscale semiconductors. Specifically, the bandgap widens, the core level shifts, and the sublevel separation within a band increases. When the dimension of the solid is reduced, nanostructured semiconductors exhibit similar changes in their electronic and optical properties, which can be summarised as follows. [55] The bandgap widens, resulting in a blue shift in the photoluminescence (PL). The energy levels of the core bands and the adsorbate-induced chemical shifts move towards higher binding energy in absolute value. X-ray photoelectron spectroscopy (XPS) has shown that the main core-level peaks and oxide satellites of various elements move upwards simultaneously, and the amount of change depends on the original core-level position and the nanocrystal size.[57]

2.5.1 Quantum confinement effect in III-V NWs

The drive for smaller electronic and optoelectronic devices and the desire to gain a better understanding of nanoscale chemistry and physics have led to a recent interest in low-dimensional III-V compound semiconductor materials. III-V films can be size-

engineered in the growth direction, and lateral confinement can be achieved using lithographic techniques or self-assembled growth, such as with V-grooves[58], patterned substrate[59,60], cleaved edge overgrowth [61], tilted or serpentine superlattices[62,63], or self-organizing quantum dots[64,65]. Research advances in III-V semiconductor quantum structures with a focus on laterally confined structures where self-assembly processes play an important role along with the effect of atomic-scale size-fluctuations on confined energy levels in these quantum structures are reviewed [62].

Of particular interest is one dimensional (1D) system, which holds promise from both fundamental and applied perspectives. High quality, well-defined 1D nanostructures are necessary for various applications such as sensors and interconnects. However, progress in this field has been impeded by the challenge of synthesising materials of controlled size, structure and composition in the 1D size regime.

The confinement of carriers in two dimensions is a characteristic of 1D nanostructures, which restricts electron/hole transportation to only one dimension. Various studies have investigated NWs with cross-sectional sizes ranging from 30-100 nm; however, electronic confinement properties are only achieved when the size falls below the exciton Bohr radius. For semiconductors such as GaAs, InP, and Si, this radius is below 20 nm. While it is possible to produce GaAs NWs with diameters below 10 nm using non-epitaxial methods like solution-liquid-solid[66] and laser catalytic growth[67] via laser ablation technique to grow NWs with the VLS method, these approaches typically yield NWs with suboptimal diameter control and random orientation. Consequently, the experimental investigation of quantum properties of NWs as 1D quantum wires has been limited by the challenge of producing quantum confined NWs with high yield.

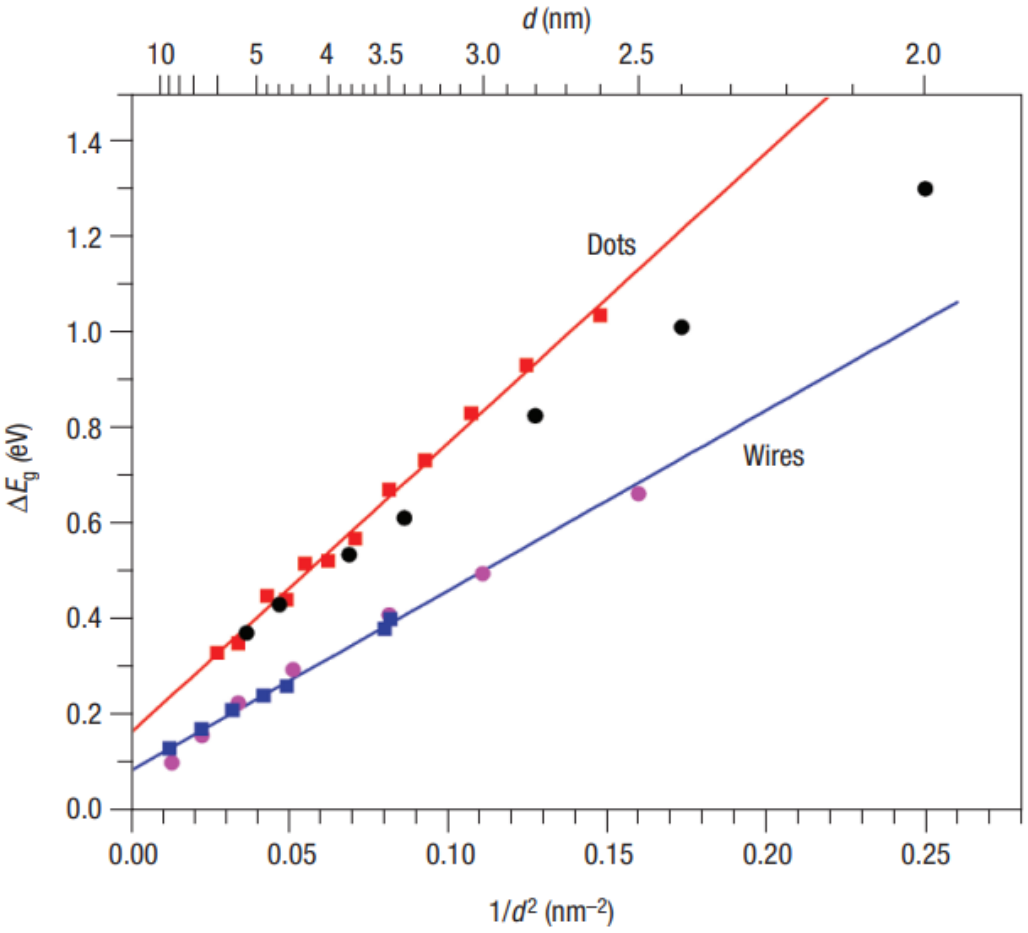

Figure 2.7 Experimental InP quantum-dot (red squares) and quantum-wire (blue squares) data plotted as ΔEg versus $1/d^2$. The results of theoretical data of semiempirical pseudopotential calculations are shown for InP quantum dots (black circles) and quantum wires (purple circles).Reproduced from ref 62.

The size-dependent evolution of bandgaps in one-dimensional (1D) confined wells, 2D-confined wires, and 3D-confined dots is expected to be different due to the varying dimensionality of confinement. E. Buhro *et. al*, conducted a systematic experimental comparison between analogous 1D, 2D, or 3D confinement systems.[68] In their study, InP quantum wires with diameters in the strong-confinement regime were grown, and their bandgaps (shown with blue squares in Figure 2.7) were compared with those previously reported for InP quantum dots (shown with red squares in Figure 2.7). The

authors also provide theoretical evidence to establish that the quantum confinement observed in the InP wires (represented by black circles in figure 2.7) is weakened to the expected extent, relative to that in InP dots (represented by purple circles in Figure 2.7), by the loss of one confinement dimension. It is worth noting that quantum wires can sometimes behave like strings of quantum dots. Therefore, the authors proposed an analysis to generally distinguish between quantum-wire and quantum-dot behaviour.

A recent epitaxial growth and characterisation study have developed a novel reverse-reaction fabrication method that can produce ultrathin, catalyst-free GaAs NWs epitaxially on silicon with record low diameters of approximately 7 nm.[69] These NWs exhibit stability in the bulk zinc blende phase. Owing to their well-oriented epitaxial nature, these low-diameter GaAs NWs can be overgrown with homogeneous AlGaAs shells to create highly efficient quantum wires. The authors conducted correlated structural and optical studies on identical NWs, which revealed strong cross-sectional size-dependent quantum confinement, as demonstrated by significant blue shifted photoluminescence emission of up to approximately 100 meV when compared to bulk-like band-edge emission. To simulate the measured confinement properties, an effective mass model was used to determine the respective ground state energy shifts of the electron and hole wave functions confined in hexagonally shaped NW cross-sections. The results of the simulation were found to be in good agreement with the experimental data. These findings indicate the potential for exploring interesting mesoscopic phenomena and enabling performance enhancements in related optical and electrical devices by exploiting the 1D electronic nature of free-standing GaAs-based and other III-V semiconductor NWs.

Up until now, the focus of research has predominantly been on the effects of quantum confinement on the bandgap of materials. However, it becomes important to study the

electronic structure, as well as the electrical and thermal properties of NWs when their dimensions are well below the Bohr exciton radius. For instance, theoretical predictions suggest a direct to indirect bandgap transition in GaAs NWs below a critical diameter of 4 nm.[70] The exploration of such possibilities with ultra-thin NWs is both experimentally exciting and demanding. In Chapter 5 of this thesis, the various physical properties of the ultra-thin GaAs quantum wires synthesised on synthetic mica are investigated.

2.5.2 Bond-Order-Bond-Length-Strength (B-OLS) mechanism

A mechanism called the bond-order–bond-length–bond-strength (bond-OLS) correlation has been proposed by Sun *et. al*, which helps to explain the relationship between the shape, size and properties of nanomaterials.[71] According to the proposed mechanism, imperfections in the coordination number of atoms on a surface cause the remaining bonds of the lower-coordinated surface atom to relax spontaneously. This relaxation leads to an increase in bond energy, which affects not only the cohesive energy of the surface atom but also the energy density in the relaxed region. The cohesive energy is related to thermodynamic properties, such as self-assembly, phase transition and thermal stability of a nanosolid.

The increase in binding energy density affects the system Hamiltonian and related properties, such as the bandgap, core-level shift, phonon frequency and dielectrics of a nanosolid. These properties change as the surface curvature and the portion of surface atoms vary with particle size.

2.6 References

(1) Han, Y.; Lau, K. M. III-V Lasers Selectively Grown on (001) Silicon. *J. Appl. Phys.* **2020**, *128* (20), 200901. https://doi.org/10.1063/5.0029804.

(2) Han, Y.; Yan, Z.; Ng, W. K.; Xue, Y.; Ng, K. W.; Wong, K. S.; Lau, K. M. III-V Micro- And Nano-Lasers Deposited on Amorphous SiO2. *Appl. Phys. Lett.* **2020**, *116* (17), 172102. https://doi.org/10.1063/5.0008144.

(3) Du, Y.; Xu, B.; Wang, G.; Miao, Y.; Li, B.; Kong, Z.; Dong, Y.; Wang, W.; Radamson, H. H. Review of Highly Mismatched III-V Heteroepitaxy Growth on (001) Silicon. *Nanomaterials* **2022**, *12* (5), 741. https://doi.org/10.3390/nano12050741.

(4) Weisbuch, C. Review—On The Search for Efficient Solid State Light Emitters: Past, Present, Future. *ECS J. Solid State Sci. Technol.* **2020**, *9* (1), 016022. https://doi.org/10.1149/2.0392001jss.

(5) Zhou, C.; Ghods, A.; Saravade, V. G.; Patel, P. V.; Yunghans, K. L.; Ferguson, C.; Feng, Y.; Kucukgok, B.; Lu, N.; Ferguson, I. T. Review—The Current and Emerging Applications of the III-Nitrides. *ECS J. Solid State Sci. Technol.* **2017**, *6* (12), Q149–Q156. https://doi.org/10.1149/2.0101712jss.

(6) Han, Y.; Yan, Z.; Ng, W. K.; Xue, Y.; Wong, K. S.; Lau, K. M. Bufferless 15 Mm III-V Lasers Grown on Si-Photonics 220 Nm Silicon-on-Insulator Platforms. *Optica* **2020**, *7* (2), 148. https://doi.org/10.1364/optica.381745.

(7) Zhou, Z.; Yin, B.; Michel, J. On-Chip Light Sources for Silicon Photonics. *Light Sci. Appl.* **2015**, *4* (11), e358. https://doi.org/10.1038/lsa.2015.131.

(8) Kim, H.; Chang, T. Y.; Lee, W. J.; Huffaker, D. L. III-V Nanowire Array Telecom Lasers on (001) Silicon-on-Insulator Photonic Platforms. *Appl. Phys. Lett.* **2019**, *115*

(21), 3101. https://doi.org/10.1063/1.5126721.

(9) Saxena, D.; Mokkapati, S.; Parkinson, P.; Jiang, N.; Gao, Q.; Tan, H. H.; Jagadish, C. Optically Pumped Room-Temperature GaAs Nanowire Lasers. *Nat. Photonics* **2013**, *7* (12), 963–968. https://doi.org/10.1038/nphoton.2013.303.

(10) Baek, H.; Lee, C. H.; Chung, K.; Yi, G. C. Epitaxial GaN Microdisk Lasers Grown on Graphene Microdots. *Nano Lett.* **2013**, *13* (6), 2782–2785. https://doi.org/10.1021/nl401011x.

(11) Wong, W. W.; Su, Z.; Wang, N.; Jagadish, C.; Tan, H. H. Epitaxially Grown InP Micro-Ring Lasers. *Nano Lett.* **2021**, *21* (13), 5681–5688. https://doi.org/10.1021/acs.nanolett.1c01411.

(12) Zhang, Y.; Saxena, D.; Aagesen, M.; Liu, H. Toward Electrically Driven Semiconductor Nanowire Lasers. *Nanotechnology* **2019**, *30* (19), 192002. https://doi.org/10.1088/1361-6528/ab000d.

(13) Mauthe, S.; Baumgartner, Y.; Sousa, M.; Ding, Q.; Rossell, M. D.; Schenk, A.; Czornomaz, L.; Moselund, K. E. High-Speed III-V Nanowire Photodetector Monolithically Integrated on Si. *Nat. Commun.* **2020**, *11* (1), 1–7. https://doi.org/10.1038/s41467-020-18374-z.

(14) Esmaeil Zadeh, I.; Chang, J.; Los, J. W. N.; Gyger, S.; Elshaari, A. W.; Steinhauer, S.; Dorenbos, S. N.; Zwiller, V. Superconducting Nanowire Single-Photon Detectors: A Perspective on Evolution, State-of-the-Art, Future Developments, and Applications. *Appl. Phys. Lett.* **2021**, *118* (19), 190502. https://doi.org/10.1063/5.0045990.

(15) Lapierre, R. R.; Robson, M.; Azizur-Rahman, K. M.; Kuyanov, P. A Review of III-V Nanowire Infrared Photodetectors and Sensors. *J. Phys. D. Appl. Phys.* **2017**, *50* (12),

123001. https://doi.org/10.1088/1361-6463/aa5ab3.

(16) Anyebe, E. A.; Sandall, I.; Jin, Z. M.; Sanchez, A. M.; Rajpalke, M. K.; Veal, T. D.; Cao, Y. C.; Li, H. D.; Harvey, R.; Zhuang, Q. D. Optimization of Self-Catalyzed InAs Nanowires on Flexible Graphite for Photovoltaic Infrared Photodetectors. *Sci. Rep.* **2017**, *7* (December 2016), 1–9. https://doi.org/10.1038/srep46110.

(17) Chugh, D.; Adhikari, S.; Wong-Leung, J.; Lysevych, M.; Jagadish, C.; Tan, H. H. Improving the Morphology and Crystal Quality of AlN Grown on Two-Dimensional HBN. *Cryst. Growth Des.* **2020**, *20* (3), 1811–1819. https://doi.org/10.1021/acs.cgd.9b01543.

(18) Xu, Y.; Cao, B.; Li, Z.; Cai, D.; Zhang, Y.; Ren, G.; Wang, J.; Shi, L.; Wang, C.; Xu, K. Growth Model of van Der Waals Epitaxy of Films: A Case of AlN Films on Multilayer Graphene/SiC. *ACS Appl. Mater. Interfaces* **2017**, *9* (50), 44001–44009. https://doi.org/10.1021/acsami.7b14494.

(19) Saraswathy Vilasam, A. G.; Prasanna, P. K.; Yuan, X.; Azimi, Z.; Kremer, F.; Jagadish, C.; Chakraborty, S.; Tan, H. H. Epitaxial Growth of GaAs Nanowires on Synthetic Mica by Metal–Organic Chemical Vapor Deposition. *ACS Appl. Mater. Interfaces* **2022**, *14* (2), 3395–3403. https://doi.org/10.1021/acsami.1c19236.

(20) Anyebe, E. A.; Kesaria, M. Recent Advances in the Van Der Waals Epitaxy Growth of III-V Semiconductor Nanowires on Graphene. *Nano Sel.* **2021**, *2* (4), 688–711. https://doi.org/10.1002/nano.202000142.

(21) Koma, A. Van Der Waals Epitaxy for Highly Lattice-Mismatched Systems. *J. Cryst. Growth* **1999**, *201–202*, 236–241. https://doi.org/10.1016/S0022-0248(98)01329-3.

(22) Lin, Z.; Mcnamara, A.; Liu, Y.; Moon, K. sik; Wong, C. P. Exfoliated Hexagonal

Boron Nitride-Based Polymer Nanocomposite with Enhanced Thermal Conductivity for Electronic Encapsulation. *Compos. Sci. Technol.* **2014**, *90*, 123–128. https://doi.org/10.1016/j.compscitech.2013.10.018.

(23) Wallentin, J.; Kriegner, D.; Stangl, J.; Borgström, M. T. Au-Seeded Growth of Vertical and in-Plane III-V Nanowires on Graphite Substrates. *Nano Lett.* **2014**, *14* (4), 1707–1713. https://doi.org/10.1021/nl403411w.

(24) Hong, Y. J.; Yang, J. W.; Lee, W. H.; Ruoff, R. S.; Kim, K. S.; Fukui, T. Van Der Waals Epitaxial Double Heterostructure: InAs/Single-Layer Graphene/InAs. *Adv. Mater.* **2013**, *25* (47), 6847–6853. https://doi.org/10.1002/adma.201302312.

(25) Meyer-Holdt, J.; Kanne, T.; Sestoft, J. E.; Gejl, A.; Zeng, L.; Johnson, E.; Olsson, E.; Nygård, J.; Krogstrup, P. Ag-Catalyzed InAs Nanowires Grown on Transferable Graphite Flakes. *Nanotechnology* **2016**, *27* (36), 365603. https://doi.org/10.1088/0957-4484/27/36/365603.

(26) Munshi, A. M.; Dheeraj, D. L.; Fauske, V. T.; Kim, D. C.; Van Helvoort, A. T. J.; Fimland, B. O.; Weman, H. Vertically Aligned GaAs Nanowires on Graphite and Few-Layer Graphene: Generic Model and Epitaxial Growth. *Nano Lett.* **2012**, *12* (9), 4570–4576. https://doi.org/10.1021/nl3018115.

(27) Sundaram, S.; Vuong, P.; Mballo, A.; Ayari, T.; Karrakchou, S.; Patriarche, G.; Voss, P. L.; Salvestrini, J. P.; Ougazzaden, A. MOVPE of GaN-Based Mixed Dimensional Heterostructures on Wafer-Scale Layered 2D Hexagonal Boron Nitride - A Key Enabler of III-Nitride Flexible Optoelectronics. *APL Mater.* **2021**, *9* (6), 061101. https://doi.org/10.1063/5.0049306.

(28) Yuan, X.; Yang, J.; He, J.; Tan, H. H.; Jagadish, C. Role of Surface Energy in Nanowire Growth. *J. Phys. D. Appl. Phys.* **2018**, *51* (28), 283002.

https://doi.org/10.1088/1361-6463/aac9f4.

(29) Hong, Y. J.; Lee, C.-H. Chapter Three – van Der Waals Heteroepitaxy of Semiconductor Nanowires. In *Semiconductors and Semimetals*; 2015; pp 125–172. https://doi.org/10.1016/bs.semsem.2015.07.002.

(30) Hong, Y. J.; Lee, W. H.; Wu, Y.; Ruoff, R. S.; Fukui, T. Van Der Waals Epitaxy of InAs Nanowires Vertically Aligned on Single-Layer Graphene. *Nano Lett.* **2012**, *12* (3), 1431–1436. https://doi.org/10.1021/nl204109t.

(31) Garnett, E. C.; Brongersma, M. L.; Cui, Y.; McGehee, M. D. Nanowire Solar Cells. *Annu. Rev. Mater. Res.* **2011**, *41*, 269–295. https://doi.org/10.1146/annurev-matsci-062910-100434.

(32) Raj, V.; Vora, K.; Fu, L.; Tan, H. H.; Jagadish, C. High-Efficiency Solar Cells from Extremely Low Minority Carrier Lifetime Substrates Using Radial Junction Nanowire Architecture. *ACS Nano* **2019**, *13* (10), 12015–12023. https://doi.org/10.1021/acsnano.9b06226.

(33) Guo, H.; Wen, L.; Li, X.; Zhao, Z.; Wang, Y. Analysis of Optical Absorption in GaAs Nanowire Arrays. *Nanoscale Res. Lett.* **2011**, *6*, 1–6. https://doi.org/10.1186/1556-276X-6-617.

(34) Hoang, S.; Gao, P. X. Nanowire Array Structures for Photocatalytic Energy Conversion and Utilization: A Review of Design Concepts, Assembly and Integration, and Function Enabling. *Adv. Energy Mater.* **2016**, *6* (23), 1600683. https://doi.org/10.1002/aenm.201600683.

(35) Zhu, W.; Si, J.; Zhang, L.; Li, T.; Song, W.; Zhou, Y.; Yu, J.; Chen, R.; Feng, Y.; Wang, L. Growth of GaN on Monolayer Hexagonal Boron Nitride by Chemical Vapor

Deposition for Ultraviolet Photodetectors. *Semicond. Sci. Technol.* **2020**, *35* (12), 125025. https://doi.org/10.1088/1361-6641/abb71d.

(36) Lapierre, R. R.; Robson, M.; Azizur-Rahman, K. M.; Kuyanov, P. A Review of III-V Nanowire Infrared Photodetectors and Sensors. *J. Phys. D. Appl. Phys.* **2017**, *50* (12). https://doi.org/10.1088/1361-6463/aa5ab3.

(37) Li, W.; Yang, S.; Shamim, A. Screen Printing of Silver Nanowires: Balancing Conductivity with Transparency While Maintaining Flexibility and Stretchability. *npj Flex. Electron.* **2019**, *3* (1), 13. https://doi.org/10.1038/s41528-019-0057-1.

(38) Chung, K.; Beak, H.; Tchoe, Y.; Oh, H.; Yoo, H.; Kim, M.; Yi, G. C. Growth and Characterizations of GaN Micro-Rods on Graphene Films for Flexible Light Emitting Diodes. *APL Mater.* **2014**. https://doi.org/10.1063/1.4894780.

(39) Dai, X.; Messanvi, A.; Zhang, H.; Durand, C.; Eymery, J.; Bougerol, C.; Julien, F. H.; Tchernycheva, M. Flexible Light-Emitting Diodes Based on Vertical Nitride Nanowires. *Nano Lett.* **2015**, *15* (10), 6958–6964. https://doi.org/10.1021/acs.nanolett.5b02900.

(40) Gu, Z.; Song, Q.; Xiao, S. Nanowire Waveguides and Lasers: Advances and Opportunities in Photonic Circuits. *Front. Chem.* **2021**, *8* (January), 1–23. https://doi.org/10.3389/fchem.2020.613504.

(41) Claudon, J.; Bleuse, J.; Malik, N. S.; Bazin, M.; Jaffrennou, P.; Gregersen, N.; Sauvan, C.; Lalanne, P.; Gérard, J. M. A Highly Efficient Single-Photon Source Based on a Quantum Dot in a Photonic Nanowire. *Nat. Photonics* **2010**, *4* (3), 174–177. https://doi.org/10.1038/nphoton.2009.287.

(42) Mantynen, H.; Anttu, N.; Sun, Z.; Lipsanen, H. Single-Photon Sources with Quantum

Dots in III-V Nanowires. *Nanophotonics* **2019**, *8* (5), 747–769. https://doi.org/10.1515/nanoph-2019-0007.

(43) Mohammadnejad, S.; Mahmoudi, A.; Arab, H. A New III–V Nanowire-Quantum Dot Single Photon Source with Improved Purcell Factor for Quantum Communication. *Opt. Quantum Electron.* **2022**, *54* (4), 1–21. https://doi.org/10.1007/s11082-022-03567-1.

(44) Jia, C.; Lin, Z.; Huang, Y.; Duan, X. Nanowire Electronics: From Nanoscale to Macroscale. *Chem. Rev.* **2019**, *119* (15), 9074–9135. https://doi.org/10.1021/acs.chemrev.9b00164.

(45) Rurali, R. Colloquium: Structural, Electronic, and Transport Properties of Silicon Nanowires. *Rev. Mod. Phys.* **2010**, *82* (1), 427–449. https://doi.org/10.1103/RevModPhys.82.427.

(46) Hong, Y. J.; Lee, C.-H. *Semiconductor Nanowires I - Growth and Theory*; 2015. https://doi.org/10.1016/bs.semsem.2015.07.002.

(47) Frost, T.; Jahangir, S.; Stark, E.; Deshpande, S.; Hazari, A.; Zhao, C.; Ooi, B. S.; Bhattacharya, P. Monolithic Electrically Injected Nanowire Array Edge-Emitting Laser on (001) Silicon. *Nano Lett.* **2014**, *14* (8), 4535–4541. https://doi.org/10.1021/nl5015603.

(48) Prabaswara, A.; Min, J. W.; Zhao, C.; Janjua, B.; Zhang, D.; Albadri, A. M.; Alyamani, A. Y.; Ng, T. K.; Ooi, B. S. Direct Growth of III-Nitride Nanowire-Based Yellow Light-Emitting Diode on Amorphous Quartz Using Thin Ti Interlayer. *Nanoscale Res. Lett.* **2018**, *13*, 1–9. https://doi.org/10.1186/s11671-018-2453-1.

(49) Zhao, S.; Liu, X.; Wu, Y.; Mi, Z. An Electrically Pumped 239 Nm AlGaN Nanowire

Laser Operating at Room Temperature. *Appl. Phys. Lett.* **2016**, *109* (19), 191106. https://doi.org/10.1063/1.4967180.

(50) De La Mata, M.; Magen, C.; Gazquez, J.; Utama, M. I. B.; Heiss, M.; Lopatin, S.; Furtmayr, F.; Fernández-Rojas, C. J.; Peng, B.; Morante, J. R.; Rurali, R.; Eickhoff, M.; Fontcuberta I Morral, A.; Xiong, Q.; Arbiol, J. Polarity Assignment in ZnTe, GaAs, ZnO, and GaN-AlN Nanowires from Direct Dumbbell Analysis. *Nano Lett.* **2012**, *12* (5), 2579–2586. https://doi.org/10.1021/nl300840q.

(51) Dhaka, V.; Perros, A.; Naureen, S.; Shahid, N.; Jiang, H.; Kakko, J. P.; Haggren, T.; Kauppinen, E.; Srinivasan, A.; Lipsanen, H. Protective Capping and Surface Passivation of III-V Nanowires by Atomic Layer Deposition. *AIP Adv.* **2016**, *6* (1), 1–7. https://doi.org/10.1063/1.4941063.

(52) Lloyd-Hughes, J.; Merchant, S. K. E.; Fu, L.; Tan, H. H.; Jagadish, C.; Castro-Camus, E.; Johnston, M. B. Influence of Surface Passivation on Ultrafast Carrier Dynamics and Terahertz Radiation Generation in GaAs. *Appl. Phys. Lett.* **2006**, *89* (23), 3–5. https://doi.org/10.1063/1.2398915.

(53) Nelson, R. J.; Sobers, R. G. Minority-Carrier Lifetimes and Internal Quantum Efficiency of Surface-Free GaAs. *J. Appl. Phys.* **1978**, *49* (12), 6103–6108. https://doi.org/10.1063/1.324530.

(54) Joyce, H. J.; Wong-Leung, J.; Yong, C. K.; Docherty, C. J.; Paiman, S.; Gao, Q.; Tan, H. H.; Jagadish, C.; Lloyd-Hughes, J.; Herz, L. M.; Johnston, M. B. Ultralow Surface Recombination Velocity in InP Nanowires Probed by Terahertz Spectroscopy. *Nano Lett.* **2012**, *12* (10), 5325–5330. https://doi.org/10.1021/nl3026828.

(55) Sun, C. Q.; Tay, B. K.; Li, S.; Sun, X. W.; Lau, S. P.; Chen, T. P. Bandgap Expansion of a Nanometric Semiconductor. *Mater.Phys.Mech.* **2001**, *4* (May 2014), 129–133.

(56) Ahmed, I. A.; Hussein, H. S.; Ragab, A. H.; Al-Radadi, N. S. Synthesis and Characterization of Silica-Coated Oxyhydroxide Aluminum/Doped Polymer Nanocomposites: A Comparative Study and Its Application as a Sorbent. *Molecules* **2020**, *25* (7). https://doi.org/10.3390/molecules25071520.

(57) Sun, C. Q.; Chen, T. P.; Tay, B. K.; Li, S.; Zhang, Y. B.; Huang, H.; Pan, L. K.; Lau, S. P.; Sun, X. W. An Extended "quantum Confinement" Theory: Surface-Coordination Imperfection Modifies the Entire Band Structure of a Nanosolid. *J. Phys. D. Appl. Phys.* **2001**, *34* (24), 3470–3479. https://doi.org/10.1088/0022-3727/34/24/308.

(58) Ducommun, Y.; Martinet, E.; Weman, H.; Biasiol, G.; Gustafsson, A.; Kapon, E. Structure and Optical Properties of V-Groove Quantum Wire Superlattices. *Phys. E Low-Dimensional Syst. Nanostructures* **1998**, *2* (1–4), 954–958. https://doi.org/10.1016/S1386-9477(98)00195-7.

(59) Benyoucef, M.; Usman, M.; Alzoubi, T.; Reithmaier, J. P. Pre-Patterned Silicon Substrates for the Growth of III-V Nanostructures. *Phys. Status Solidi Appl. Mater. Sci.* **2012**, *209* (12), 2402–2410. https://doi.org/10.1002/pssa.201228367.

(60) Benyoucef, M.; Reithmaier, J. P. Direct Growth of III-V Quantum Dots on Silicon Substrates: Structural and Optical Properties. *Semicond. Sci. Technol.* **2013**, *28* (9), 094004. https://doi.org/10.1088/0268-1242/28/9/094004.

(61) Sun, Q.; Gao, H.; Zhang, X.; Yao, X.; Xu, S.; Zheng, K.; Chen, P.; Lu, W.; Zou, J. High-Quality Epitaxial Wurtzite Structured InAs Nanosheets Grown in MBE. *Nanoscale* **2020**, *12* (1), 271–276. https://doi.org/10.1039/c9nr08429k.

(62) Gossard, A. C.; Fafard, S. Quantum-Engineering of III-V Semiconductor Structures. *Solid State Commun.* **1994**, *92* (1–2), 63–70. https://doi.org/10.1016/0038-1098(94)90859-1.

(63) Chang Yi, J.; Dagli, N. Optical Properties of Serpentine Superlattices on GaAs Vicinal Substrates for Quantum Wire Laser Applications. *Appl. Phys. Lett.* **1992**, *61* (2), 219–221. https://doi.org/10.1063/1.108223.

(64) Fukui, T.; Notzel, R.; Temmyo, J.; Kozen, A.; Tamamura, T.; Hasegawa, H.; Ingaas, S. SELF-ORGANIZED GROWTH OF QUANTUM-DOT STRUCTURES. **1996**, *40* (1), 777–783.

(65) Hapter, C. S YNTHESIS AND C HARACTERIZATION OF C APPED ZnS Q UANTUM D OTS. **1999**, No. October, 62–94.

(66) Dong, A.; Yu, H.; Wang, F.; Buhro, W. E. Colloidal GaAs Quantum Wires: Solution-Liquid-Solid Synthesis and Quantum-Confinement Studies. *J. Am. Chem. Soc.* **2008**, *130* (18), 5954–5961. https://doi.org/10.1021/ja711408t.

(67) Gudiksen, M. S.; Lieber, C. M. Diameter-Selective Synthesis of Semiconductor Nanowires [13]. *J. Am. Chem. Soc.* **2000**, *122* (36), 8801–8802. https://doi.org/10.1021/ja002008e.

(68) Yu, H.; Li, J.; Loomis, R. A.; Wang, L. W.; Buhro, W. E. Two-versus Three-Dimensional Quantum Confinement in Indium Phosphide Wires and Dots. *Nat. Mater.* **2003**, *2* (8), 517–520. https://doi.org/10.1038/nmat942.

(69) Loitsch, B.; Rudolph, D.; Morkötter, S.; Döblinger, M.; Grimaldi, G.; Hanschke, L.; Matich, S.; Parzinger, E.; Wurstbauer, U.; Abstreiter, G.; Finley, J. J.; Koblmüller, G. Tunable Quantum Confinement in Ultrathin, Optically Active Semiconductor Nanowires Via Reverse-Reaction Growth. *Adv. Mater.* **2015**, *27* (13), 2195–2202. https://doi.org/10.1002/adma.201404900.

(70) Persson, M. P.; Xu, H. Q. Electronic Structure of Nanometer-Scale GaAs Whiskers.

Appl. Phys. Lett. **2002**, *81* (7), 1309–1311. https://doi.org/10.1063/1.1498871.

(71) Sun, C. Q.; Tay, B. K.; Zeng, X. T.; Li, S.; Chen, T. P.; Zhou, J.; Bai, H. L.; Jiang, E. Y. Bond-Order-Bond-Length-Bond-Strength (Bond-OLS) Correlation Mechanism for the Shape-and-Size Dependence of a Nanosolid. *J. Phys. Condens. Matter* **2002**, *14* (34), 7781–7795. https://doi.org/10.1088/0953-8984/14/34/301.

Chapter 3

Experimental Techniques

3.1 Introduction

This chapter provides an overview of the various experimental and theoretical methods used for the growth of III-V compound semiconductors, with a specific focus on GaAs grown on synthetic mica. The chapter is divided into several sections, with each section covering a particular topic. In section 3.2, the essential experimental methods used for epitaxy and deposition are discussed, including metal-organic chemical vapour deposition (MOCVD), electron beam evaporation and atomic layer deposition (ALD) in sub-sections 3.2.1, 3.2.2 and 3.2.3, respectively. Section 3.3, focuses on the growth methodology, including gold-seeded nanowire growth using (a) vapour-liquid-solid (VLS) techniques, (b) substrate preparation, and (c) catalyst-free growth. The characterisation tools used to analyse the grown material system are covered in section 3.4, which includes 3.4.1 on Raman spectrometry, 3.4.2 on atomic force microscopy (AFM) and various electron microscopy techniques such as 3.4.3 scanning electron microscopy (SEM), 3.4.4 transmission electron microscopy (TEM), with subsection (a) high resolution transmission electron microscopy (HRTEM) (b) scanning transmission electron microscopy (STEM), and (c) energy-dispersive X-ray spectroscopy (EDS). Section 3.4.5 focuses on photoluminescence spectroscopy, and section 3.4.6 covers X-ray diffraction (XRD) techniques such as (a) high-resolution X-ray diffraction (HRXRD), (b) grazing incidence X-ray diffraction (GIXRD), and the (c) rocking curve technique in XRD. Finally, section 3.4.7 covers photoelectron spectroscopy (X-ray and Ultraviolet) and 3.4.8 van der Pauw Hall measurement and finally section 3.5 provides the references.

3.2 Epitaxial growth and deposition techniques

3.2.1 Metal-Organic Chemical Vapour Deposition (MOCVD)

In this thesis, MOCVD technique is employed to grow III-V compound semiconductor nanowires on 2D templates. All the III-V nanowires and thin films were grown at the Australian National University.

MOCVD is an epitaxial growth technique that can achieve high growth rates and abrupt interfaces. Despite its requirement for costly and hazardous precursors, it can produce virtually any III-V and II-VI compound semiconductors. For a detailed explanation of the MOCVD technique, refer to the book by Stringfellow. [1] An AIXTRON 200/4 horizontal flow reactor was used for epitaxial growth, as illustrated in Figure 3.1. The III-V precursors were composed of metal-organic (organometallic or metal alkyl) and hydride precursors for group III and group V atoms, respectively. For example, trimethylgallium ($Ga(CH_3)_3$, TMGa), trimethyl aluminium ($Al(CH_3)_3$, TMAl), and trimethylindium ($In(CH_3)_3$, TMIn) were used as the metal-organic precursors for group III atoms (Ga, Al, and In). Arsine (AsH_3) was used to supply group V atoms (As).

To store the metal-organic sources, stainless steel cylinders called bubblers were used. These bubblers were kept at constant pressures and immersed in temperature-controlled baths. The hydrides are stored in high-pressure cylinders and directly supplied to the reactor.

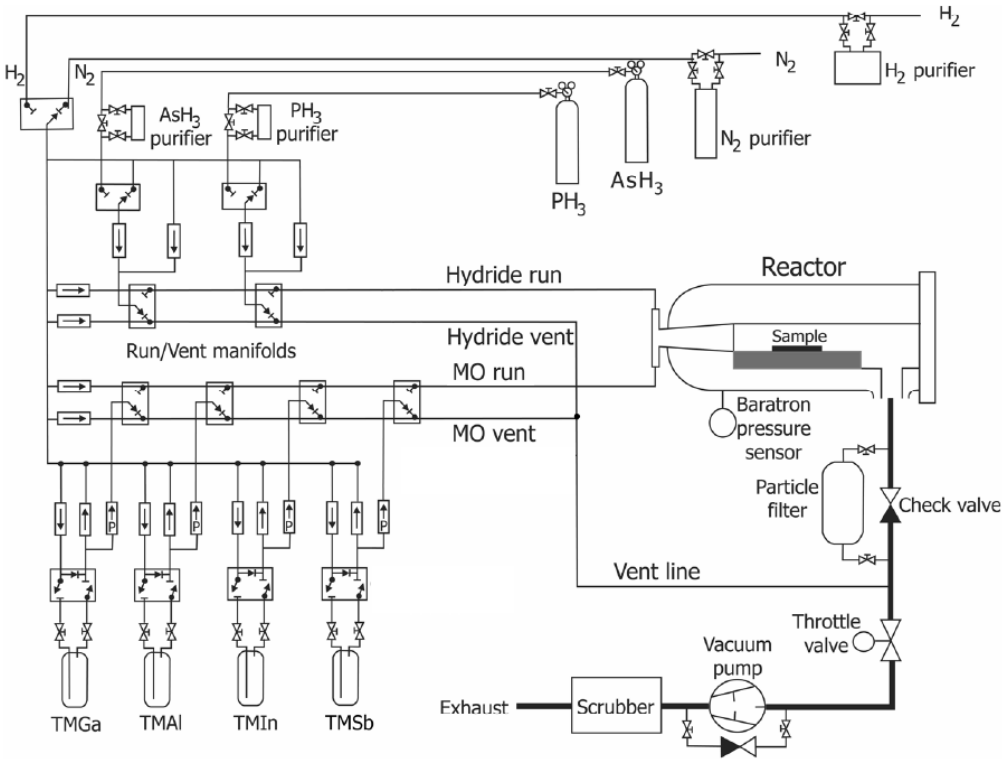

Fig 3.1 Schematic illustration of the Aixtron 200/4 MOCVD reactor. [2]

MOCVD employs ultra-high purity hydrogen, which is purified by passing high purity H_2 through a palladium-silver alloy membrane, as the carrier gas. The carrier gas is directed into the bubblers to transport the vapour of metal-organic compounds into the reaction chamber. Separate supply lines called MO run and Hydride run ensure that the metal-organic and hydride precursors are transported into the reaction chamber separately to prevent pre-reactions. A parallel vent line carries unspent gases into the exhaust, stabilising the source flow rate. The source flow is switched into the run line only after the flow rate is stabilized. The total gas flow rate for MO run is maintained at 10,000 standard cubic centimetre per minute (sccm), and for Hydride run, it is kept at 5000 sccm. During growth, the reactor pressure is maintained at 100 mbar.

The reaction chamber employs a silicon carbide coated graphite susceptor with gas foil rotation plates to hold the substrates. The susceptor follows a main planetary rotation, while the three plates have a satellite rotation to ensure highly uniform deposition. The

susceptor is heated using a three-zone infrared lamp arrangement surrounding the reaction chamber, and its temperature is measured by a thermocouple.

In this thesis, we examine the growth of GaAs and AlGaAs material systems through pyrolysis reactions that occur in the reaction chamber. Specifically, the following reactions take place:

$$Ga(CH_3)_3 + AsH_3 \rightarrow GaAs + 3CH_4$$

$$Al(CH_3)_3 + Ga(CH_3)_3 + 2AsH_3 \rightarrow AlGaAs + 6CH_4$$

Different combinations of precursors allow for the deposition of different materials and alloys with varying compositions including ternary materials such as AlGaAs. During the growth process, we adjust the precursor flow rate to control the chemical composition and deposition rate. To remove toxic compounds from the exhausted gas mixture, an activated charcoal scrubber is used, which results in the release of only diluted hydrogen into the atmosphere.

3.2.2 Electron beam (e-beam) vaporation

E-beam evaporation is preferred for the direct transfer of electron energy to the material, making it suitable for evaporating and depositing high melting point metals. In this thesis, the contact pads for electrical measurements were deposited using a Temescal BJD-2000 e-beam evaporator system. The system features a six-pocket e-gun and one-position thermal evaporation. The vacuum chamber comprises of a scroll pump and a cryo-pump, which together enable a vacuum range in the mid 10^{-7} mbar. A schematic of the e-beam deposition system is shown in figure 3.2.

The samples were mounted on a rotating sample holder during the deposition process. A high-energy electron beam is used to evaporate the material from a metal crucible.

The evaporated material then condenses on the substrate, which is maintained at a relatively low temperature compared to the crucible. [3] The electron beam is generated by applying a high voltage of several kilovolts to a tungsten filament within the chamber.

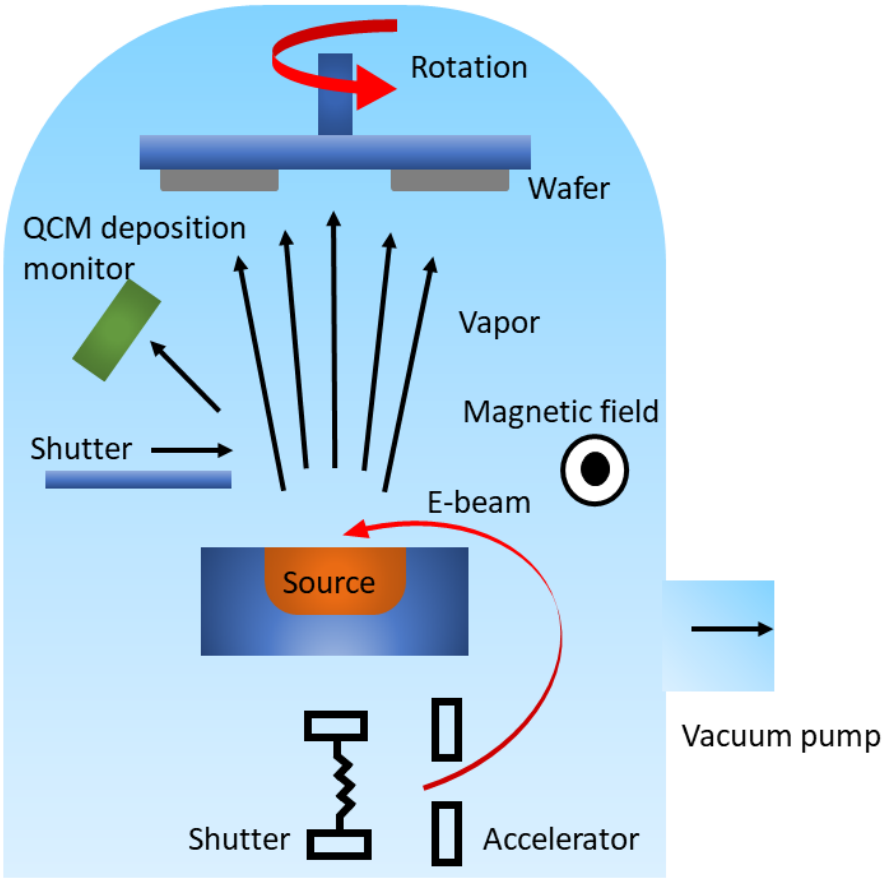

Fig 3.2 Schematic illustration of the electron beam evaporation system.

A directional magnetic field is used to direct the electron beam towards the metal crucible, resulting in the evaporation of the material. This technique is ideal for producing highly uniform, thin films with excellent adhesion to the substrate.

3.2.3 Atomic Layer Deposition (ALD)

(ALD is a versatile thin-film deposition technique that has gained considerable attention in recent years due to its ability to precisely control the thickness and composition of the deposited films at the atomic level. ALD utilizes self-limiting surface reactions to deposit thin films one atomic layer at a time, resulting in excellent uniformity, conformality and thickness control over complex substrates. [4] In this dissertation, a Picosun R-200 ALD system is used to deposit thin films for electrical contact pads/ passivation layers.

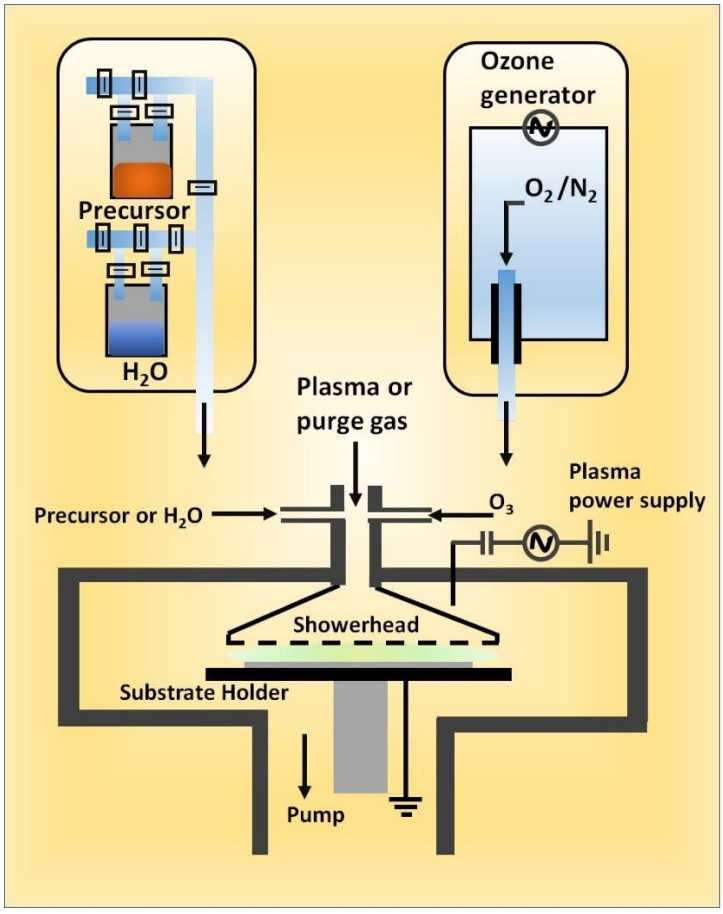

Fig 3.3 Schematic illustration of the atomic layer deposition (ALD).

ALD is a cyclic process that involves the sequential exposure of a substrate to alternating precursors. The precursors are typically gaseous and contain the elements

to be deposited. During the first half of the cycle, the substrate is exposed to the first precursor, which chemisorbs on the surface, leaving a self-limiting monolayer. Excess precursor is then purged from the chamber, and the substrate is exposed to the second precursor, which reacts with the first monolayer to form a new layer. The process is repeated until the desired thickness is achieved. Figure 3.3 shows the schematic of the ALD deposition process.

The self-limiting nature of the process ensures that each layer is uniform and conformal, with excellent step coverage over complex geometries. The deposition rate can be precisely controlled by adjusting the exposure time of each precursor and the number of cycles, making ALD a highly versatile technique for depositing a wide range of materials, including metals, oxides, nitrides and sulphides. [5,6]

ALD has several advantages over other thin-film deposition techniques. Firstly, the self-limiting nature of the process ensures excellent uniformity and thickness control, even over complex substrates. Secondly, ALD is a low-temperature process, typically performed at temperatures below 300 °C, making it compatible with a wide range of substrates, including certain plastics, glass and semiconductors. Thirdly, the process is highly reproducible and scalable, making it suitable for industrial-scale production. Finally, the ability to deposit precise thicknesses of multiple layers with varying compositions makes ALD ideal for fabricating complex multilayer structures with tailored properties.

3.3 Growth Methodology

3.3.1 Gold-seeded nanowire growth: Vapour-Liquid-Solid (VLS) growth

VLS is a technique used for the growth of nanowires. The basic idea behind VLS is to use a liquid metal catalyst to initiate the growth of a nanowire from a vapour-phase precursor. [7]

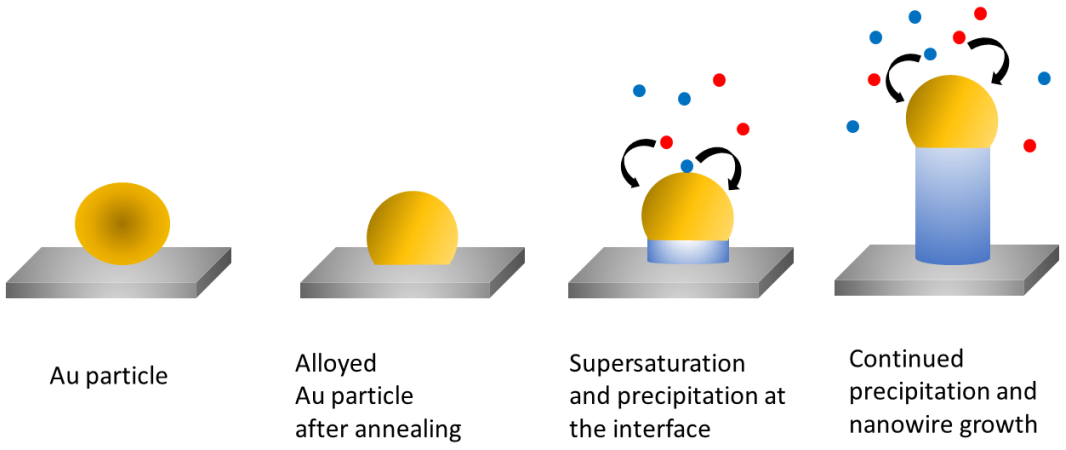

Figure 3.4: VLS growth mechanism.

A schematic of the VLS process is given in figure 3.4. The precursor gas reacts with the catalyst, forming a liquid droplet of the catalyst on the substrate surface. As the precursor gas continues to flow into the chamber, it is absorbed into the liquid droplet and reacts with the catalyst. This reaction creates a supersaturated solution of the precursor in the liquid droplet. Once the concentration of the precursor in the liquid droplet reaches a critical value, the supersaturated solution becomes unstable and the precursor begins to nucleate onto the surface of the catalyst droplet. The newly formed nanowire grows out from the surface of the liquid droplet, with the catalyst acting as a "tip" or "seed" for the nanowire growth. The nanowire continues to grow as long as there is a supply of precursor gas in the chamber.

3.3.2 Substrate preparation

A two-dimensional layered material, synthetic mica was used as the substrate for gold-seeded VLS growth of nanowires. To deposit the Au nanoparticles on the substrate, a colloidal solution is employed in conjunction with poly-L-lysine (PLL) functionalisation. PLL, a positively charged polyelectrolyte, attracts negatively charged Au nanoparticles and immobilises them onto the substrate.[8] The nanoparticle deposition process consists of two steps: PLL functionalisation and gold nanoparticle deposition.

The PLL functionalisation process begins with immersing the substrate in PLL solution for 60 seconds, followed by rinsing with DI water and drying with a nitrogen gun. Next, Au colloidal solution is dispersed onto the substrate for 60 seconds, and the sample is subsequently rinsed with DI water and dried using a nitrogen gun.

3.3.3 Catalyst-free growth

For catalyst-free growth method in the thesis, few-layer h-BN on SiO_2/Si substrates acquired from Grolltex, USA, are used directly as the substrate for epitaxy.

3.4 Characterisation tools

3.4.1 Raman Spectrometry

Raman spectroscopy is a non-destructive and non-invasive technique that is commonly used to investigate the vibrational and structural properties of materials. It is based on the Raman effect, which occurs when a photon interacts with a molecule, causing it to vibrate. The scattered photon can either have less energy (Stokes scattering) or more energy (anti-Stokes scattering) than the incident photon, depending on the vibrational energy of the molecule. [9] The Raman spectrum of a material is a plot of the intensity of scattered photons as a function of their energy and can be used to identify the vibrational modes of the molecules in the material.

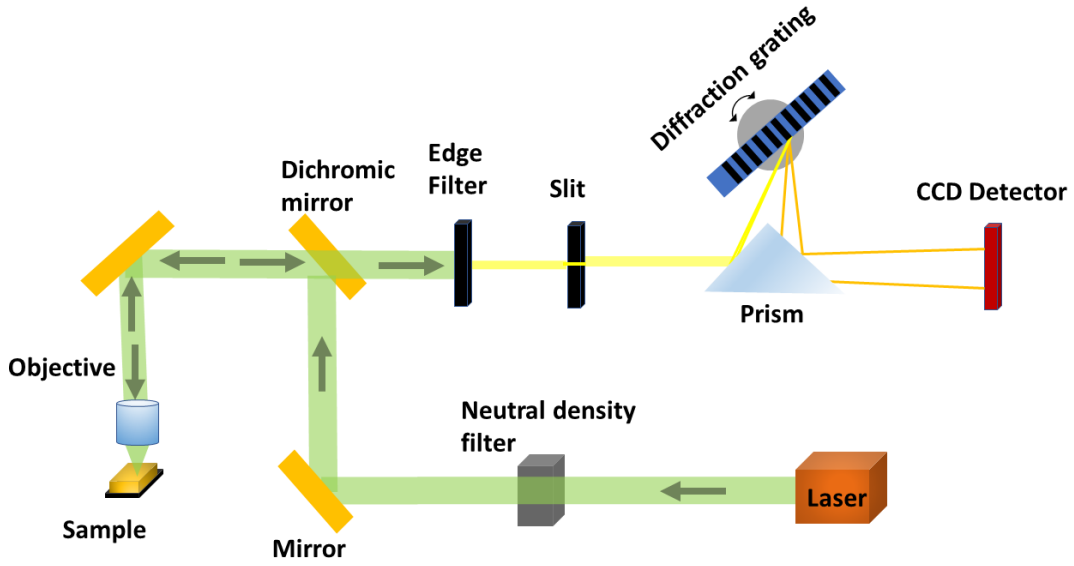

Figure 3.5 Schematic illustration of a typical Raman spectrometer.

Raman spectroscopy requires a laser as a source of excitation, which is typically in the visible or near-infrared range. The laser light is focused onto the sample, and the scattered light is collected and analysed using a spectrometer. Raman spectra can be obtained in either a backscattering geometry, where the laser and the detector are located on the same side of the sample, or a transmission geometry, where the laser and detector are on opposite sides of the sample. A schematic of a typical Raman system is given in figure 3.5. All the Raman spectra in this thesis are acquired using the Renishaw Raman system at the Australian National University.

3.4.2 Atomic Force Microscopy (AFM)

(AFM is a powerful technique for the topography imaging of surfaces at the nanoscale. It is a non-destructive and non-invasive technique that can be used to study a wide range of materials, including biological samples, polymers, semiconductors and metals. Unlike other surface analysis techniques, AFM can provide high-resolution topographical information about surfaces, with a lateral resolution on the order of

nanometres. AFM can also be used to measure other surface properties, such as adhesion, roughness and mechanical properties.

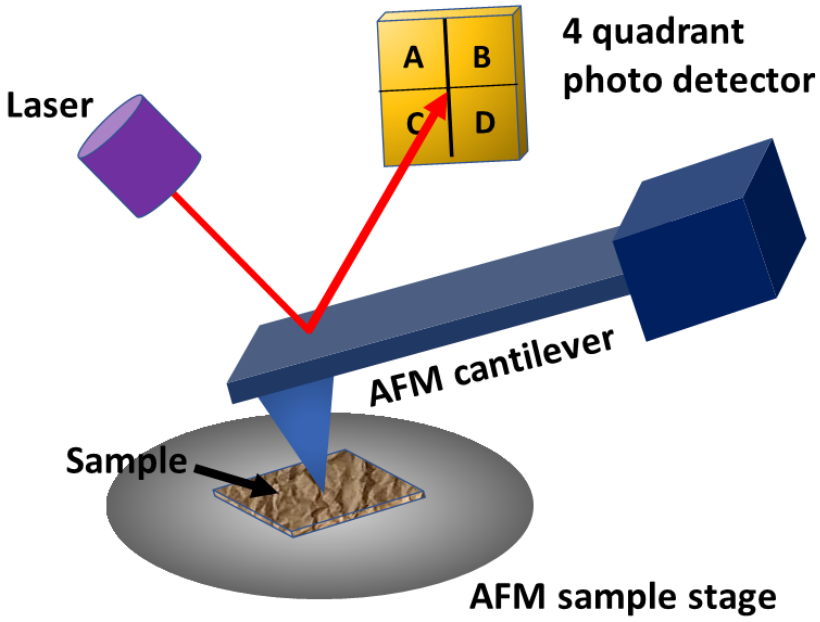

Figure 3.6 Schematic illustration of atomic force microscopy.

AFM data in this dissertation are taken using Bruker's ScanAsyst and PeakForce Tapping AFM. [10] A schematic illustration of atomic force microscopy operation is shown in figure 3.6. AFM operates by scanning a sharp probe tip over the surface of the material of interest and measuring the deflection of a cantilever that holds the probe. The cantilever deflection is a measure of the force between the probe tip and the surface of the material and is used to reconstruct a topographic image of the surface.

The AFM probe tip is typically made of silicon or silicon nitride and has a radius of curvature of a few nanometres. The probe tip is brought into contact with the surface of the material and the cantilever deflection is measured using a laser beam that is reflected off the back of the cantilever onto a detector. The accuracy and quality of AFM measurements rely heavily on the detection system employed. One widely used detection method involves directing an optical beam towards the centre of a quadrant

photodiode (QPD). This type of position sensing detector operates in a straightforward manner, where a laser beam with a Gaussian spot is directed onto the centre of the detector. By combining the signals detected by each of the four quadrants (A, B, C, and D), it is possible to estimate the displacement of the laser spot in relation to the centre of the quadrant detector. The intensity variation associated with the detection is adjusted by normalising the sum intensity of all four quadrants (A+B+C+D) to account for potential fluctuations in laser beam intensity. As the probe tip is scanned across the surface of the material, the cantilever deflection changes due to the topography of the surface.

Electron microscopy techniques

Electron microscopy is a powerful set of techniques for imaging and analysing materials at the nanoscale. Two of the most commonly used electron microscopy techniques are scanning electron microscopy (SEM) and transmission electron microscopy (TEM).

3.4.3 Scanning Electron Microscopy (SEM)

SEM is a widely used imaging technique that produces high-resolution images of the surface of materials. In SEM, a focused beam of electrons is scanned across the surface of a sample and the electrons that are scattered or emitted from the surface are collected to form an image. SEM can provide information about the topography, morphology and elemental composition of a material. [11]

In SEM, a primary beam of electrons with energies ranging from a few keV to a few tens of keV is focused onto the sample surface. The high-energy primary electrons collide with the atoms in the sample, causing the emission of secondary electrons from

the sample's surface. These secondary electrons are collected by a detector to generate an image of the surface topography.

The SEM instrument consists of several components, including an electron source, a series of electromagnetic lenses, a sample holder, and a detector. The electron source generates a beam of electrons, which is focused and directed onto the sample surface using the lenses. The sample holder holds the sample in place and the detector collects the scattered or emitted electrons to produce an image. A schematic illustration of SEM along with the e-beam interaction with specimen is shown in figure 3.7.

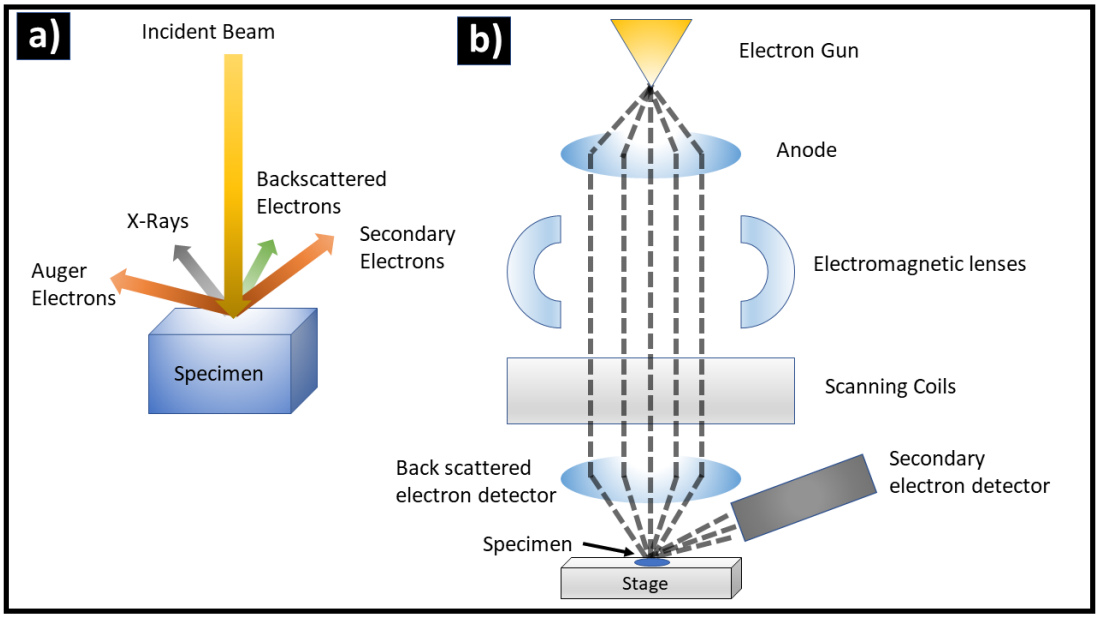

Figure 3.7 Schematic illustration of (a) electron beam interaction with specimen and (b) a scanning electron microscope (SEM).

3.4.4 Transmission electron microscopy (TEM)

TEM is a powerful imaging technique. A variety of TEM techniques such as including high-resolution TEM (HRTEM), scanning TEM (STEM), energy-dispersive X-ray spectroscopy (EDS), and high-angle annular dark field STEM (HAADF STEM) are

utilized in this thesis for inspecting various samples. For detailed information on TEM techniques refer to the book by David B. Williams and C. Barry Carter. [12]

(a) High-Resolution Transmission Electron Microscopy (HRTEM):

HRTEM is a powerful technique that provides detailed information about the crystal structure and defects in nanowires. The working principle of HRTEM is based on the interaction between a thin sample and a beam of high-energy electrons. As shown in the schematic in figure 3.8, a high-energy electron beam is focused onto a thin section of a specimen and the transmitted electrons are then detected by a sensitive detector. The resulting image provides information about the crystal structure of the specimen at an atomic scale.

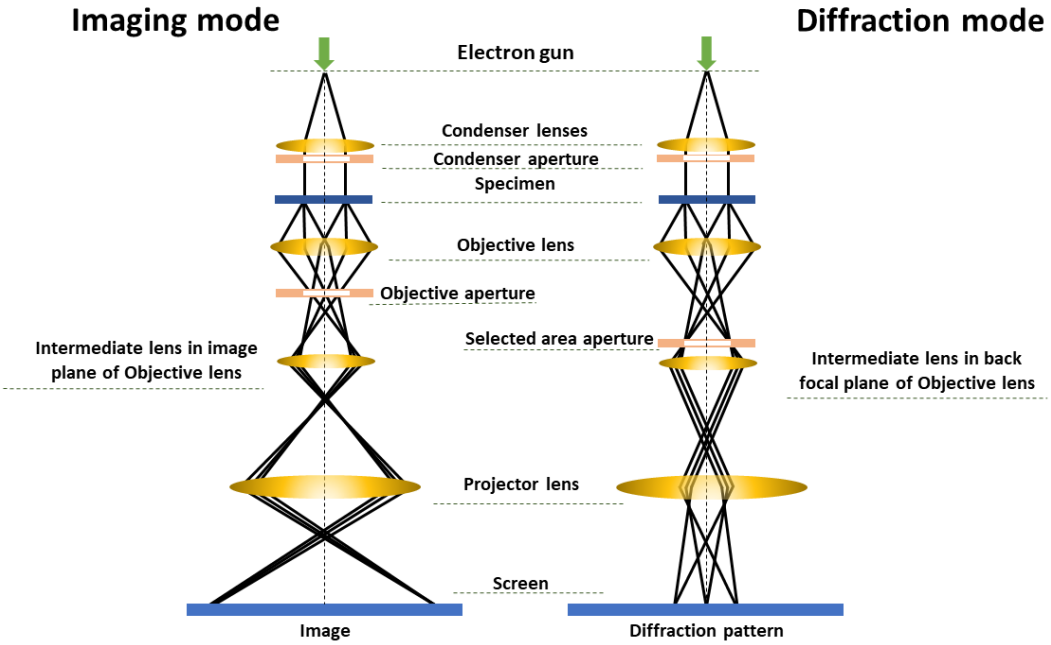

Figure 3.8 Schematic illustration of imaging and diffraction modes of transmission electron microscopy.

The electron beam in a TEM column is generated by an electron source, which can be a tungsten filament or a lanthanum hexaboride (LaB6) crystal. The electron beam is then passed a series of electromagnetic lenses.

The electron beam passes through a thin sample, which is mounted on a small grid or thin film. As the beam passes through the sample, it interacts with the atoms and electrons in the material, causing some of the electrons to scatter in different directions.

The scattered electrons are then collected by a series of electromagnetic lenses and detectors. These detectors can be positioned at different angles and distances from the sample to collect different types of scattered electrons.

The transmitted electrons, which have not interacted with the sample, are also collected by a detector placed on the opposite side of the sample. This detector measures the intensity of the transmitted electrons, which is used to create the bright-field image in a TEM.

The electron beam column in a TEM has several key components, including the electron source, the condenser lens, the objective lens, and the projection lens. The condenser lens focuses the electron beam onto the sample, while the objective lens collects the transmitted and scattered electrons to form the image.

The projection lens is used to magnify the image and project it onto a screen or camera. The magnification of the image is controlled by adjusting the focus of the objective lens and the position of the projection lens.

One of the limitations of HRTEM is that it requires a thin sample to be prepared, typically less than 100 nm in thickness. This can be challenging for some materials, especially those that are prone to damage from the ion beam used for sample preparation. HRTEM also requires high vacuum conditions, which can limit the types of samples that can be studied.

The two common modes of TEM imaging are imaging and diffraction as given in figure 3.8. In imaging mode, the electron beam is focused onto the specimen, and the

transmitted electrons are collected by a detector to form a two-dimensional image. The image resolution can be improved by using higher-energy electrons or reducing the distance between the sample and the detector. In diffraction mode, the electron beam is diffracted by the sample, producing a diffraction pattern that provides information about the sample's crystal structure and lattice spacing. By analysing the diffraction pattern, it is possible to determine the crystal structure, orientation, and composition of the sample.

(b) Scanning Transmission Electron Microscopy (STEM)

STEM is another technique that can be used to study thin specimens at high resolution. In STEM, a highly focused electron beam is scanned across the surface of the specimen, and the transmitted electrons are then detected by a detector. STEM provides high-resolution images of the surface of the specimen and can also be used to perform elemental analysis.

The working principle of STEM is like HRTEM, but STEM can provide higher contrast images due to the use of a high-angle annular dark-field (HAADF) detector, which collects scattered electrons at high angles. One limitation of STEM is that it is sensitive to sample thickness, and samples that are too thick may produce low contrast images.

(c) Energy-Dispersive X-ray Spectroscopy (EDS)

EDS is a technique that is used to determine the elemental composition of nanowires. In EDS, a high-energy electron beam is used to excite the atoms in the nanowire, causing them to emit characteristic X-rays. The emitted X-rays are then detected by a sensitive detector and the resulting spectrum is used to determine the elemental composition of the specimen.

One of the limitations of EDS is that it requires a high electron dose, which can cause radiation damage to the sample. EDS also has limited spatial resolution, typically on the order of a few nanometres.

(d) High-Angle Annular Dark-Field Scanning Transmission Electron Microscopy (HAADF-STEM)

HAADF-STEM is a type of STEM that uses a high-angle annular dark-field detector to collect scattered electrons at high angles. It provides high-resolution images of the thin specimen and can be used to perform elemental analysis. Figure 3.9 provides a simplified schematic of the HAADF-STEM system.

The working principle of HAADF-STEM is similar to STEM, but it provides higher contrast images due to the use of the HAADF detector. One limitation of HAADF-STEM is that it requires a high electron dose, which can cause radiation damage to the sample.

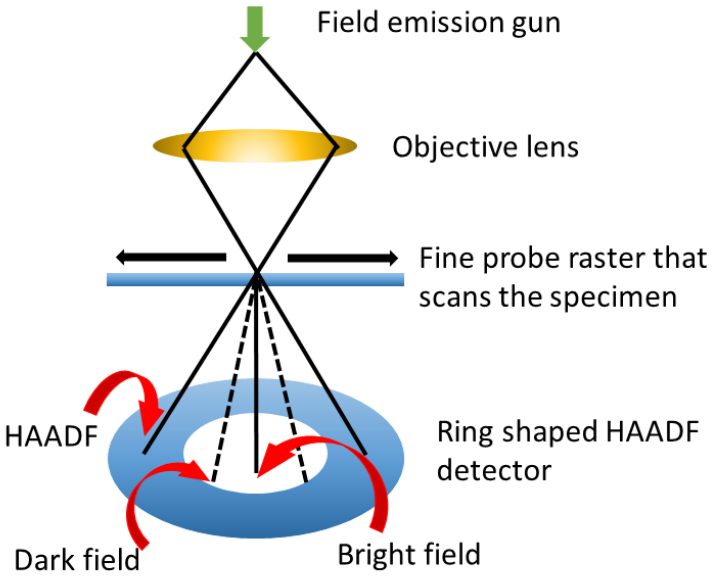

Figure 3.9 Schematic illustration of high-angle annular dark-field scanning transmission electron microscopy (HAADF-STEM).

3.4.5 Photoluminescence Spectroscopy

Photoluminescence (PL) spectroscopy is a non-destructive optical characterisation technique that measures the light emission from materials upon excitation by a light source. It is widely used for the characterisation of semiconductors, including III-V nanowires and thin films. PL provides information about the electronic and optical properties of the material, such as the bandgap, carrier concentration, recombination lifetime and defect density. [13] In III-V nanowires and thin-film samples, PL spectroscopy is a powerful tool for understanding the fundamental physics and for optimising the growth and processing conditions for device applications.

Time-Resolved Photoluminescence (TRPL)

TRPL is a powerful technique for studying the carrier dynamics of materials. It provides valuable information about the lifetime of excited states in a material, which is a key factor in determining the efficiency of optoelectronic devices. TRPL has a wide range of applications in materials science and optoelectronics. The PL spectra obtained for this thesis is acquired from the micro-PL system at the ANU. Figure 3.10 shows a schematic of the experimental set up at the ANU. The infra-red PL spectra are acquired from the PL system at UCLA.

TRPL typically involves a pulsed laser as the excitation source, a monochromator to select the excitation wavelength and a detector to measure the PL emission. The laser is pulsed with a duration typically in the picosecond to femtosecond range. The PL emission is collected using collection optics and directed to the detector, which is typically a photomultiplier tube or a CCD camera. The time resolution of the measurement is determined by the duration of the laser pulse and the response time of the detector.

The data obtained from TRPL measurements is typically presented as a decay curve, which plots the intensity of the PL emission as a function of time after excitation. The decay curve can be fitted to an exponential function to extract the PL lifetime. The PL lifetime is related to the efficiency of radiative recombination and nonradiative recombination processes in the material. A longer PL lifetime indicates a higher efficiency of radiative recombination, which is desirable for optoelectronic applications.

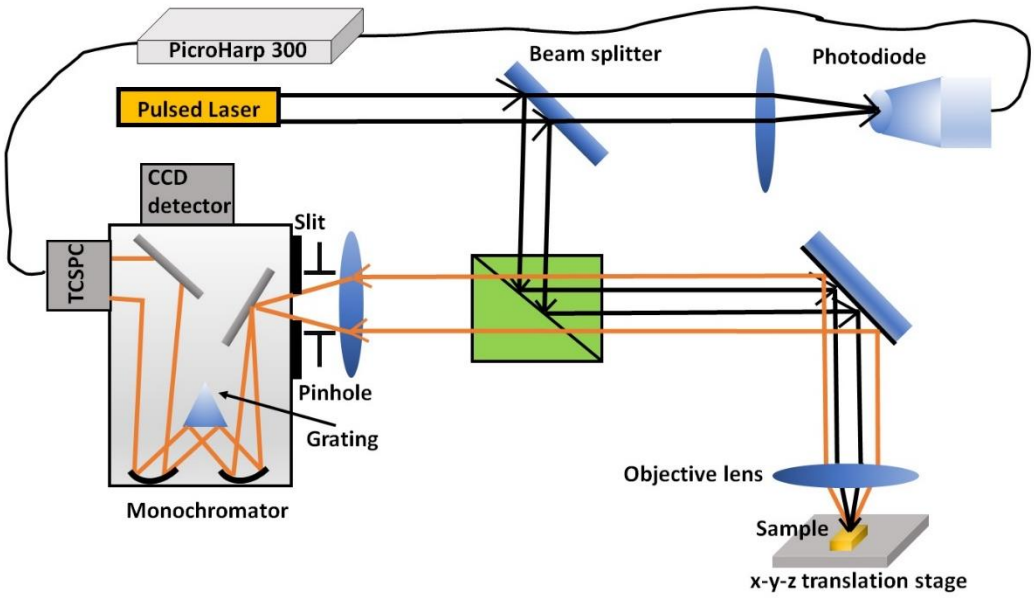

Figure 3.10 Schematic illustration of the room-temperature TRPL system.

3.4.6 X-Ray Diffraction (XRD)

Bragg's law is a fundamental principle of X-ray diffraction, which relates the angles at which X-rays are diffracted by a crystal lattice to the spacing between the crystal planes. The basic principle of X-ray diffraction is that when a beam of X-rays is incident on a crystal, the X-rays are scattered in different directions by the atoms in the crystal lattice. The scattered X-rays interfere constructively or destructively depending on the angle of incidence and the spacing between the crystal planes.

The law can be expressed mathematically as:

$$n\lambda = 2d \sin \theta$$

where:

n is the order of the diffraction peak

λ is the wavelength of the incident X-rays

d is the spacing between the crystal planes

θ is the angle between the incident X-ray beam and the crystal plane.

The law states that if the path difference between the X-rays scattered from two adjacent crystal planes is an integer multiple of the X-ray wavelength, then the diffracted waves will interfere constructively and a diffraction peak will be observed. This is known as constructive interference.

The angle at which the diffraction peak is observed depends on the spacing between the crystal planes and the wavelength of the X-rays. The higher the order of the diffraction peak, the smaller the angle of incidence required to produce it. This is because the path difference between adjacent crystal planes increases with increasing order of the diffraction peak.

Bragg's law is widely used in X-ray diffraction experiments to determine the crystal structure of materials. By measuring the angles at which X-rays are diffracted by a crystal, and by knowing the wavelength of the X-rays, the spacing between the crystal planes can be calculated. This information can then be used to determine the positions of the atoms in the crystal lattice and the crystal symmetry. Figure 3.11 gives a schematic of the Bragg’s law.

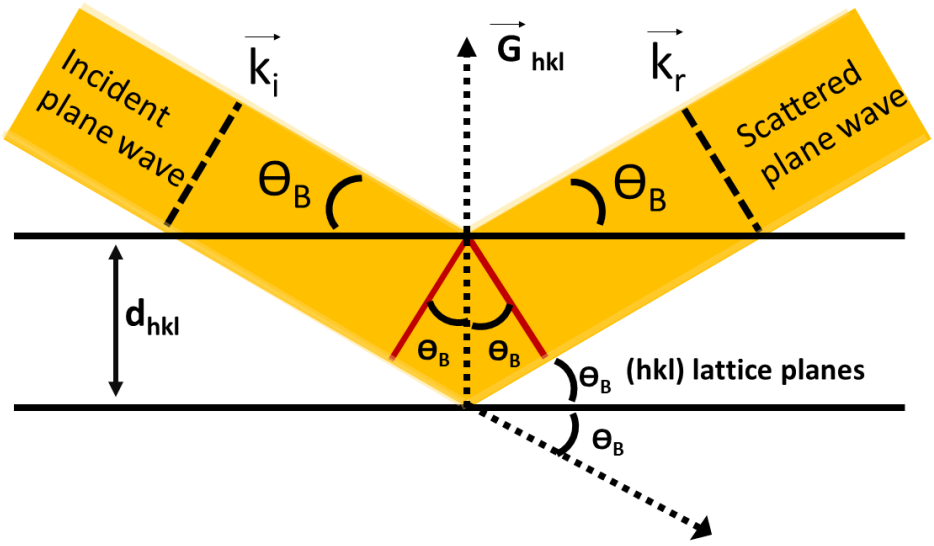

Figure 3.11 Illustration of the Bragg's law in an XRD set-up.

The XRD technique works by directing a beam of monochromatic X-rays at a crystalline sample which is mounted on a goniometer. The goniometer rotates the sample while the X-rays are diffracted in different directions. The diffracted X-rays are collected by a detector, such as a scintillation counter or a photographic film, and the intensity of the diffracted X-rays at different angles is measured. This produces a diffraction pattern, which is a graph of the intensity of diffracted X-rays as a function of the diffraction angle.

The diffraction pattern contains a series of peaks, which correspond to the diffraction angles of the diffracted X-rays. The positions and intensities of these peaks are related to the crystal structure of the sample. The positions of the peaks are determined by the spacing of the crystal lattice planes, while the intensities of the peaks depend on the arrangement of the atoms in the crystal.

XRD modes to study different aspects of a crystalline material's structure in this thesis are outlined below.

(a) High-resolution X-ray diffraction (HRXRD): HRXRD is a mode of XRD that is used to study the epitaxial quality of thin films and multilayer structures. In this technique, a high-resolution X-ray beam is directed at the sample, and the diffracted X-rays are collected at a high angular resolution. This allows for the precise determination of lattice parameters and crystallographic orientation of thin films and multilayer structures. The technique is particularly useful for the characterisation of semiconductor devices, such as transistors and solar cells, where the epitaxial quality of thin films is critical for their performance.

(b) Grazing incidence X-ray diffraction (GIXRD): GIXRD is a mode of XRD that is used to study the surface structure of thin films and interfaces. In this technique, the X-ray beam is incident at a grazing angle (typically less than 1^{o}) to the surface of the sample, which allows the X-rays to penetrate only a few atomic layers into the surface. This results in a diffraction pattern that is dominated by the surface structure of the sample. GIXRD is commonly used to study the crystal structure of thin films and interfaces, such as those found in semiconductor devices and catalytic materials.

(c) Rocking curve technique in XRD: The rocking curve technique is a mode of XRD that is used to study the structural quality of single crystals. The rocking curve technique is particularly useful for the characterisation of semiconductor materials, where the presence of defects can have a significant impact on their electrical and optical properties. It is based on the principle that the diffraction intensity of a single crystal varies with the angle of incidence of the X-ray beam, due to the crystal's crystallographic structure and defects.

In the rocking curve technique, a single crystal is mounted on a goniometer and rotated while the X-ray beam is directed at it. The diffraction intensity is measured as a function of the rotation angle, producing a rocking curve. The width and shape of the rocking curve provide information about the structural quality of the crystal, including the presence of defects such as dislocations, stacking faults, and twinning.

A high-quality single crystal will produce a narrow, symmetric rocking curve with a sharp peak, indicating a well-defined crystal structure with few defects. In contrast, a defective crystal will produce a broad, asymmetric rocking curve with a lower intensity peak, indicating a distorted crystal structure with a high density of defects.

3.4.7 X-Ray and Ultraviolet Photoelectron Spectroscopy (XPS and UPS)

XPS and UPS are both widely used analytical techniques that provide valuable information about the electronic structure and composition of materials.

XPS is a surface-sensitive technique that measures the binding energy of electrons emitted from the surface of a material when it is exposed to X-rays with energies ranging from 0.1 to 2 keV where as the UPS uses an ultraviolet light source. The binding energy is related to the electronic structure and chemical environment of the material. The XPS instrument includes an X-ray source, a sample holder, an electron analyser and a detector. The X-ray source emits X-rays onto the sample, which causes photoelectrons to be emitted from the surface of the material. The electron analyser selects electrons with specific energies and angles of emission, and the detector measures the intensity of the emitted photoelectrons as a function of energy. Figure 3.12 shows the energy level diagram for a sample and spectrometer during an XPS experiment.

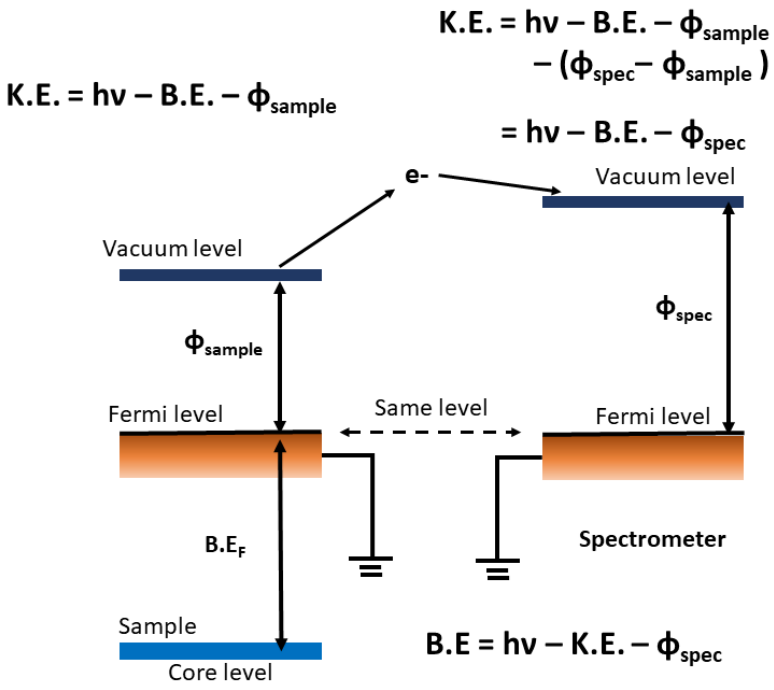

Figure 3.12 Energy level diagram for a sample and spectrometer during an XPS experiment.

UPS, on the other hand, measures the kinetic energy and intensity of photoelectrons emitted from the valence band of a material when it is exposed to ultraviolet light with energies ranging from 6 to 50 eV. UPS is also a surface-sensitive technique that provides information about the electronic structure and chemical environment of a material.

UPS is commonly used to study the electronic structure of organic molecules, polymers and other materials with low atomic number elements. It is also used to study the band alignment at interfaces between different materials. UPS can determine the work function and ionisation potential of materials, which is important for the design of electronic devices.

A flood gun is a commonly used tool for the analysis of insulating or dielectric materials. When an insulating sample is irradiated with ultraviolet light, the

photoelectrons that are emitted from the surface may be trapped in the sample's bulk or surface charges, leading to a charge-up effect that can affect the results of the analysis. This effect can be mitigated by using a flood gun, which provides a low-energy electron beam that neutralizes the charge on the sample's surface.

The flood gun emits electrons with energies ranging from a few eV to a few hundred eV, which are much lower than the kinetic energy of the photoelectrons emitted from the sample surface. The low-energy electrons from the flood gun collide with the surface of the sample, neutralizing the positive charge that accumulates due to the emission of photoelectrons. This enables the analysis of the sample's surface without any distortions due to charge effects.

The flood gun is typically located at a small angle to the sample surface, so that the emitted electrons do not interfere with the analysis of the photoelectrons. The angle and energy of the flood gun electrons can be adjusted to optimize the neutralization of the sample's surface charge while minimizing any additional noise or background signal.

3.4.8 Hall effect measurement

Hall effect is a phenomenon that describes the generation of an electric field perpendicular to the direction of an electric current flowing in a conductor. This effect was first discovered by American physicist Edwin Hall in 1879. When a magnetic field is applied to a conductor carrying an electric current, the Lorentz force causes a transverse voltage, known as the Hall voltage, to appear across the conductor. The Hall voltage is proportional to the magnetic field strength and the current density, and inversely proportional to the number of charge carriers in the conductor. Therefore, the Hall effect can be used to determine the concentration and mobility of charge carriers in a material, as well as its magnetic field strength.

The Hall effect measurement is a commonly used technique to determine the resistivity and carrier concentration of a semiconductor material. Using the four-probe Van der Pauw method measurement that can be used to determine the electrical properties of a sample regardless of its shape or size.

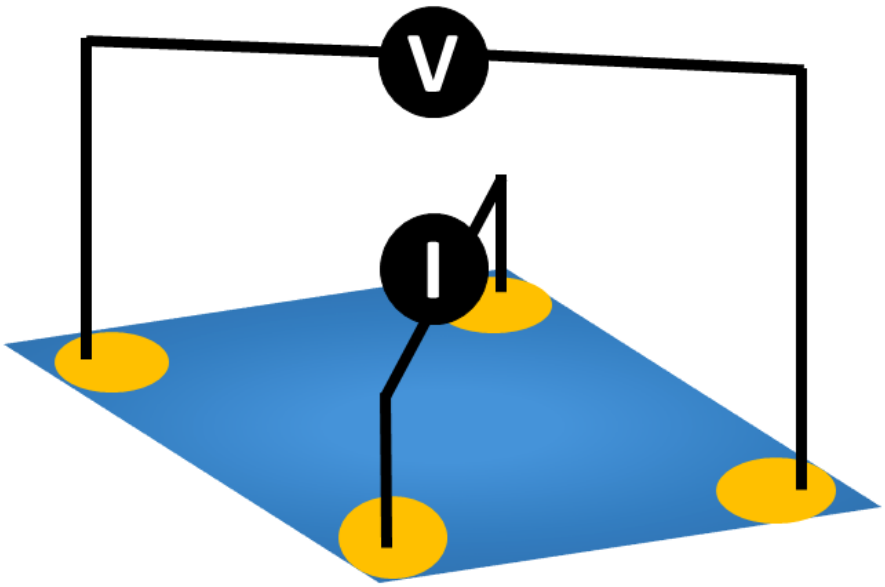

Figure 3.13 Schematic illustration of the sample configuration for the van der Pauw method hall measurement.

The Hall measurement is based on the relationship between the electrical resistivity and the Hall coefficient of a material. The Hall effect occurs when a magnetic field is applied perpendicular to the direction of current flow in a conductor. This results in a transverse voltage that is proportional to the applied magnetic field and the carrier concentration of the material. The Hall coefficient is defined as the ratio of the transverse voltage to the applied magnetic field and the current density. The schematic in Figure 2.12 illustrates the measurement geometry. The resistivity of the material can be determined by measuring the voltage drop across the sample when a current is passed through it. However, this method cannot be used for non-uniform or irregularly shaped

samples. The Van der Pauw method overcomes this limitation by using a four-probe measurement. In this method, four contacts are placed on the sample in a non-collinear configuration. The resistivity and Hall coefficient of the material can be determined by measuring the resistance between the two pairs of opposing contacts as the current is passed through the sample.

3.5 References

(1) Stringfellow, G. B. *Organometallic Vapor-Phase Epitaxy*, second edi.; Elsevier, 1999. https://doi.org/10.1016/B978-0-12-673842-1.X5000-5.

(2) Hannah Jane Joyce. Growth and Characterisation of III-V Semiconductor Nanowires for Optoelectronic Device Applications. **2009**, No. December.

(3) Bashir, A.; Awan, T. I.; Tehseen, A.; Tahir, M. B.; Ijaz, M. *Interfaces and Surfaces*; 2020. https://doi.org/10.1016/B978-0-12-818908-5.00003-2.

(4) George, S. M. Atomic Layer Deposition: An Overview. *Chem. Rev.* **2010**, *110* (1), 111–131. https://doi.org/10.1021/cr900056b.

(5) Johnson, R. W.; Hultqvist, A.; Bent, S. F. A Brief Review of Atomic Layer Deposition: From Fundamentals to Applications. *Mater. Today* **2014**, *17* (5), 236–246. https://doi.org/10.1016/j.mattod.2014.04.026.

(6) Oviroh, P. O.; Akbarzadeh, R.; Pan, D.; Coetzee, R. A. M.; Jen, T. C. New Development of Atomic Layer Deposition: Processes, Methods and Applications. *Sci. Technol. Adv. Mater.* **2019**, *20* (1), 465–496. https://doi.org/10.1080/14686996.2019.1599694.

(7) Wagner, R. S.; Ellis, W. C. Vapor-Liquid-Solid Mechanism of Single Crystal Growth.

Appl. Phys. Lett. **1964**, *4* (5), 89–90. https://doi.org/10.1063/1.1753975.

(8) Morsin, M.; Nafisah, S.; Sanudin, R.; Razali, N. L.; Mahmud, F.; Soon, C. F. The Role of Positively Charge Poly-L-Lysine in the Formation of High Yield Gold Nanoplates on the Surface for Plasmonic Sensing Application. *PLoS One* **2021**, *16* (11 November), 1–15. https://doi.org/10.1371/journal.pone.0259730.

(9) Raman, C. V. A New Radiation *. 1928, *2* (March), 387–398.

(10) Bruker. Application Note # 133 Introduction to Bruker ' s ScanAsyst and PeakForce Tapping AFM Technology. *Bruker Application Note*. 2011, pp 1–12.

(11) Mayeen, A.; Shaji, L. K.; Nair, A. K.; Kalarikkal, N. Morphological Characterisation of Nanomaterials. In *Characterisation of Nanomaterials*; Elsevier, 2018; pp 335–364. https://doi.org/10.1016/B978-0-08-101973-3.00012-2.

(12) David B. Williams, C. B. C. *Transmission Electron Microscopy*; 2009. https://doi.org/https://doi.org/10.1007/978-0-387-76501-3.

(13) Metzger, W.; Ahrenkiel, R.; Dippo, P. Time-Resolved Photoluminescence and Photovoltaics. *Dep. Energy Sol. Energy Technol. Progr. Rev. Meet.* **2004**, *1* (January), 1–2.

Chapter 4

Epitaxial Growth of GaAs Nanowires on Synthetic Mica by Metal−Organic Chemical Vapour Deposition

4.1 Introduction

van der Waals epitaxy is an unconventional technique that addresses the challenges of lattice and thermal expansion coefficient mismatch between substrate materials and epitaxial layers.[1] Although there are various research efforts to grow 2D and 3D materials on 2D substrates, only a few reports exist on the growth of II-VI and III-V epitaxial layers and nanostructures on 2D templates.[2–4] The exceptional electronic and optoelectronic properties of III-V semiconductor NWs, coupled with the weak bonding between NWs and 2D substrates, provide an excellent opportunity to design structures that can be easily detached for flexible device applications.

In general, GaAs NWs tend to nucleate in either the cubic ZB or hexagonal WZ crystal phase and grow preferentially in the [111] B direction on substrates such as GaAs and Si due to energetic reasons. Joyce et al. proposed a model for the growth of Au-seeded GaAs NWs on GaAs substrates that accounts for the effect of temperature and V/III ratio on crystal structure. [5]

This chapter provides a comprehensive growth study of GaAs NWs with a focus on achieving maximum vertical yield and good optical quality, specifically for the pure ZB phase NWs. Additionally, the study investigates the potential for peeling off the NWs from the synthetic mica substrate for flexible device applications.

Section 4.2 provides the details of substrate material and methods used in the study. The research on MOCVD growth parameters for epitaxial growth of GaAs NWs on synthetic mica is outlined in section 4.3. The research begins by exploring the effect of AsH_3 pre-flow on NW growth, as detailed in sub-section 4.3.1. This pre-flow is crucial in altering the surface energy of the mica surface and the results demonstrate that even a pre-flow duration as low as 1 minute can enhance the NW vertical yield. Sub-sections 4.3.2 and 4.3.3 then discuss the effect of basic growth parameters on the vertical yield of the NWs.

Section 4.4 delves into the optical properties of AlGaAs passivated GaAs NWs on synthetic mica and showcases the successful peel-off of a large array of NWs. The crystal structure of NWs synthesised using various growth parameters is discussed in detail in section 4.5, with subsections 4.5.1 and 4.5.2 describing the effect of temperature and V/III ratio, respectively.

In section 4.6, the crystal polarity is discussed and compared with typical NW polarities from literature. Section 4.7 then describes the computational methodology used to study the GaAs-mica interface, followed by detailed theoretical analysis based on electronic structure properties in section 4.7.1.

The chapter concludes with section 4.8, which summarises the growth, morphology, passivation and optical properties of NWs, along with the structural and theoretical results of GaAs NWs grown on synthetic mica.

4.2 Materials and methods

4.2.1 Choice of substrate

The identification of stable 2D materials that can withstand high growth temperatures and hydrogen ambience is crucial for vapour-liquid-solid (VLS) growth of GaAs NWs. Graphene/graphitic substrates and mica have been identified as suitable materials for this

purpose. Although III-V NWs can be grown easily on almost any substrate using gold-seeded VLS, achieving vertical NWs can be challenging. This is because without proper control of the contact angle of the gold nanoparticles, most NWs tend to be non-vertical or kinked. To obtain vertical NWs, a medium to large contact angle on the chosen substrate material is required. Previous attempts to grow very high-yield vertical GaAs NWs on graphene using VLS epitaxy have been unsuccessful. [6]

The surface energy of mica is an order of magnitude less than that of conventional V/III substrates, but relatively high compared to graphene. Table 4.1 gives the surface energy comparison between conventional substrates and several van der Waals substrates.[7–10] Although the surface energy of mica is not as high as typical semiconductors, it is an order of magnitude higher than the graphitic substrates, this attribute is hypothesised to promote more out-of-plane NW growth. However, the lack of dangling bonds on the mica surface due to its van der Waals nature does not readily support epitaxial growth. Surface treatments and precursor pre-flow can be used to modify the surface energy and promote growth.[11] The contact angle formed on the surface of mica is a result of the surface energy balance between the gold nanoparticle and the substrate at a given growth temperature.

Conventional substrates	Surface energy (γ_{sv}) Jm^{-2}
GaAs (111)B	1.07
Si (111)	1.24
van der Waals substrates	**Surface energy (γ_{sv}) Jm^{-2}**
Mica	0.38
Graphene	0.029
MoS_2	0.07-0.075

Table 4.1 Comparison of the surface energies between conventional and several van der Waals substrates.

4.2.2 Synthetic mica

The synthetic mica used in this study is fluoro-phlogopite, which belongs to the biotite group of phyllosilicate materials and is rich in magnesium. Synthetic mica exhibits desirable physical properties such as high transparency, flexibility, chemical inertness and an atomically smooth surface. [12] Additionally, its thermal stability above 1000 °C makes it suitable for epitaxial growth experiments using MOCVD. The synthetic mica measuring 20 mm x 20 mm from Continental Trade are used for the growth of the NWs.

Synthetic mica, like other types of mica, is a layered monocrystalline material with a monoclinic crystal structure possessing a space group symmetry of C2/m. The lattice parameters of synthetic mica are a = 5.308Å, b = 9.183Å, c = 10.139Å, ß = 100.07º, and Z=2.[13] The crystal structure of mica consists of trioctahedral sheets (all octahedral sites filled) containing Mg and F sandwiched between silicate sheets, held together by KO_6 octahedra as shown in Figure 4.1 (a) and (b). Crystal Maker 2.7 software is utilised to simulate the crystal structure of synthetic mica and to calculate the angles between crystal

planes, bond lengths and density. Figure 4.1 (c) shows the HR-XRD peaks depicting the single crystalline nature of the synthetic mica.

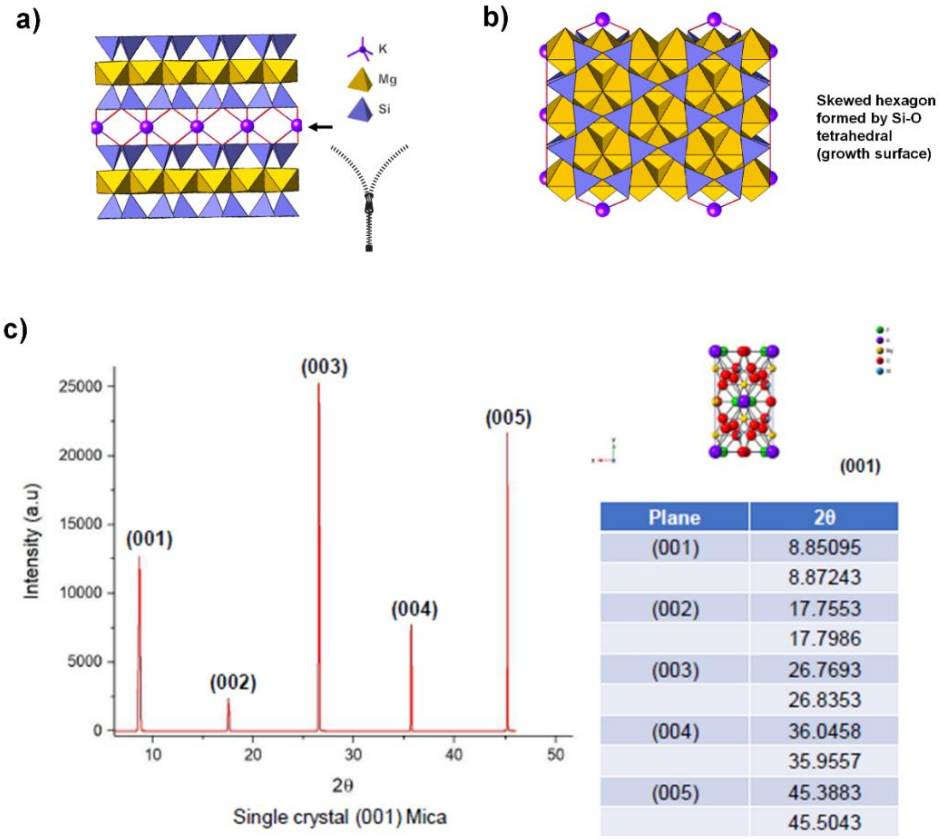

Fig 4.1 (a) and (b) depict the layered structure of mica with the interlayer cation potassium (K) and the skewed hexagon formed by Si-O tetrahedral arrangement. (c) HR-XRD peaks showing the (001) family of planes with the 2Theta angles of various planes and a corresponding ball-and-stick model of the crystal structure.

Synthetic mica possesses various unique properties that make it useful in many applications. One of the most notable properties of synthetic mica is its thermal stability, which allows it to withstand high temperatures in excess of 1000 ºC. This makes it ideal for use in epitaxial growth experiments using MOCVD. Additionally, synthetic mica has a high degree of transparency, allowing for the measurement of optical properties of as-

grown NWs without very low background contributions. Figure 4.2 (a) shows the AFM scan of a freshly cleaved mica surface showing an atomically smooth surface. Moreover, the absorption spectrum of synthetic mica shown in figure 4.2 (b) indicates a wide transmission range from UV to IR.

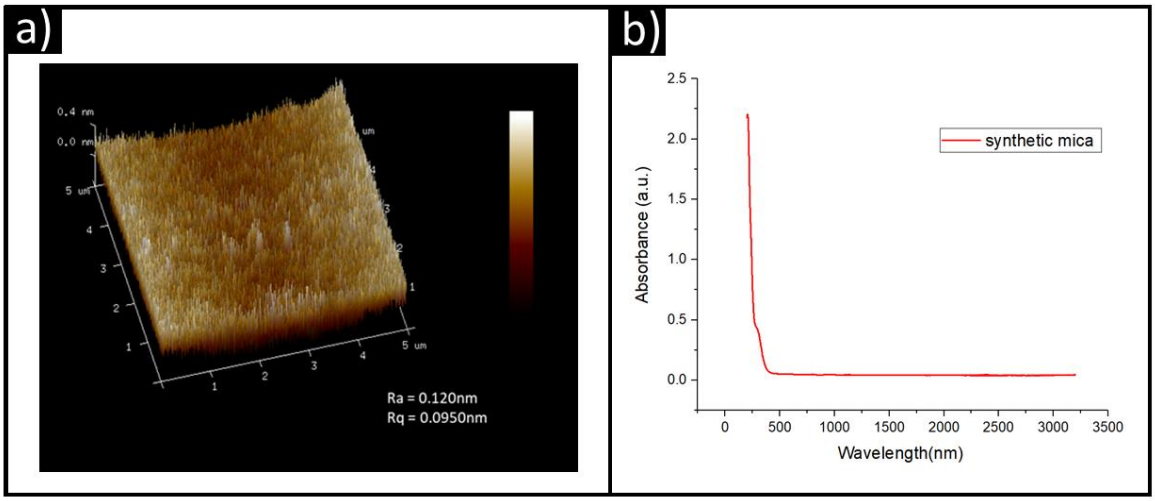

Figure 4.2 (a) AFM and (b) absorption spectrum of freshly cleaved synthetic mica.

Experimental Methods: Synthetic mica substrates were used for the growth of NWs. Gold nanoparticles were deposited on the substrate using poly-L-lysine (PLL) functionalisation. PLL is a positively charged polyelectrolyte that attracts the negatively charged Au nanoparticles and helps to immobilize them on the substrate. The deposition of gold nanoparticles was carried out in two steps, PLL functionalisation and gold nanoparticle deposition.

For the functionalisation step, the substrate was immersed in PLL solution for 60 seconds. After 60 seconds, the substrate was rinsed with DI water and blow-dried using N_2 gas gun.

Next, the gold nanoparticle deposition was carried out by dispersing the Au colloidal solution on the substrate for 60 seconds. After deposition, the substrate was rinsed with DI water and blow-dried using a N_2 gas gun.

4.3 MOCVD growth and characterisation

Experimental Methods:

The experiment involved growing GaAs NWs in an MOCVD reactor under varying conditions. To investigate the effects of growth temperature, V/III ratio and AsH_3 pre-flow, samples were transferred to the reactor with a reduced pressure of 100 mbar. The NWs were grown using a single-temperature growth step, whereby the reactor was heated to the desired temperature and AsH_3 was pre-flown for a fixed duration. TMGa was then introduced to initiate NW growth, which continued for 20 minutes. After growth, the reactor was allowed to cool under AsH_3 ambient until the temperature dropped below 350 ºC. The experiment investigated the effects of growth temperature (375-500 ºC) and V/III ratio (5.2-335) by varying the group V flow while keeping group III flow constant. AsH_3 pre-flow prior to growth was also varied at a fixed rate of 1.295×10^{-3} mol/min for 0, 1, 5, and 60 minutes. SEM and TEM were used for the morphological and structural characterisation of the NWs, respectively. SEM images were collected with an accelerating voltage of 3 kV to prevent charging of the mica substrate. Finally, the polarity of the NWs was determined using HAADF-STEM microscopy. All NWs were grown using 60 nm gold particles unless stated otherwise.

4.3.1 Effect of AsH_3 pre-flow

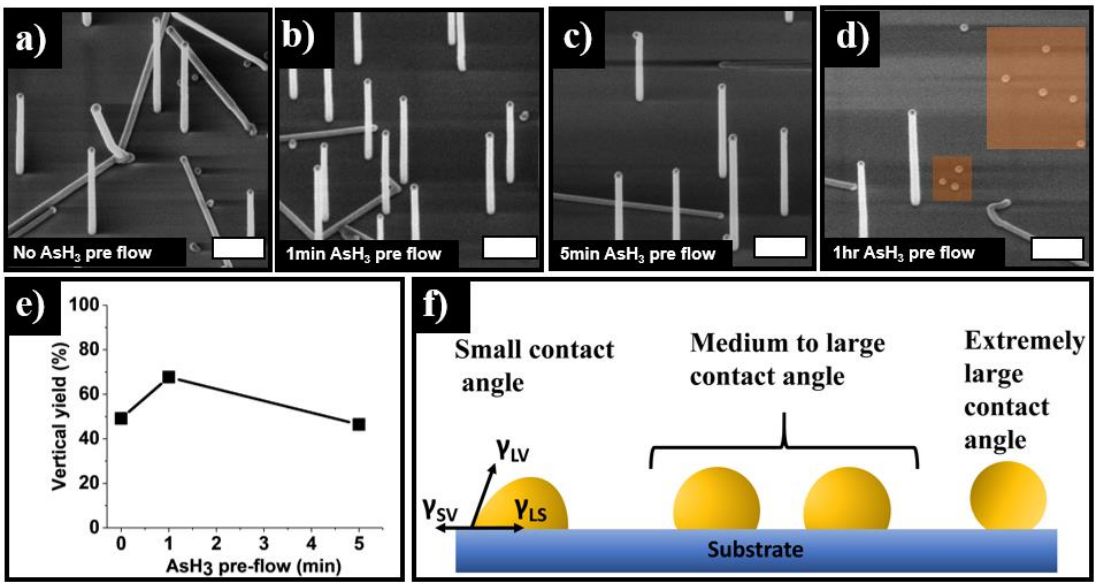

Figure 4.3. SEM images of GaAs NWs grown on synthetic mica with varying AsH_3 pre-flow time of a) no pre-flow, b) 1 min, c) 5 min and d) 1 hr. The false colored area in d) shows gold particle de-wetting. All scale bars are 500 nm. e) Vertical yield of NWs as a function of AsH_3 pre-flow. f) Schematic representation of gold on mica illustrating Au seed geometries on a substrate with small, medium to large and extremely large contact angles.

Figure 4.3 (a)-(d) presents 45º-tilted SEM images of GaAs NWs grown with different AsH_3 pre-flow times, with the corresponding percentage vertical yield summarised in Figure 4.3 (e). The percentage vertical yield refers to the ratio of vertical NWs to the total number of NWs. The NW count was conducted on SEM images taken from various regions of the as-grown sample, covering an area of 25 μm² each. Each data point in Figure 4.3 (e) represents an average count from 5 of these images. Results show that without AsH_3 pre-flow, a relatively high vertical yield of about 50% is achieved. However, pre-flowing AsH_3 for 1 min results in an additional 10% increase in the vertical

yield, whereas increasing the duration of AsH_3 pre-flow beyond 1 min leads to a dramatic drop in the vertical yield.

The growth direction and crystal phase of the NWs depend significantly on the contact angle between the gold nanoparticles and the substrate. The contact angle is determined by the surface energy balance between the gold nanoparticle and the substrate at the growth temperature. Studies have shown that manipulating the contact angle by altering the surface energy of the substrate can engineer the vertical yield, crystal phase and NW polarity.[11] A medium to large contact angle is preferred for vertical NW growth, whereas a low or extremely large contact angle results in in-plane/crawling NWs or no growth, respectively.

The surface energy of the growth substrate can be altered by surfactants or by passivation. In-situ TEM measurements of GaAs NW growth have demonstrated that the AsH_3 flow rate and hence V/III ratio, plays a significant role in the gold contact angle and crystal phase selection.[14] Furthermore, the possible surface energy changes to the mica/gold nanoparticle interface with AsH_3 pre-treatment can affect the yield of vertical NWs.

Our results indicate that pre-flowing AsH_3 prior to growth can manipulate the contact angle of the gold nanoparticles on mica, leading to changes in the vertical yield. Increasing the AsH_3 pre-flow time beyond 1 min results in a significant increase in the contact angle, leading to a drop in the vertical yield. Figure 4.3 (d) highlights the areas where the gold nanoparticles have an extremely large contact angle on the mica surface, inhibiting NW growth for long AsH_3 pre-flow times.

4.3.2 Effect of growth temperature

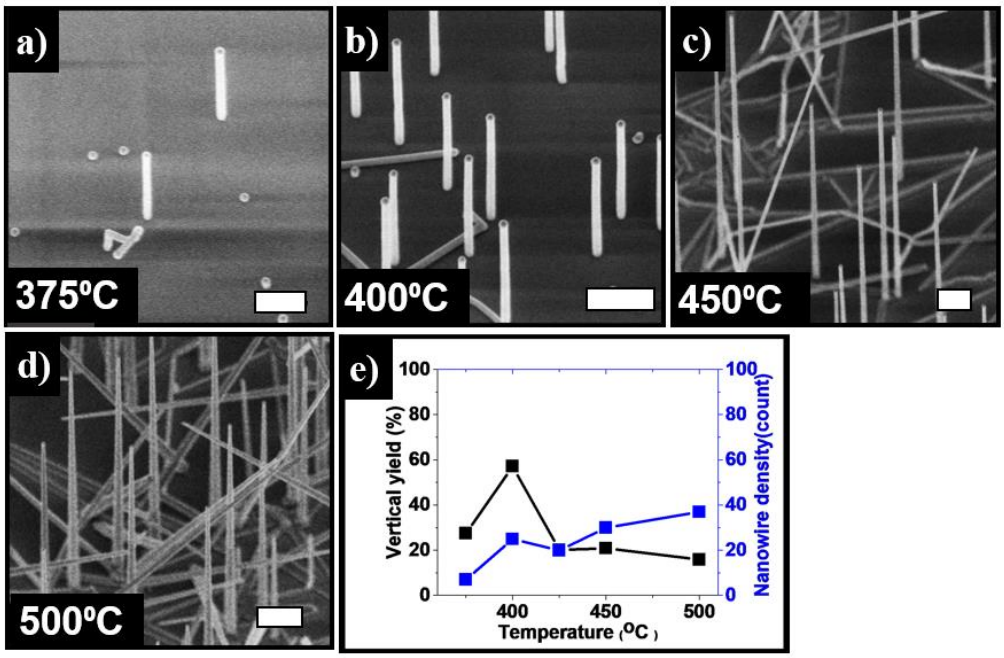

Figure 4.4. SEM images of GaAs NWs grown on synthetic mica at various temperatures. (a-d) 40º tilted view images of GaAs NWs grown at a temperature of 375 ºC, 400 ºC and 450 ºC and 500 ºC, respectively. All scale bars are 500 nm. e) Vertical NW yield (black) and NW density (blue) as a function of growth temperature.

SEM images of NWs grown with a fixed AsH_3 pre-flow time of 1 min at various temperatures ranging from 375-500 ºC are presented in Figure 4.4 (a)-(d). An increase in NW tapering is observed with increasing growth temperature. However, the vertical yield of the NWs does not follow a linear trend. The maximum vertical yield is observed at 400 ºC, as shown in Figure 4.4 (e). The NW count was conducted on SEM images taken from various regions of the as-grown sample, covering an area of 25 μm² each. Each data

point in Figure 4.4 (e) represents the average count from 5 of these images. The plot also shows the NW areal density, which counts the total number of nucleated NWs. At low growth temperatures, the decomposition efficiency of AsH_3 and TMGa is reduced, resulting in a low NW density. As the growth temperature is increased, more precursor decomposition occurs, resulting in an increase in the density of nucleated NWs. However, at high growth temperatures, tapering of the NWs is observed due to increased competition of radial growth with axial growth. At high temperatures, adatoms have sufficient energy to diffuse from the surrounding regions onto the NWs, resulting in radial growth. In addition, there is a significant increase in inclined and in-plane NWs, probably due to improved precursor decomposition at these temperatures.

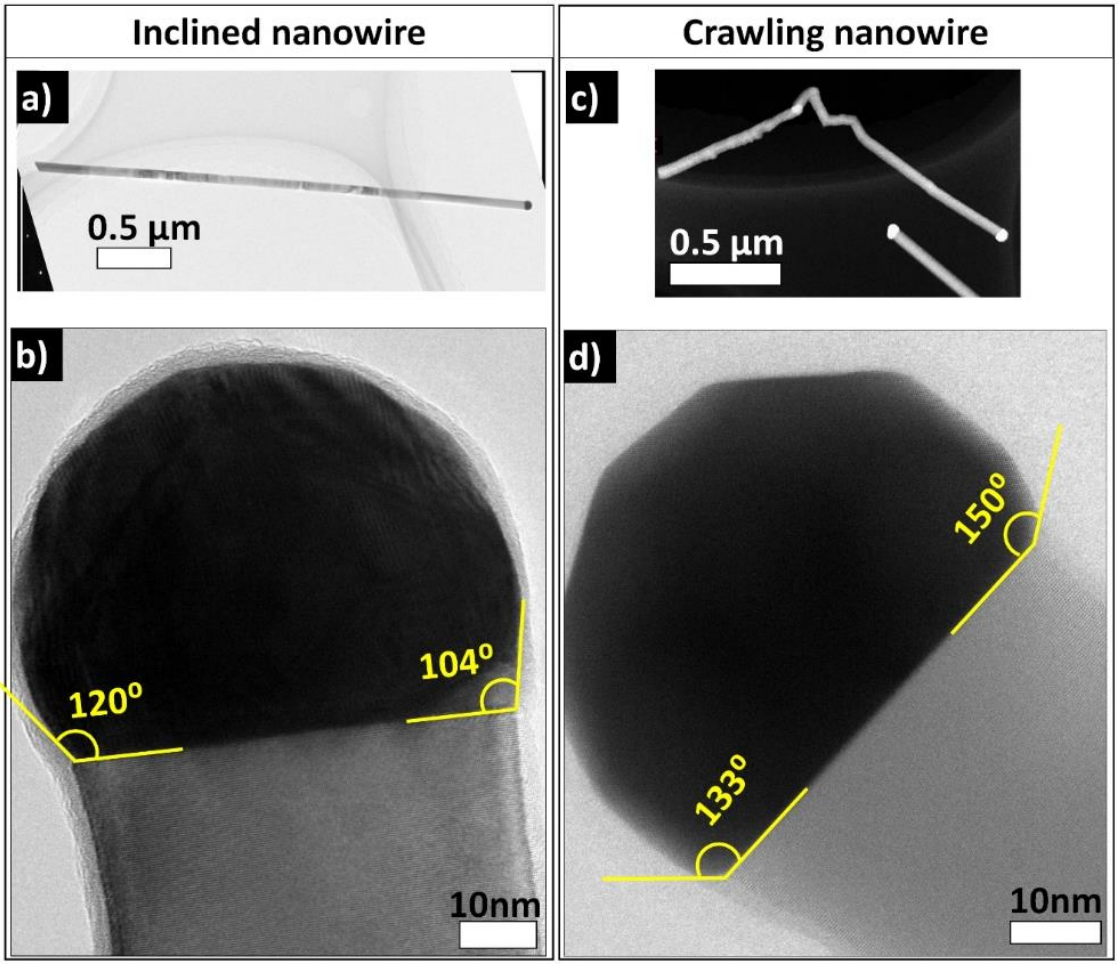

Figure 4.5 The full length of an inclined wire is shown in a), while b) shows the HRTEM

image of the NW top with the gold contact angles on either side of the inclined NW. The full length of a crawling NW is shown in c). The HRTEM image in d) shows the gold contact angles on either side of the crawling NW tip.

Figure 4.5 (a) and (b) shows the TEM image of an inclined NW and the HRTEM image of the tip of the NW respectively. The gold nanoparticle on inclined NW were noted to be 120º and 104º on either side after growth, and they are oriented in the [001] direction. Crawling NWs have larger contact angles, as shown in Figure 4.5 (c) and (d) shows the TEM images of a typical crawling NW with large contact angles of 133º and 150º.

4.3.3 Effect of V/III ratio

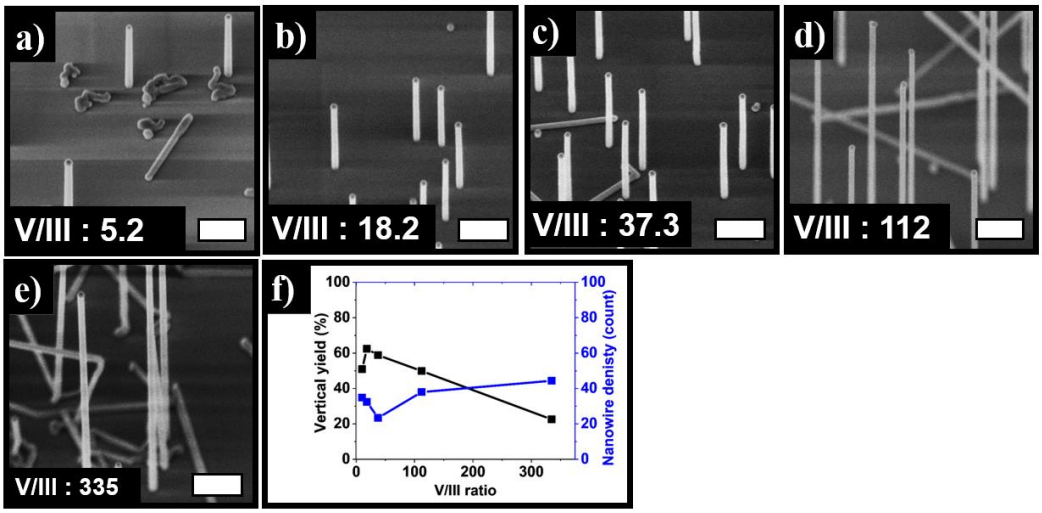

Figure 4.6. SEM images of GaAs NWs grown on synthetic mica under different growth conditions. (a-e) 40º tilted view images of GaAs NWs grown at 400 ºC growth temperature and V/III ratios of 5.2, 18.2, 37.3, 112 and 335, respectively. All scale bars are 500 nm. (f) Vertical NW yield (black) and NW density (blue) as a function of V/III ratio.

Figure 4.6 (a)-(e) displays SEM images of NWs grown at a temperature of 400 ºC and 1 min AsH_3 pre-flow with V/III ratios of 5.2, 18.2, 37.3, 112, and 335, respectively. However, the AsH_3 pre-flow rate used in this set of samples is the same as the flow rate used during growth for each V/III ratio, meaning that the higher V/III ratio samples have a higher AsH_3 pre-flow rate. Figure 4.6 (f) illustrates the trend in the vertical yield and the areal density of the NWs with respect to V/III ratio. The NW count was conducted on SEM images taken from various regions of the as-grown sample, covering an area of 25 μm^2 each. Each data point in Figure 4.6 (f) represents the average count from 5 of these images. The growth rate improves significantly from 5 nm/min at a V/III ratio of 5.2 to 200 nm/min at a V/III ratio of 112. A lower V/III ratio achieves a high vertical yield above 60%. Increasing the V/III ratio beyond the optimal value does not enhance the vertical yield but instead leads to crawling and inclined NWs. This finding agrees with the AsH_3 pre-flow study, where the vertical yield reduces considerably with AsH_3 pre-flow duration. A higher V/III ratio during growth results in an increased flow of AsH_3 in the pre-flow step, affecting the vertical yield in a way similar to the longer AsH_3 pre-flow study. At higher growth temperatures, the situation is quite comparable as more precursor decomposition occurs at higher growth temperatures for any given V/III ratio, leading to a high AsH_3 ambient.

The amount of AsH_3 in the environment increases with a higher V/III ratio and affects the surface energy of the mica. This interaction with the gold seed results in an increase in the number of vertical NWs, as seen in previous studies on AsH_3 pre-flow and temperature. However, an even higher V/III ratio leads to more kinked and tapered NWs, as shown in Figures 4.6 (d) and (e) for V/III ratios of 112 and 335, respectively.

The density of NWs, including crawling, inclined, and vertical NWs, increases with increasing V/III ratio due to the higher availability of group III and V precursor species

resulting from increased decomposition. However, SEM images show that higher V/III ratios also lead to more kinking and tapering of NWs. Tapering occurs because increasing group V adatoms reduce the diffusion length of group III adatoms, preventing them from reaching the Au tip. The observed kinking of axial NWs is attributed to the formation of stable As-trimers on As-terminated (111) B surfaces at high V/III ratios, which can hinder NW growth in the [111] B direction and encourage growth in other directions.[15] As a result of changes in the gold contact angle caused by temperature and V/III ratio, NWs do not only grow axially but also become inclined and kink from the axial growth direction.

4.4 Passivation and photoluminescence

To examine the optical quality of the GaAs NWs grown on mica, photoluminescence (PL) and time-resolved PL measurements were conducted on core-shell NWs at room temperature. The properties of GaAs Nanowires, such as carrier lifetime and mobility, have not yet reached the level of state-of-the-art planar GaAs devices.[16] This is due to the inherent large surface to volume ratio of nanowires, which leads to the formation of non-radiative recombination centres at the surface or interface. Specifically, nanowires suffer from lower carrier lifetime and high surface/interface recombination velocity, caused by non-radiative recombination pathways such as bulk defects and surface states.[17,18]

Additionally, the as-grown GaAs NW will form native oxide on the NW surface when in contact with ambient air, which in turn affects the optical properties. Therefore, to reduce non-radiative carrier recombination at the surface, it is well established that covering the GaAs surface with an AlGaAs layer is an effective method. This layer has a wider

bandgap and negligible lattice mismatch compared to GaAs, which reduces electronic surface states. N Jiang *et. al.* [19] have conducted research to optimize the growth of the AlGaAs shell on GaAs nanowires. They focused on the V/III ratio, shell growth temperature, and shell growth time to achieve the best results.

To create the core-shell NWs, an AlGaAs shell was deposited around the core of GaAs NWs grown on mica at 750°C, with a vapour phase ratio of TMGa/(TMAl+TMGa) = 0.3. The morphology of the core/shell NWs is shown in Figure 4.7(c). A typical PL emission around 1.43 eV, corresponding to the band edge transition within the GaAs core, is observed for the core/shell NWs, as shown in Figure 4.7(b). The inset shows the time-resolved PL decay measured at the band edge (1.43 eV), and the minority carrier lifetime (τ_{mc}) of 0.21 ns is calculated by fitting the data with a mono-exponential decay curve. The high-quality band edge PL emission at room temperature indicates that the NWs grown on synthetic mica exhibit a high optical quality.

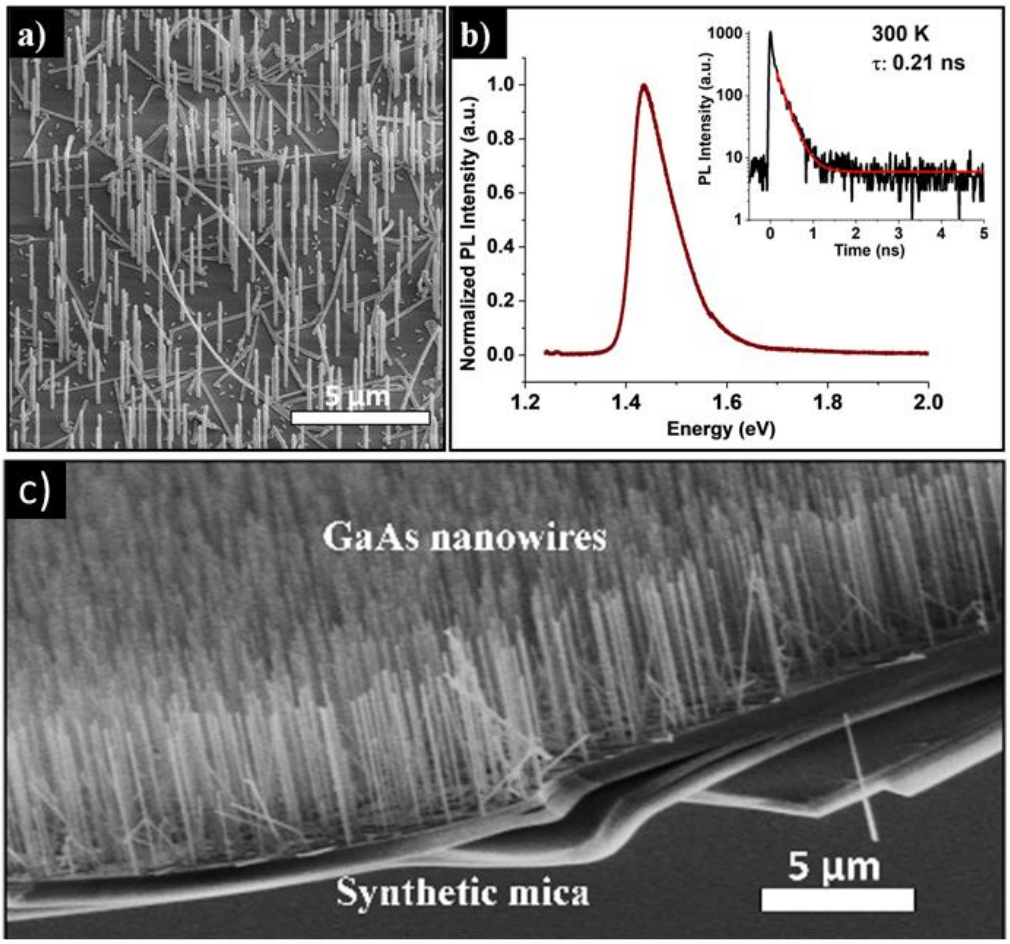

Figure 4.7 (a) SEM image showing the GaAs/AlGaAs/GaAs core/shell/cap NWs grown on synthetic mica. (b) A typical room temperature PL spectrum of a GaAs/AlGaAs/GaAs core/shell/cap nanostructure peeled off from the mica substrate. The inset shows the time-resolved PL decay with a mono-exponential curve fitting. The calculated minority carrier lifetime is 0.21 ns. (c) Cross-sectional SEM image of GaAs NWs on mica peeling off from the bulk mica substrate.

Moreover, the van der Waals layered structure of mica enables easy peel-off of large area vertical NWs mechanically using a scalpel, as depicted in Figure 4.7(c), and has two advantages: (i) it enables experiments to be designed to study the optical and mechanical properties of as-grown NWs and innovative design prospects for various flexible NW-based devices, and (ii) the substrate left after peel-off can be re-used for further epitaxial

growth, as a new atomically flat surface is exposed as a result of the peel-off, which further reduces the substrate cost involved. However, this is beyond the scope of this thesis and will be explored in future experiments.

4.5 Crystal structure of GaAs NWs

The NWs from the mica substrate were transferred to a copper grid by gently sliding the copper grid over the as-grown sample. The HRTEM images of the base of a NW show micro-faceting behaviour as shown in Figure 4.8 (a) and (b). We attribute this to the epitaxial alignment of GaAs with the mica substrate. It has been previously reported that NWs evolve through higher index facets to reach an equilibrium state when grown on substrates such as silicon.[20] All the vertical NWs grown under different conditions examined in this study have micro-faceting behaviour at their base.

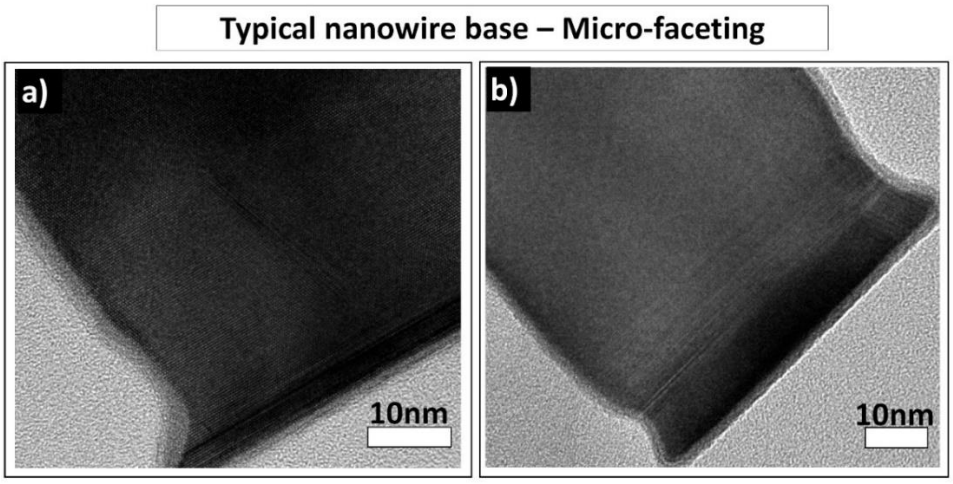

Figure 4.8 HRTEM images of a typical vertical NW are shown in (a) and (b), clearly showing the micro-faceting behaviour at the base of the NWs

4.5.1 Effect of growth temperature

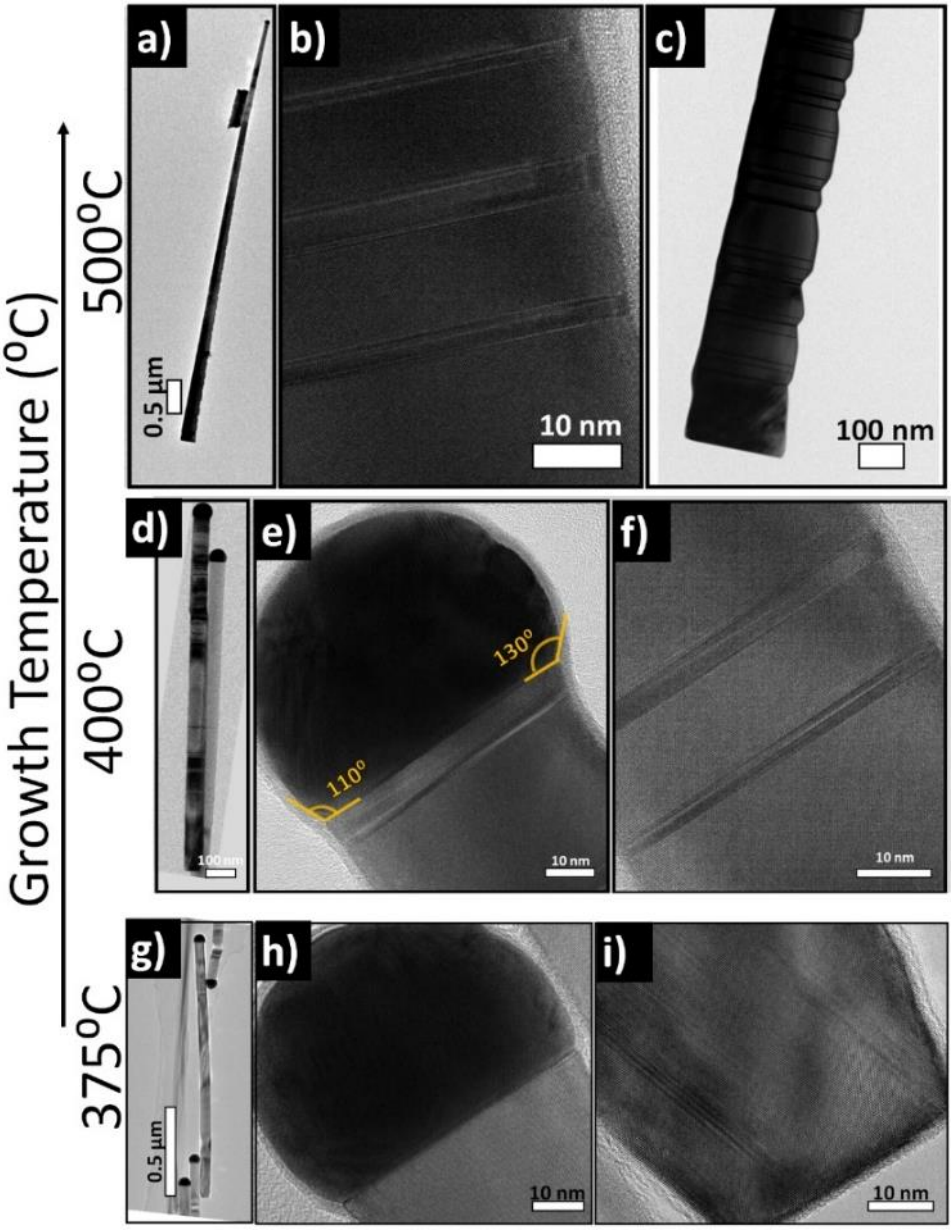

Figure 4.9 TEM images of NWs grown at various temperatures, at a constant V/III ratio of 37.3 and 1 min AsH_3 pre-flow. The full length of the NW, middle portion and base of NW grown at 500 °C are shown in a), b) and c), respectively. Defects (stacking faults) and tapering are clearly observed in b) and c). The full length of the NW, gold tip and middle of the NW grown at 400 °C are shown in d), e) and f), respectively, demonstrating the gold contact angle and stacking faults along the length of the NW. The full length of

the NW, gold tip and base of the NW grown at 375 ºC are shown in g), h) and i), respectively.

The crystal structure of NWs is heavily influenced by the growth temperature. In order to avoid high tapering and defect density in NWs, it is essential to use a lower growth temperature, as demonstrated by figures 4.9 (a), (d), and (g). Although high-temperature growth results in a higher growth rate, it comes at the cost of compromised crystal quality and a reduced number of vertical NWs.

Growth temperature plays an essential role in determining the crystal structure of NWs. As evident from figure 4.9 (a), (d) and (g), a lower growth temperature is essential to avoid high tapering (ratio of increase in NW radius per unit NW length) and high defect density in nanowires. Although the growth rate is high at high temperature, the crystal quality is compramised along with the number of vertical NWs as discussed earlier in section 4.3.2

Interestingly, Figure 4.9 (e) shows that the NW contact angle is asymmetric after growth, indicating that the gold seed moves constantly to maintain stability with the changing facets during growth. The initial evolution of the side facet and the inclined stacking fault [111] in some NWs at an angle of 70º to the growth plane suggest that the gold tip may be dragged to one side throughout the growth. Under As-rich conditions, either high temperature growth or high V/III conditions, the Au particles achieve contact angles greater than 110º. The gold-mica interfacial energy and its contact angle with the mica surface play an important role in determining the growth direction and potential kinking in the early stages of nucleation. Breuer et al [21] describe the effect of 'droplet-bulge' on the NW facets, where there is a decrease in lateral surface energy when the angle between the droplet and the facet is small. Additionally, it was found that the reduction in energy

is proportional to the droplet surface energy, resulting in different side facets for different droplets. For example, Au-seeded VLS growth typically has high surface energy (112) side facets, while Ga-seeded VLS has predominantly lower surface energy (110) side facets. The paper also suggests that the constituents of the generally observed (112) side facets are As-reconstructed (11-1) B facets.

4.5.2 Effect of V/III ratio

The NW morphology, growth direction, and crystal structure are significantly influenced by the V/III ratio. Figure 4.10 gives a comprehensive study on effect of V/III ratio on crystal structure of NWs. HRTEM investigations show that a high V/III ratio, achieved by increasing the AsH_3 flow rate, leads to less planar defects and promotes defect-free growth, particularly at a V/III ratio of 112 and above. For example, Figure 4.10 (a)-(e) displays a bright-field HRTEM image and selective area diffraction pattern captured at the [110] zone axis of a NW grown at 400 ºC with a V/III ratio of 112 and a 1 min AsH_3 pre-flow. The NW exhibits a ZB phase with an occasional stacking fault or inclined twin defect at its base, as indicated in Figure 4.10 (c), likely resulting from instabilities during the initial stages of growth. All vertical NWs oriented in the [111] direction have contact angles of 130º and 110º on either side of the gold nanoparticle, regardless of their growth temperature.

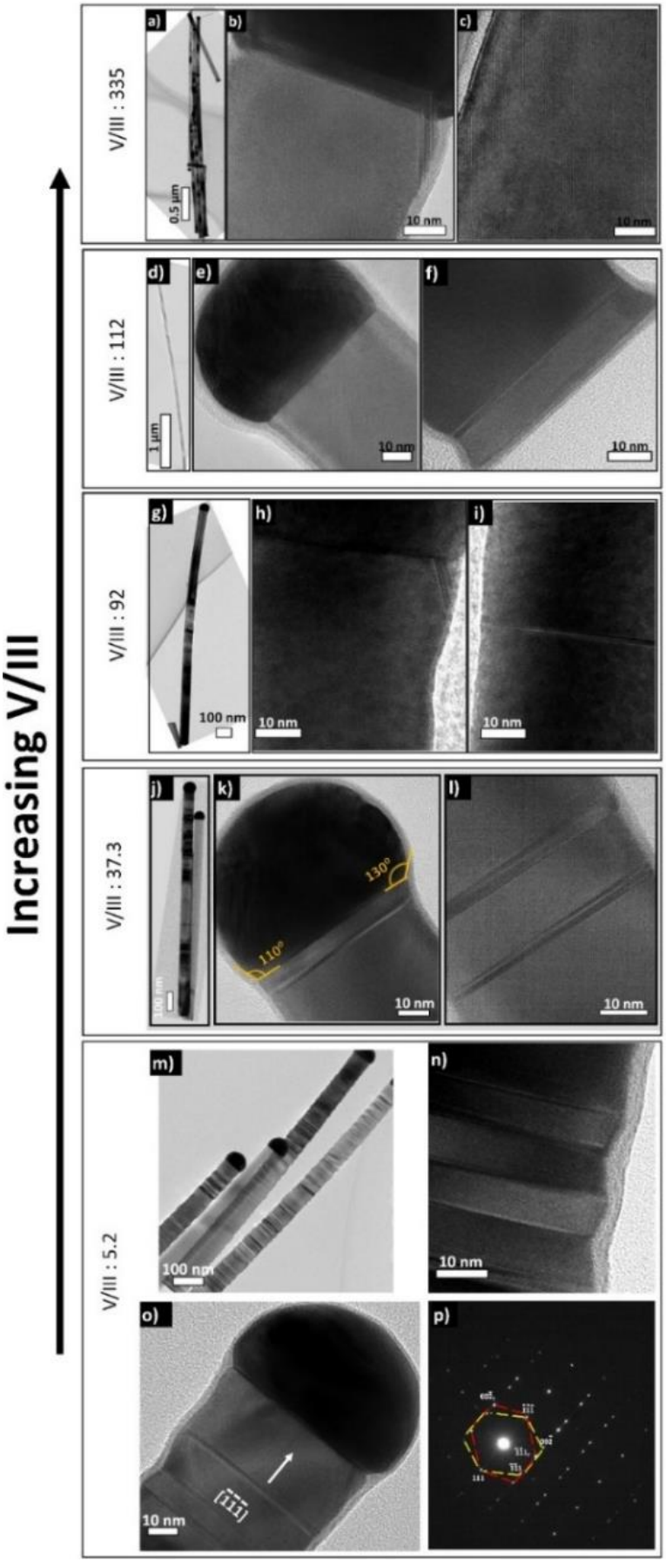
Increasing V/III
V/III : 335
V/III : 112
V/III : 92
V/III : 37.3
V/III : 5.2
a)
b)
c)
d)
e)
f)
g)
h)
i)
j)
k)
l)
m)
n)
o)
p)
0.5 µm
1 µm
100 nm
10 nm
130°
110°
[111]

Figure 4.10. TEM investigations of the crystal phase evolution from a V/III ratio of 5.2 to 335 with 1 min AsH_3 pre-flow and a growth temperature of 400 ºC. a), b) and c) show respectively the full length, top and middle of the NW with a pure ZB phase grown at V/III = 335. A NW grown at V/III = 112, the pure ZB phase with defects only in the base can be observed in d), e) and f). The full length of NW, top and middle of NWs are shown in g), h) and i), respectively, demonstrating occasional stacking faults along the length of the NW. The full length, top and middle of the NW grown at V/III = 37.3 are shown in j), k) and l), respectively. Full length, middle, top and SADP from the middle of the NW grown with low V/III ratio of 5.2 are shown in m), n), o), and p), respectively.

After conducting detailed HRTEM analysis on vertical NWs grown under different conditions (as shown in Figures 4.9 and 4.10), we found that a low growth temperature and high V/III ratio results in a pure zinc blende (ZB) structure as shown in Figure 4.11. This finding is consistent with previous reports from our group on VLS GaAs NWs grown on a GaAs substrate by Joyce et al., where it was demonstrated that a low temperature and high V/III ratio yield a twin-free ZB structure. In contrast, a high temperature and low V/III ratio yield a pure wurtzite (WZ) structure.[5]

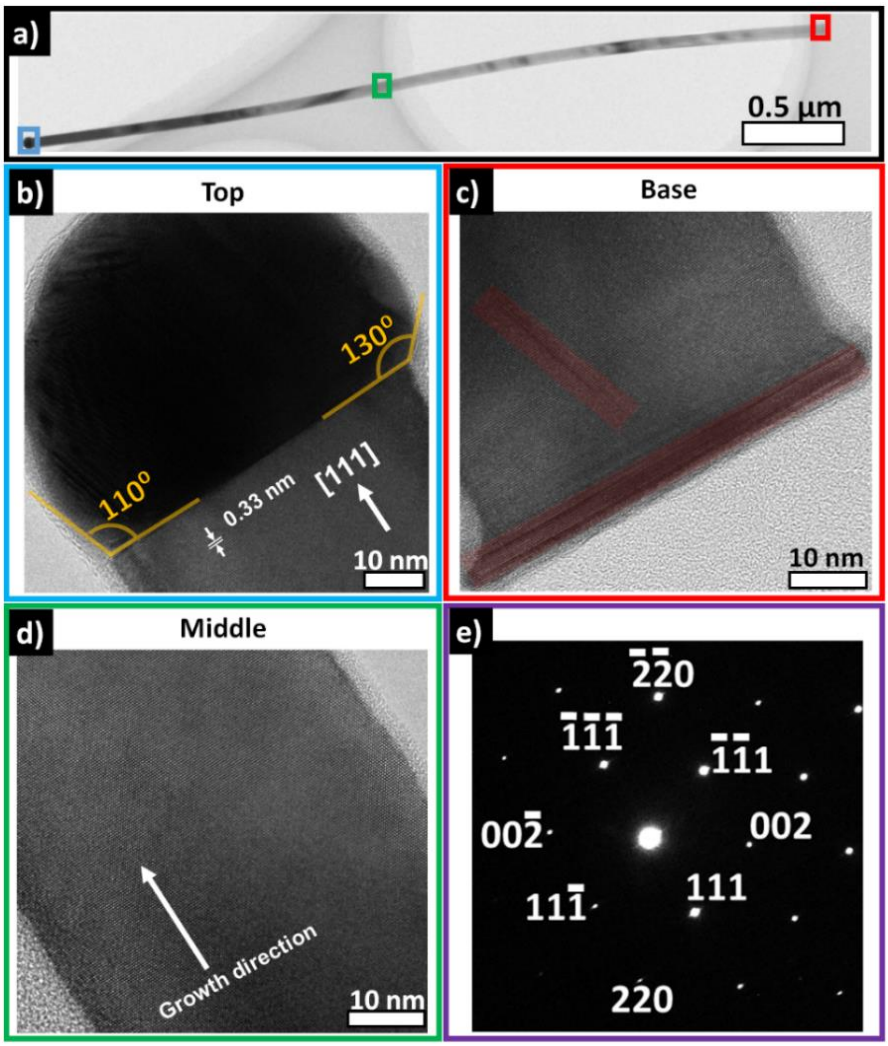

Figure 4.11. TEM investigation of a GaAs NW grown on synthetic mica with a V/III ratio of 112, a growth temperature of 400 ºC and 1 min AsH_3 pre-flow. a) Low-magnification TEM image of a NW. The scale bar is 0.5 µm. (b-d) HRTEM images of the different regions of the NW as indicated by the coloured boxes. e) The indexed selected area diffraction pattern (SADP), obtained from the middle section of the NW, illustrating defect free zinc blende crystal structure.

4.6 Polarity of GaAs NWs

To determine the orientation of vertical NWs, previous studies have used contact angle and surface energy considerations. However, our investigation using aberration-corrected HAADF-STEM reveals evidence of [111] B polarity in our NWs, despite an

asymmetric Au seed with a truncated facet suggesting growth along the A polar orientation. The polarity of GaAs NWs is intrinsic due to the ionicity of the atoms, with usual [111] B polarity when grown on GaAs or silicon substrates. Although several studies have explored engineering the polarity of NWs grown on conventional III-V substrates, there is limited information on NWs grown on van der Waals substrates, apart from a report indicating that ZnO NWs grow on mica surfaces with A polarity.[22] Figure 4.12 displays HAADF-STEM images of a NW and intensity line scans along the growth direction, revealing [111] B polarity. The NW tip and base are displayed in Figures 4.12 (a) and (d), with (b) and (e) presenting the GaAs 'dumbbells' from the NW tip and base, respectively. The yellow and green boxes in (b) and (d) illustrate the direction of the line scan, and the intensity profiles of the scans are presented in (c) and (f). The signal intensity is directly proportional to the atomic number, with As atoms being brighter due to their slightly higher atomic number than Ga. The distance between the Ga and As atoms in the 'dumbbell' is 0.14 nm, consistent with the reported value of the Ga-As bond.[23] Therefore, the determination of As-terminated growth of the NWs conclusively proves their [111] B polarity.

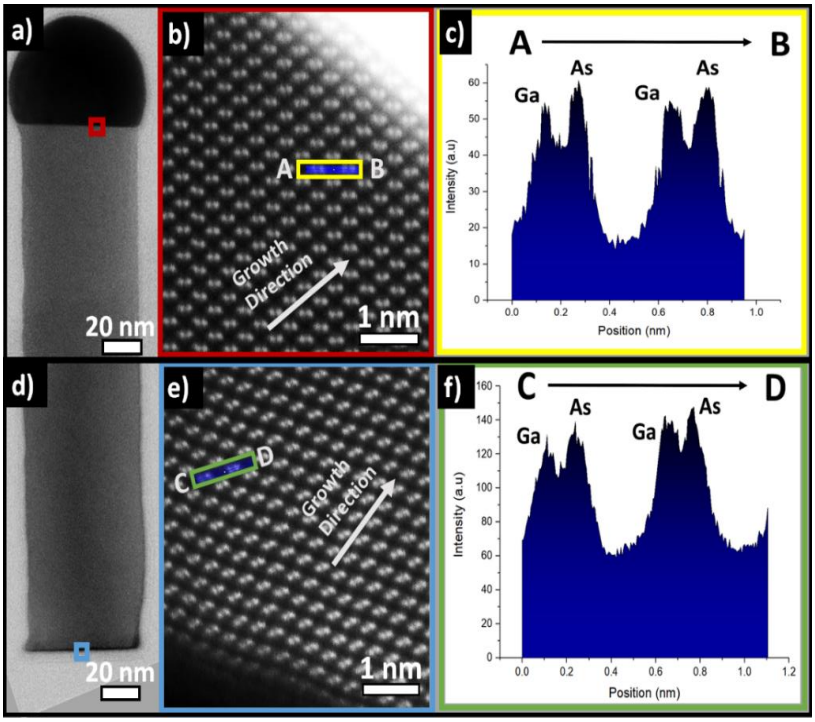

Figure 4.12 AC-HAADF-STEM images of GaAs NW. a) and d) show the NW tip and bottom part, respectively. b) and e) show the GaAs 'dumbbells'. c) and f) show the line scan intensity in the direction of growth from the top and base of the NW, respectively, confirming B polarity.

4.7 Computational methodology

We conducted a theoretical study on the bonding between GaAs and synthetic mica using first-principles electronic structure calculations within the density functional theory (DFT) framework. The study was carried out at the MATES Lab, Harish-Chandra Research Institute Allahabad by Prof. Sudip Chakraborty and Ponnappa Kechanda Prasanna. Our calculations employed the Vienna ab-initio simulation package code with the projector augmented wave formalism, using the generalised gradient approximation with the Predrew-Bruke-Ernzerhof functional to treat exchange and correlation energies. We constructed a van der Waals heterostructure consisting of a GaAs NW along the (111) direction situated on a 2×2×1 supercell of a 2D mica slab along the (001) direction. To

attain the minimum energy convergence of 10^{-4} eV and force convergence criteria of 10^{-2} eV $Å^{-1}$, we subjected all structures to ionic relaxation. The converged energy cut-off was 500 eV, which was used throughout the calculation. We used the 3×3×1 Monkhorst–Pack scheme to sample the Brillouin zone for the ionic relaxation of the pure mica and van der Waals heterostructure, and 1×1×5 for GaAs. We added adequate vacuum along the z-axis for the GaAs and 2D mica system, and vacuum along the x and y-directions to the GaAs NW to prevent interactions between the periodic images. We considered different possibilities of spacing between the GaAs NW and mica to determine the minimum energy configuration of the van der Waals heterostructure.

4.7.1 Theoretical analysis based on electronic structure properties

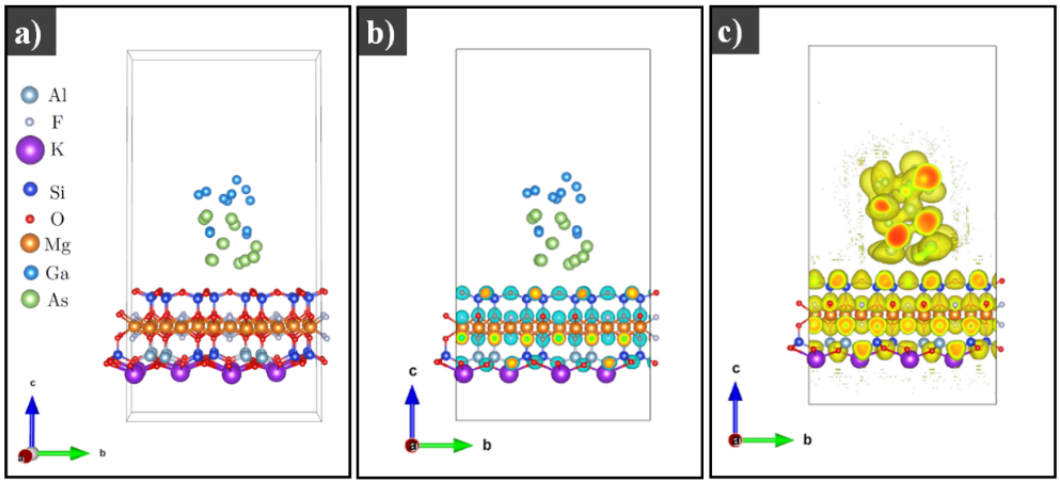

Figure 4.13 van der Waals heterostructure consisting of a GaAs [111] NW and mica [001] surface. (a) Optimised minimum energy configuration, (b) charge distribution, and (c) electron localisation function of the van der Waals heterostructure.

Figure 4.13 (a) shows the geometrical representation of the individual and hybrid systems after obtaining their minimum energy configurations. During the optimisation of the hybrid system, we increased the spacing between the 2D mica and GaAs NW and found that it was optimised at 3.2 Å, indicating weaker van der Waals bonding between the GaAs NW and mica. We can determine the nature of the bonding between GaAs and mica by analysing the charge distribution at the interface of the two systems, as shown in Figure 4.13 (b). We found that there is negligible charge transfer between mica and GaAs, indicating a physisorption type bonding, unlike conventional covalent bonding when GaAs NWs are grown on III-V substrates. This is further supported by the electron localisation, shown in Figure 4.13 (c), which indicates no strong electron sharing between the NW and mica. The increase in the spacing between the GaAs NW and 2D mica surfaces in the lowest energy configuration, and the negligible charge transfer between the two systems, provide theoretical evidence that the considered (111) GaAs NW on top of (001) 2D mica surface primarily has van der Waals interactions.

4.8 Conclusions

This chapter presents the successful synthesis of vertical GaAs NWs on a synthetic mica substrate using Au-catalysed VLS growth by MOCVD. The study systematically investigated the impact of growth parameters, such as temperature and V/III ratio, on the maximum yield of vertical NWs, as well as the effect of AsH_3 pre-flow on the vertical yield. The results show that the resulting NWs have high optical quality, as evidenced by room-temperature PL measurements with an emission at 1.43 eV, which corresponds to the band edge emission of GaAs.

Under optimal growth conditions, the NWs possess a ZB crystal structure with occasional stacking faults or inclined twin defects near the base. The polarity of the vertical NWs is [111] B. Theoretical investigations within the DFT framework revealed that the bonding between GaAs NWs and mica is a physisorption-type bonding, which is different from the conventional covalent bonding observed when GaAs NWs are grown on III-V substrates.

Importantly, the study found that the NWs can be easily peeled off from the 2D layered mica substrate, making them potentially suitable for flexible device applications. This opens the possibility of developing NW-based optoelectronic devices that can be grown epitaxially on more affordable 2D substrate materials. Furthermore, direct growth on transparent substrates like mica presents an opportunity for further investigation of NW arrays, which were previously restricted by substrate effects.

These findings have significant implications for the development of flexible and cost-effective NW-based optoelectronic devices.

4.9 References

(1) Koma, A. Van Der Waals Epitaxy for Highly Lattice-Mismatched Systems. *J. Cryst. Growth* **1999**, *201–202*, 236–241. https://doi.org/10.1016/S0022-0248(98)01329-3.

(2) Utama, M. I. B.; Zhang, Q.; Jia, S.; Li, D.; Wang, J.; Xiong, Q. Epitaxial II-VI Tripod Nanocrystals: A Generalization of van Der Waals Epitaxy for Nonplanar Polytypic Nanoarchitectures. *ACS Nano* **2012**, *6* (3), 2281–2288. https://doi.org/10.1021/nn204344z.

(3) Anyebe, E. A.; Kesaria, M. Recent Advances in the Van Der Waals Epitaxy Growth of III-V Semiconductor Nanowires on Graphene. *Nano Sel.* **2021**, *2* (4), 688–711. https://doi.org/10.1002/nano.202000142.

(4) Chugh, D.; Adhikari, S.; Wong-Leung, J.; Lysevych, M.; Jagadish, C.; Tan, H. H. Improving the Morphology and Crystal Quality of AlN Grown on Two-Dimensional HBN. *Cryst. Growth Des.* **2020**, *20* (3), 1811–1819. https://doi.org/10.1021/acs.cgd.9b01543.

(5) Joyce, H. J.; Wong-Leung, J.; Gao, Q.; Hoe Tan, H.; Jagadish, C. Phase Perfection in Zinc Blende and Wurtzite III- V Nanowires Using Basic Growth Parameters. *Nano Lett.* **2010**, *10* (3), 908–915. https://doi.org/10.1021/nl903688v.

(6) Wallentin, J.; Kriegner, D.; Stangl, J.; Borgström, M. T. Au-Seeded Growth of Vertical and in-Plane III-V Nanowires on Graphite Substrates. *Nano Lett.* **2014**, *14* (4), 1707–1713. https://doi.org/10.1021/nl403411w.

(7) Messmer, C.; Bilello, J. C. The Surface Energy of Si, GaAs, and GaP. *J. Appl. Phys.* **1981**, *52* (7), 4623–4629. https://doi.org/10.1063/1.329342.

(8) Wang, S.; Zhang, Y.; Abidi, N.; Cabrales, L. Wettability and Surface Free Energy of

Graphene Films. *Langmuir* **2009**, *25* (18), 11078–11081. https://doi.org/10.1021/la901402f.

(9) G.F.S. The Splitting Strength of Mica. *J. Franklin Inst.* **1931**, *211* (1), 122. https://doi.org/10.1016/s0016-0032(31)90361-x.

(10) Zhang, S. B.; Wei, S. H. Surface Energy and the Common Dangling Bond Rule for Semiconductors. *Phys. Rev. Lett.* **2004**, *92* (8), 8–11. https://doi.org/10.1103/PhysRevLett.92.086102.

(11) Yuan, X.; Yang, J.; He, J.; Tan, H. H.; Jagadish, C. Role of Surface Energy in Nanowire Growth. *J. Phys. D. Appl. Phys.* **2018**, *51* (28), 283002. https://doi.org/10.1088/1361-6463/aac9f4.

(12) Ginocchio, I. F. Title Synthetic Mica and Its Appplications. **2006**, *124*, 119–124.

(13) Crystal Structure Analysis of Synthetic Fluorophlogopite. *Am. Mineral.* **1973**.

(14) Maliakkal, C. B.; Jacobsson, D.; Tornberg, M.; Persson, A. R.; Johansson, J.; Wallenberg, R.; Dick, K. A. In Situ Analysis of Catalyst Composition during Gold Catalyzed GaAs Nanowire Growth. *Nat. Commun.* **2019**, *10* (1), 4577. https://doi.org/10.1038/s41467-019-12437-6.

(15) Thornton, J. M. C.; Woolf, D. A.; Weightman, P. Surface Reconstructions and Phase Transitions on the GaAs(111)B Surface. *Surf. Sci.* **1997**, *380* (2–3), 548–555. https://doi.org/10.1016/S0039-6028(97)00042-3.

(16) Czaban, J. A.; Thompson, D. A.; LaPierre, R. R. GaAs Core-Shell Nanowires for Photovoltaic Applications. *Nano Lett.* **2009**, *9* (1), 148–154. https://doi.org/10.1021/nl802700u.

(17) Gutsche, C.; Niepelt, R.; Gnauck, M.; Lysov, A.; Prost, W.; Ronning, C.; Tegude, F. J.

Direct Determination of Minority Carrier Diffusion Lengths at Axial GaAs Nanowire P-n Junctions. *Nano Lett.* **2012**, *12* (3), 1453–1458. https://doi.org/10.1021/nl204126n.

(18) Demichel, O.; Heiss, M.; Bleuse, J.; Mariette, H.; Fontcuberta Morral, I. A. Impact of Surfaces on the Optical Properties of GaAs Nanowires. *Appl. Phys. Lett.* **2010**, *97* (20). https://doi.org/10.1063/1.3519980.

(19) Phys, A. Long Minority Carrier Lifetime in Au-Catalyzed GaAs/$Al_xGa_{1-x}As$ Core-Shell Nanowires. *Appl. Phys. Lett.* **2012**, *101* (2), 2311–2314.

(20) Zeng, H.; Yu, X.; Fonseka, H. A.; Boras, G.; Jurczak, P.; Wang, T.; Sanchez, A. M.; Liu, H. Preferred Growth Direction of III-V Nanowires on Differently Oriented Si Substrates. *Nanotechnology* **2020**, *31* (47), 475708. https://doi.org/10.1088/1361-6528/abafd7.

(21) Breuer, S.; Feiner, L. F.; Geelhaar, L. Droplet Bulge Effect on the Formation of Nanowire Side Facets. *Cryst. Growth Des.* **2013**, *13* (7), 2749–2755. https://doi.org/10.1021/cg301770f.

(22) Utama, M. I. B.; Belarre, F. J.; Magen, C.; Peng, B.; Arbiol, J.; Xiong, Q. Incommensurate van Der Waals Epitaxy of Nanowire Arrays: A Case Study with ZnO on Muscovite Mica Substrates. *Nano Lett.* **2012**, *12* (4), 2146–2152. https://doi.org/10.1021/nl300554t.

(23) De La Mata, M.; Magen, C.; Gazquez, J.; Utama, M. I. B.; Heiss, M.; Lopatin, S.; Furtmayr, F.; Fernández-Rojas, C. J.; Peng, B.; Morante, J. R.; Rurali, R.; Eickhoff, M.; Fontcuberta I Morral, A.; Xiong, Q.; Arbiol, J. Polarity Assignment in ZnTe, GaAs, ZnO, and GaN-AlN Nanowires from Direct Dumbbell Analysis. *Nano Lett.* **2012**, *12* (5), 2579–2586. https://doi.org/10.1021/nl300840q.

Chapter 5

Ultra-thin GaAs quantum wires: structural and electronic structure properties

5.1 Introduction

True electronic confinement characteristics manifest only when the size shrinks below the exciton Bohr radius. As the size decreases below the exciton Bohr radius, the spatial confinement becomes significant, leading to quantized energy levels and enhanced electronic confinement properties. To harness the true quantum confined characteristics, an ideal GaAs quantum wire must have radius below ~ 11 nm.[1] A controlled synthesis of GaAs nanowires (NWs) with core diameter as low as 7 nm was synthesised using reactive ion etching technique, successfully demonstrating wavelength tunability as a result of quantum confinement effect. [2] Pure zinc blende phase GaAs NWs with diameters ranging 15 nm down to 5 nm were achieved using Hydride vapour phase epitaxy (HVPE) technique using gold catalyst.[3] Despite progress in nanowire synthesis and applications, the epitaxial growth of large area freestanding GaAs quantum wires is still not explored. This opens a wide range of research questions, especially to understand and harness the optical and electronic confinement properties of free-standing quantum wires. Experimental study of quantum confinement and electronic structure changes in III-V quantum wires is especially challenging, as it needs precise control of the quantum wire dimensions while maintaining a high structural and crystal quality.

In this chapter, we demonstrate a high yield of GaAs NWs with diameters 20 nm and below over a large area on synthetic mica substrate. Structural, electronic structure and

bandgap properties of these ultra-thin wires are investigated in detail. Experimental demonstration of zinc blende crystal structure, binding energy, bandgap and electronic structure properties of ultra-thin NWs are presented.

5.2 Structural Properties of Quantum Wires

5.2.1 Morphology and crystal structure

The experimental exploration of true quantum confinement in technologically relevant III-V NWs requires the synthesis of uniform cross sectional non-tapered NWs with their cross-sections below the exciton Bohr radius. In this chapter we will explore a large area synthesis GaAs NWs with diameters of 5 nm, (sample S1), 10 nm, (sample S2) and 20 nm (sample S3). For brevity, these NWs will be called quantum wires.

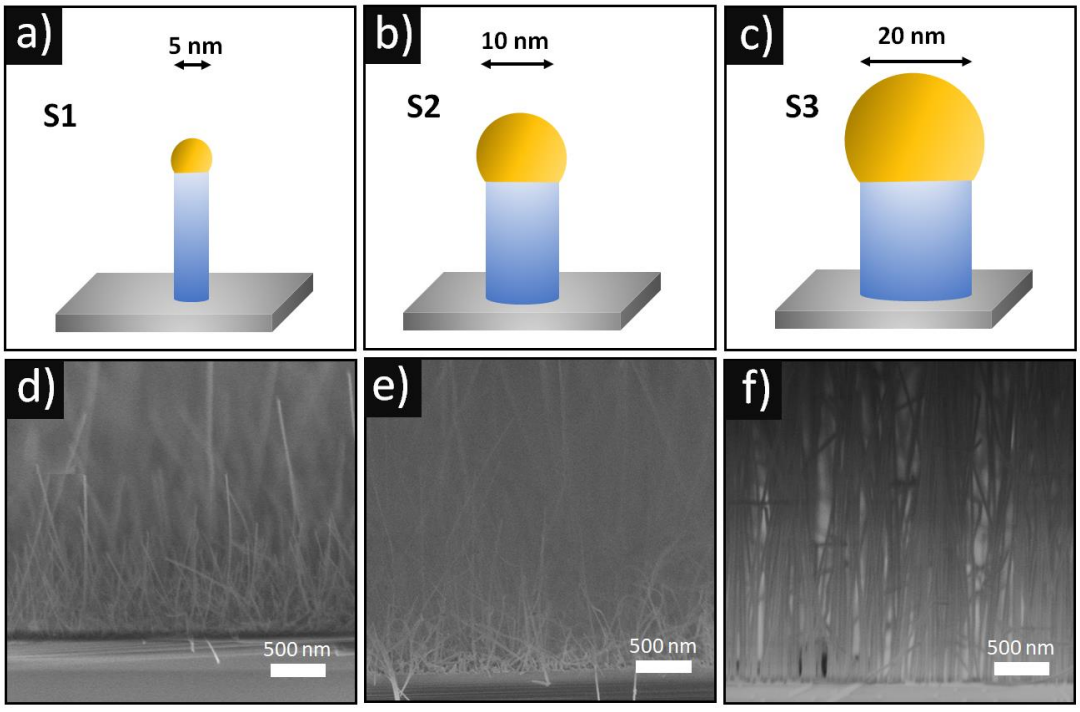

Figure 5.1 (a)-(c) Schematic illustration of samples S1, S2 and S3 grown using 5,10 and 20 nm gold seed particles. (d)-(f) Cross- sectional SEM images of S1, S2 and S3, respectively.

Figure 5.1 (a)-(c) shows the schematic of the samples S1, S2 and S3, respectively. The cross-sectional scanning electron microscopy images in Figure 5.1 (d)-(f) clearly depict the wires grown vertically on synthetic mica substrate. The quantum wires were found to have very little tapering, a morphology that is advantageous for many quantum confinement studies as it demands uniformity in diameter for accurate measurement of various optical properties such as emission wavelength. The chapter 4 described the growth and characterisation of GaAs NWs on synthetic mica using a 60 nm gold seeds which have a high (> 60%) vertical yield. [4]The vertical NWs grown at the same conditions as this work (a low temperature and a high V/III ratio) were found to have a zinc blende phase with a [111] B polarity. The gold seed investigated after growth were found to have a contact angle asymmetry on either side of the gold seed. The formation of pure zinc blende structure was attributed to the surface energy of gold-mica interface.

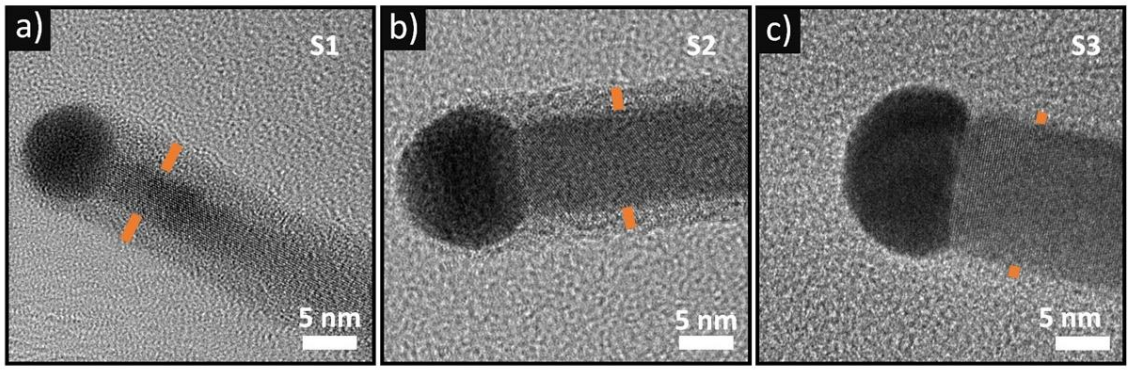

Figure 5.2. (a)-(c) HRTEM images showing the top part of sample S1, S2 and S3, respectively. All samples have a zinc blende crystal phase. The native oxide formed is highlighted with orange marks.

VLS growth of GaAs quantum wires on synthetic mica regardless of their diameter were found to have a zinc blende phase as shown in figure 5.2 (a)-(c). According to Glass *et.al.*,[5] the high super saturation in the smaller gold catalysts leads to wurtzite phase in NWs.[5] Our results here are in contradiction to this prediction of energetically favoured wurtzite crystal structure in ultra-thin wires. Akiyama *et.al*. [6], systematically investigated

the relative stability between wurtzite and zinc blende structures in group III–V semiconductor NWs based on an empirical potential, which incorporates electrostatic energy due to valence-bond and ionic charges. Their investigation on the energy differences between wurtzite and zinc blende structures of 12 compound semiconductor NWs with diameter of 1– 22 nm shows that the wurtzite NWs are stabilised for small diameter. For arsenide NWs, the paper clearly shows the existence of a critical diameter of 10.8 – 20.1 nm. However, recent experimental reports suggest that VLS growth of ultra-thin GaAs wires can form a pure zinc blende structure. For instance, Gil *et.al.*[3], reported the gold catalyst-assisted synthesis of 20 μm-long GaAs NWs by the VLS - HVPE exhibiting a pure zinc blende phase for radii lower than 15 nm down to 5 nm. They demonstrated that for their growth conditions, VLS growth takes place at high liquid chemical potential that originates from very high influx of both As and Ga. This yields a Ga concentration systematically higher than 0.62 in the Au−Ga−As droplets. The high Ga concentration decreases the surface energy of the droplets, which disables nucleation at the triple phase line thus preventing the formation of wurtzite structure regardless of NW diameter.

VLS growth of GaAs on glass by Veer Dhaka *et.al.* [7] demonstrated pure zinc blende phased GaAs NWs. They proposed the cause is due to unintentional doping of the GaAs NWs from the glass substrate. Na and Si atoms are mobile at the growth temperatures (> 500 ºC) reported in their work and could be incorporated in the NWs during growth. Although experimentally not detected, it is speculated that Na could dramatically change the VLS mechanism resulting in single-phase purity. They also observe that additional sensitive experiments are required to ascertain the role of impurities on the growth and structure of the NWs grown on glass substrate.

Thus, either a high Ga concentration in the Au-Ga-As catalyst and/or an unintentional doping of gold seed from the synthetic mica could potentially alter the surface energy at the gold-quantum wire interface and favour the growth of zinc blende phase wires regardless of diameter.

Although convincing from the above discussion, the reasons for phase purity of quantum wires grown on synthetic mica regardless of the diameter is yet to be explored in detail experimentally. This requires a dedicated study to investigate the effect of growth parameters and sensitive experimental measurements of the gold catalyst and NWs alike.

5.2.2 Lattice strain in quantum wires

NWs have a large surface-to-volume ratio that causes significant lattice contraction, especially when they have free surfaces. This contraction becomes more pronounced as the size of the NWs decreases. For example, silicon NWs that are not modified by passivation during or after growth are shown to have undergone surface reconstructions, leading to significant deviations in the Si-Si bond length.[8] Another study that fabricated silicon NWs down to 1.3 nm in diameter reported a change in density of states and clear shift in bandgap energy from 1.1 eV for 7 nm to 3.5 eV for 1.3 nm diameter nanowire using scanning tunnelling microscope measurements. [9]

While III-V NWs, especially GaAs based nanostructures are extensively studied, most of them have focused on passivated NWs or those embedded within a structure.[10,11] The effect of GaAs NW diameter has only been explored for studying the effect of quantum confinement on the bandgap properties. While bandgap properties are important, it is equally important to investigate changes in lattice and electronic structure as a function of quantum wire diameter.

Lattice relaxation of the quantum wires (contraction or expansion) is experimentally determined from high-resolution transmission electron microscopy (HRTEM) studies.

Several studies have developed general equations that describe the lattice contraction and surface stress of fcc nanocrystals.[12] These equations are derived from the Laplace-Young equation and account for the size-dependence of the solid-liquid interface energy.[13] Their predictions have been validated through experimental measurements of lattice contraction and surface stress of nanoparticles and thin films, as well as theoretical calculations. According to these models, the physical origin of the lattice strain (ε) given by $\frac{\Delta a}{a}$ is the hydrostatic pressure on the surface induced by intrinsic surface stress (f), where Δa is the difference between the measured quantum wire lattice constant and the bulk lattice constant. Thus, lattice strain is a measure of the surface stress of nanomaterials and is highly dependent on the surface species.

For a nanocrystal (particle or wire) with a diameter (D) one can write the Laplace-Young equation [12] as:

$$P = \frac{4f}{D} \qquad (1)$$

where P is the pressure difference between the internal pressure in the crystal and external pressure in the surrounding material.

Considering the compressibility (κ) for a cubic lattice, lattice strain $\varepsilon(D)$ along the radius can be expressed as:

$$\varepsilon(D) = \frac{\Delta a}{a} = \frac{4}{3}\,\kappa\frac{f}{D} \qquad (2)$$

Rearranging equation (2) and considering the definition of compressibility (κ) as the reciprocal of bulk modulus, we arrive at the equation for surface stress (f) given by:

$$f = \frac{3}{4}\frac{\Delta a}{a}\,\frac{D}{\kappa} \qquad (3)$$

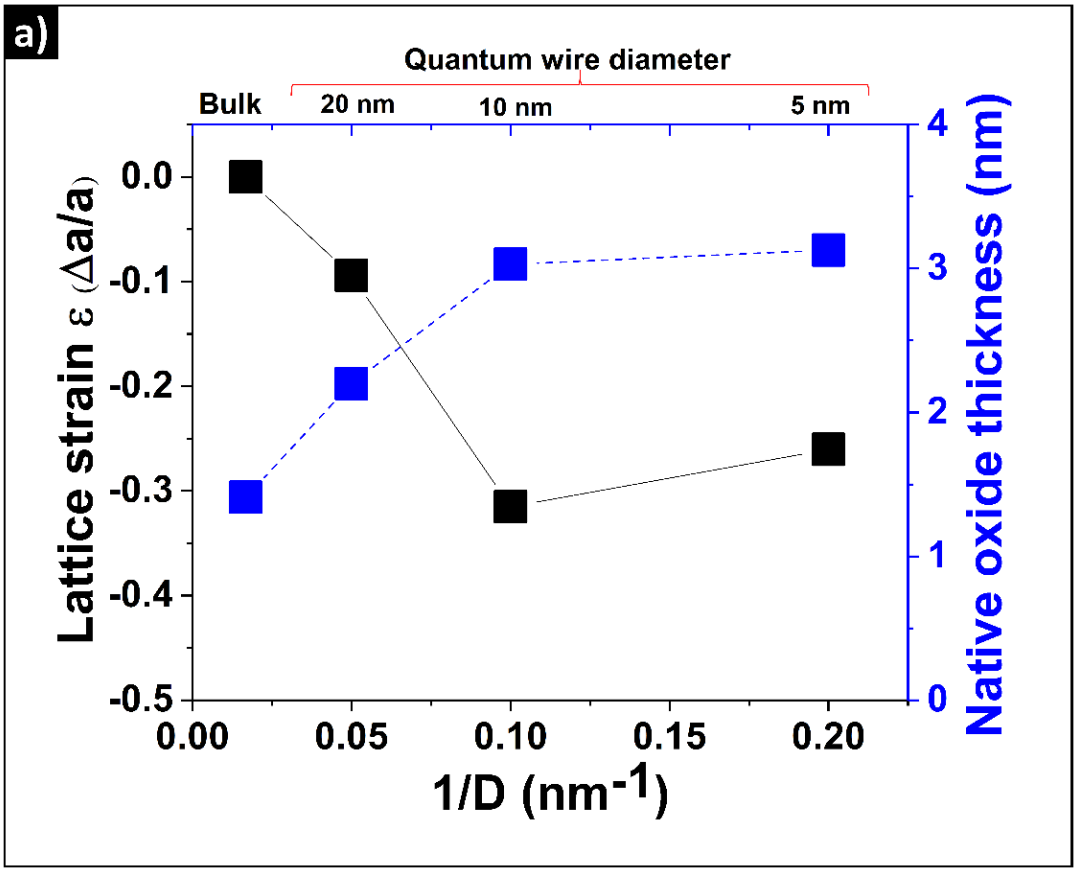

Figure 5.3. Variation in lattice deformation of GaAs quantum wires as a function of the reciprocal diameter (1/D) (black data points) extracted from HRTEM lattice parameter measurements. Blue data points show the variation of native oxide thickness as a function of quantum wire diameter.

The lattice strain $\frac{\Delta a}{a}$ of the quantum wires is determined through experimental analysis of HRTEM images. A bulk modulus of (reciprocal of compressibility ($\frac{1}{\kappa}$)) 76.4 GPa is derived from literature for GaAs. The lattice spacing, specifically d_{111} along the [111] growth direction of the quantum wires, is extracted from the HRTEM images to determine the lattice constant (a) as a function of the diameter of the quantum wires. Figure 5.3 (a) shows a plot of the lattice strain $\frac{\Delta a}{a}$ against the reciprocal of the quantum wire diameter. The data points in black correspond to the calculated lattice strain while

the blue squares represent the measured native oxide thickness obtained from the HRTEM investigations of the quantum wires.

The calculated surface stress for various quantum wire diameters are listed in table 1.

Quantum wire diameter (nm)	**Lattice strain $\varepsilon(D)$ (%)**	**Calculated Surface Stress (N/m)**
5	26.03	-74.57
10	31.51	-180.55
20	9	-107.72

Table 5.1. Surface stress of GaAs quantum wires calculated using Equation 2.

From the surface stress calculation using equation (3), It is observed that the 20 and 10 nm diameter quantum wires experience a negative surface stress of 107.72 N/m and 180.55 N/m, respectively, which correlate with the observed lattice contraction. However, the 5 nm diameter quantum wire exhibits significantly less negative surface stress compared to the 10 and 20 nm diameter wires. At such small dimensions, a high percentage of atoms are on the surface and interact with the surrounding native oxide, causing lattice strain relaxation, which results in an expansion of the lattice. Research has shown that lattice contraction occurs in metal nanoparticles such as Pd,[14] Pt,[15] as well as in semiconductors such as free-standing wurtzite CdSe nanocrystals.[16] On the other hand, metal oxide nanocrystals reportedly exhibit lattice expansion.[17] It is worth noting that the lattice constant of free-standing nanostructures often undergoes contraction, while nanostructures embedded in a matrix of different materials or chemically passivated can result in lattice expansion.

The experimental lattice relaxation in GaAs quantum wires and other materials indicates that lattice relaxation can be explained through the bond-order-length-strength (B-OLS) mechanism,[18] which suggests that the imperfection in coordination number of an atom at a surface causes the remaining bonds of the lower-coordinated surface atoms to relax spontaneously, resulting in a rise in the bond energy. The increase in bond energy contributes not only to the cohesive energy of the surface atom but also to the energy density in the relaxed region, which directly relates to the thermodynamic properties of a nanosolid. Furthermore, the rise in binding energy density affects the system Hamiltonian that determines the entire band structure and related properties, such as the bandgap, core-level shifts, phonon frequency, Young's modulus and surface stress. Thus, it is established that the GaAs quantum wires experience significant negative surface stress compared to its bulk counterpart (as given in table 5). This result has great significance to further understand the physical and chemical properties of the extremely low-dimensional wires. In the following section the electronic structure of the GaAs quantum wires is studied using photoelectron spectroscopy techniques.

5.3 X-ray photoelectron spectroscopy (XPS) and ultraviolet spectroscopy (UPS)

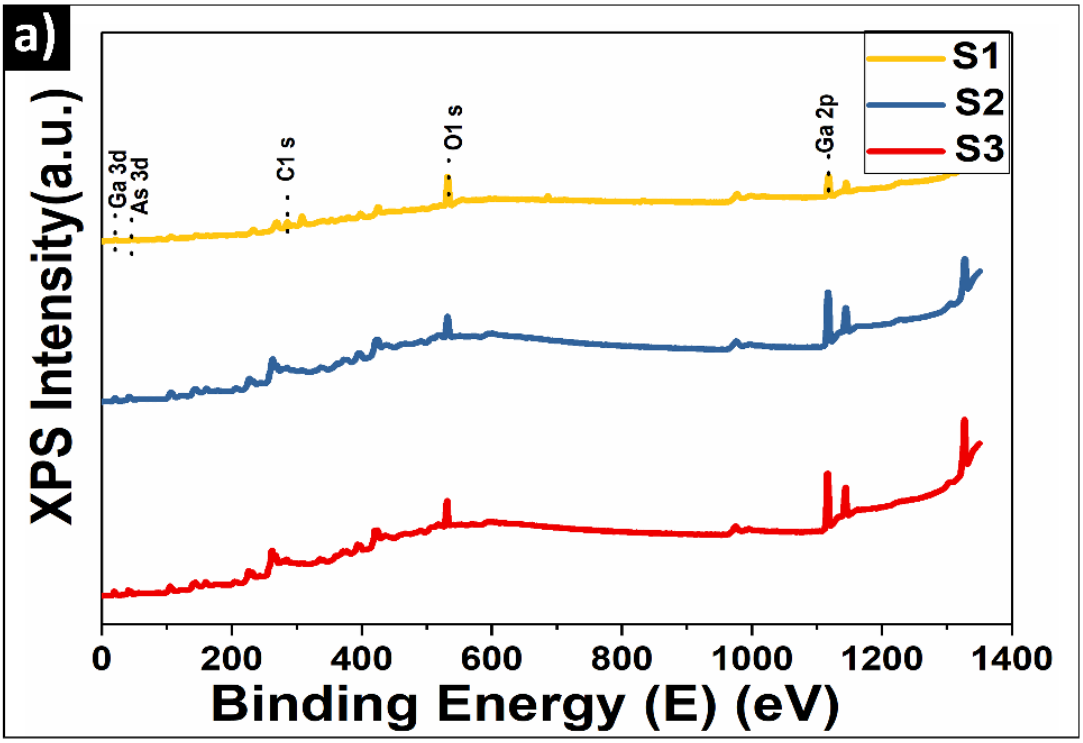

Figure 5.4. (a) Survey XPS spectra of samples S1, S2 and S3 with a diameter of 5, 10 and 20 nm, respectively.

Combined XPS and UPS is a powerful surface sensitive technique that can reveal the electronic band structure information such as binding energy core-level shifts, valence band maximum (VBM), bandgap and work function of materials. Figure 5.4 (a) provides the XPS survey spectra of samples S1, S2 and S3. The peaks noted are Ga 3d, As 3d, C1s, O1s and Ga 2p. The presence of C1s and O1s are from the carbon-contamination and native oxide on the quantum wire surface, respectively.

The compounds with a given chemical composition has a signature electronic structure. The core-level binding energy of electrons in pure ionic compounds remains the same as for the free ions. The shift of core-level electrons is such that donor level is shifted to

higher energies and acceptor level to lower energy. The core-levels can shift in nano-dimensional crystals as a function of their size giving rise to quantum confinement effects. Figure 5.5 (a) demonstrates the centroid of Ga 3d core-level binding energy shift of samples with varying diameter. The Ga 3d core-level shifts to higher energies as the quantum wire diameter is increased from 5 to 20 nm. However, the shift has to be considered corresponding to the valence band energy for each sample i.e. a change in binding energy (ΔBE) is equal to the difference between the Ga 3d core level binding energy (E_{CL}) and valence band energy (E_V).

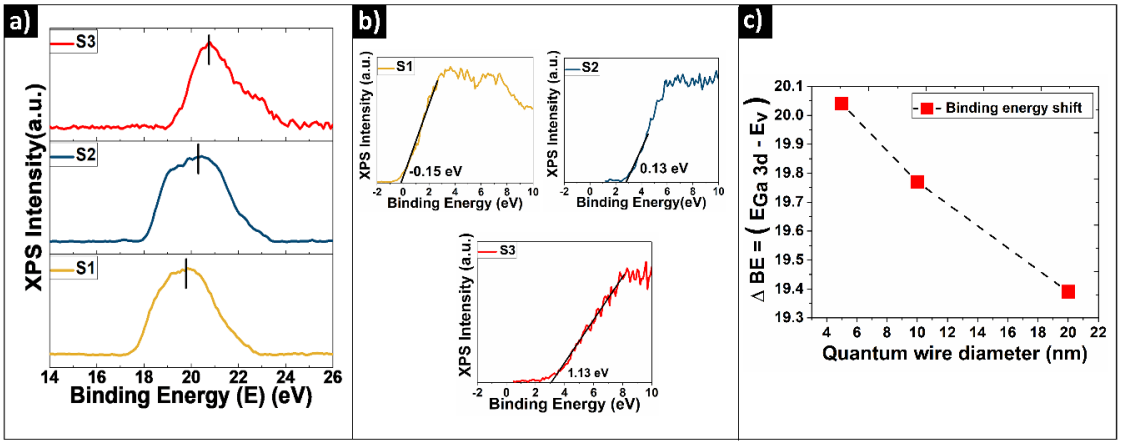

Figure 5.5. (a) Ga 3d core-level energy spectra (b) valence band maximum of samples S1, S2 and S3. (c) Effective binding energy shift as a function of quantum wire diameter.

Figure 5.5 (b) shows the VBM spectra from S1, S2 and S3. The VBM of the various samples were determined by the usual method of linear extrapolation of the leading edge of the VB spectrum (with an accuracy of about ±0.05 eV). The difference between the Ga 3d core level binding energy and valence band energy ($\Delta BE = E_{CL} – E_V$) for samples S1, S2 and S3 calculated from Figure 5.5 (a) and (b) are 20.27, 20.13 and 19.65 eV, respectively. These results, as plotted in Figure 5.5 (c), show that the binding energy increases with reducing GaAs quantum wire diameter. We attribute the observed E_{CL} shift to higher energies due to the lattice relaxation in the ultra-thin quantum wires.

Following the bond OLS correlation, in order to minimise the system energy, the binding energy of the relaxed bond will reduce (rise in absolute value). Such a relaxed bond is stronger too. Albeit bond relaxation may vary from system to system, it is important to note that the nature of specific chemical bond itself is not important.

Understanding the electronic structure of valence band is very important to understand the physical properties of the wires. The nature of the density of states (DOS) near the Fermi energy level would determine the reactivity of the material. Electrons near the Fermi energy level are readily available for any chemical reaction or electrical transport. The valence band narrowing effect as the quantum wire diameter is reduced is of significance when understanding the origin of work function variation and optical bandgap variation. As shown in figure 5.5 (b), the corrugation of the DOS near the Fermi energy level is much enhanced for sample S1 and S2 compared to sample S3. This size dependent shift in valence band position with the change in quantum wire diameter can be attributed to lattice distortion (lattice expansion and lattice contraction) resulting in a more reactive material. Hence, from the observed VB shift, we can see there is a size dependent enhanced reactivity in the GaAs quantum wires.

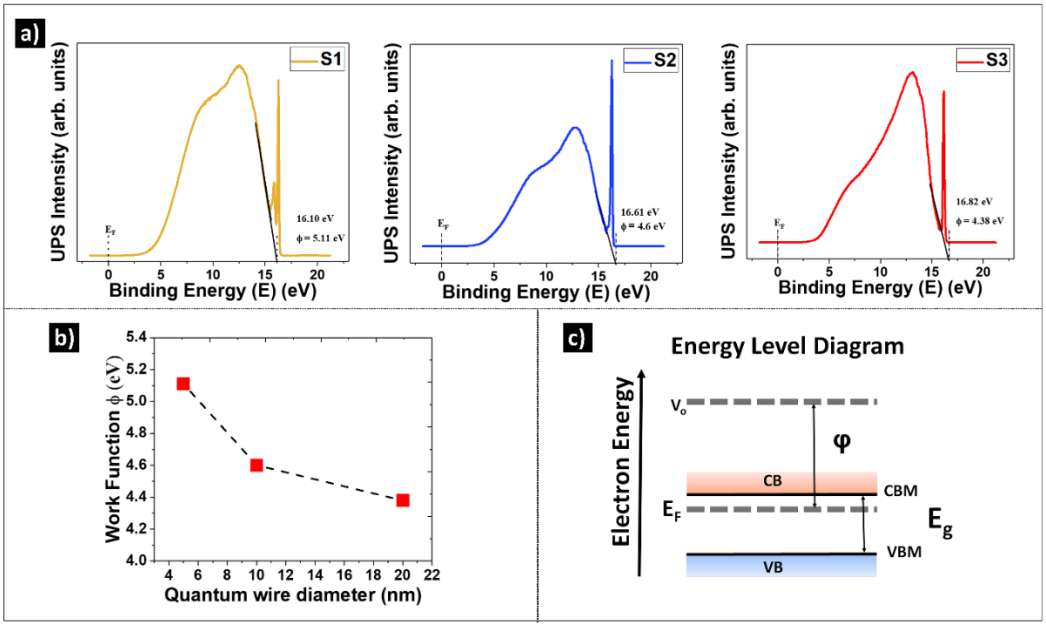

Figure 5.6. (a) UPS spectra with the high binding energy cut off of quantum wire samples S1 (5 nm), S2 (10 nm) and S3 (20 nm) used to determine the work function. (b) Dependence of work function on quantum wire diameter. (c) Energy band diagram showing the relationship between conduction band, valence band, work function, Fermi energy level and energy bandgap for a semiconductor material.

The work function of the quantum wires can be retrieved from the UPS spectra. Figure 5.6 (a), (b) and (c) show the UPS spectra of samples S1, S2 and S3 respectively. The work function can be calculated by finding the difference between the higher energy (secondary electron) cut off value obtained from UPS spectrum and the energy of the UV photons (21.21 eV for He I radiation):

$$Work\ function(\Phi) = h\nu - (E_{cut\text{-}off} - E_F) \qquad (3)$$

where hν is the energy corresponding to the He I source (21.21 eV), $E_{cut\text{-}off}$ is the cut-off of the tail at the higher binding energy end of the UPS spectrum and E_F is the Fermi energy level, located at 0 eV. Figure 5.6 (b) shows the plot with the work function corresponding to each diameter calculated in this manner. The work function increases

as a function of decreasing quantum wire diameter and can be related to the lattice distortions leading to relatively high number of dangling bonds.

5.4 Bandgap properties of quantum wires

Considering both the valence band narrowing effect observed from Figure 5.5 (b) and the work function increase observed in Figure 5.6 (b) as a function of decreasing quantum wire diameter, and the energy level diagram given in Figure 5.6 (c), it is clear that the bandgap energy increases as the quantum wire decreases in size. The bandgap energy shift to higher energies can be understood taking into consideration both the quantum confinement effect and lattice distortion effects. While quantum confinement is easily understood and could be experimentally observed by photoluminescence studies, lattice distortion needs surface sensitive experiments like the XPS and UPS. While they can be successfully used to measure the lattice strain and corresponding lattice stress experimentally from GaAs quantum wires, our PL studies on un-passivated GaAs quantum wires did not yield any results even for low temperature measurements. This is unsurprising given the material volume and more importantly the very high surface recombination velocities of GaAs material.[19]

It is now understood from the above discussions that the increase in surface-to-volume ratio of decreasing quantum wire size along with the lattice strain effects can be used to explain the bandgap expansion in quantum wires. The theory of quantum confinement also agrees to our qualitative understanding of the bandgap energy. According to quantum confinement theory, bandgap expansion is caused due to the energy of freely moving carriers. The confinement of both the electrons and holes in the conduction band and the valence band, respectively, cause an increase in the lowest energy optical transition from valence to conduction band, effectively increasing the bandgap. The experimental determination of the bandgap energy would require effective passivation

techniques. The widely reported passivation layer used for GaAs NWs is AlGaAs. Despite the best efforts to grow an effective passivation layer, AlGaAs growth over ultra thin GaAs quantum wires were not successful as high growth temperatures (typically >650°C) resulted in etch down of quantum wires. We attempt to understand the optical transition energies as a function of decreasing quantum wire diameter using Next Nano simulations. Figure 5.7 (a) shows a schematic of a typical free standing GaAs quantum wire and AlGaAs passivated GaAs quantum wires on synthetic mica.

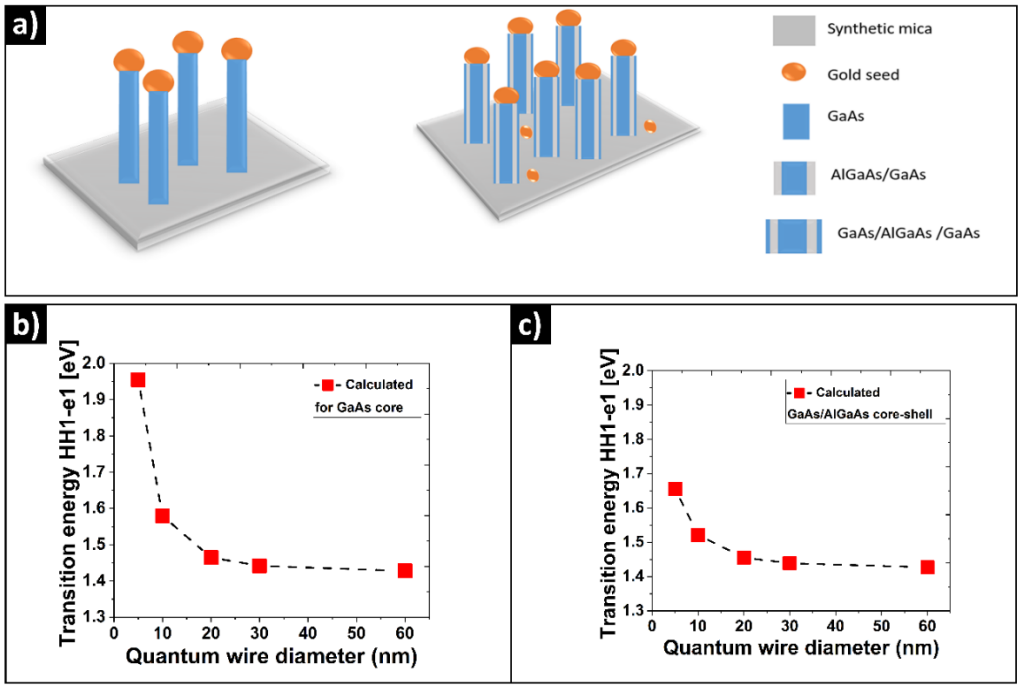

Figure 5.7. (a) Schematic of VLS grown GaAs quantum wires on synthetic mica without and with AlGaAs passivation. (b) Calculated lowest optical transition energy for free standing GaAs quantum wires (b) without passivation and (c) with AlGaAs passivation.

Figure 5.7 (b) and (c) show the plot of the calculated lowest optical transition energy for free standing GaAs core and AlGaAs passivated quantum wires respectively. Our calculations revealed a significant difference in bandgap energy shift in free-standing GaAs quantum wire in contrast to the AlGaAs passivated GaAs quantum wires.

5.5 Conclusions

GaAs quantum wires of record dimensions down to 5 nm diameter are synthesised via gold-seeded VLS growth technique on synthetic mica using MOCVD. The samples exhibit exceptional crystal morphology including very low tapering and pure zinc blende structure. A direct lattice constant measurements and subsequent lattice strain and stress results show lattice relaxation in GaAs quantum wires. 10 and 20 nm GaAs quantum wires were measured to have an enhanced negative stress in contrast to 5 nm wires. The electronic structure, surface and bandgap properties are explored in detail. Our XPS experimental results indicate that the core-level binding energy shifts to the higher energy along with the valence band narrowing effect as a function of decreasing quantum wire diameter. An increasing work function with decreasing quantum wire diameter is extracted from UPS results. The bandgap energy shifts to higher energies with decreasing quantum wire diameter.

Next Nano simulations were carried out to study the effect of quantum confinement on optical transition energies in both freestanding GaAs quantum wires and GaAs quantum wires passivated with an AlGaAs layer. The simulation results show an enhanced bandgap variation in freestanding quantum wires as opposed to AlGaAs passivated wires. Overall, in this chapter we have systematically studied various physical properties as a function of GaAs quantum wires of dimensions below the exciton Bohr radius. This study has laid the foundation for experimental growth and characterisation of ultra-thin III-V NWs.

5.6 References:

(1) Heyn, C.; Strelow, C.; Hansen, W. Excitonic Lifetimes in Single GaAs Quantum Dots Fabricated by Local Droplet Etching. *New J. Phys.* **2012**, *14*. https://doi.org/10.1088/1367-2630/14/5/053004.

(2) Loitsch, B.; Rudolph, D.; Morkötter, S.; Döblinger, M.; Grimaldi, G.; Hanschke, L.; Matich, S.; Parzinger, E.; Wurstbauer, U.; Abstreiter, G.; Finley, J. J.; Koblmüller, G. Tunable Quantum Confinement in Ultrathin, Optically Active Semiconductor Nanowires Via Reverse-Reaction Growth. *Adv. Mater.* **2015**, *27* (13), 2195–2202. https://doi.org/10.1002/adma.201404900.

(3) Gil, E.; Dubrovskii, V. G.; Avit, G.; André, Y.; Leroux, C.; Lekhal, K.; Grecenkov, J.; Trassoudaine, A.; Castelluci, D.; Monier, G.; Ramdani, R. M.; Robert-Goumet, C.; Bideux, L.; Harmand, J. C.; Glas, F. Record Pure Zinc blende Phase in GaAs Nanowires down to 5 Nm in Radius. *Nano Lett.* **2014**, *14* (7), 3938–3944. https://doi.org/10.1021/nl501239h.

(4) Saraswathy Vilasam, A. G.; Prasanna, P. K.; Yuan, X.; Azimi, Z.; Kremer, F.; Jagadish, C.; Chakraborty, S.; Tan, H. H. Epitaxial Growth of GaAs Nanowires on Synthetic Mica by Metal–Organic Chemical Vapor Deposition. *ACS Appl. Mater. Interfaces* **2022**, *14* (2), 3395–3403. https://doi.org/10.1021/acsami.1c19236.

(5) Glas, F.; Harmand, J. C.; Patriarche, G. Why Does Wurtzite Form in Nanowires of III-V Zinc Blende Semiconductors? *Phys. Rev. Lett.* **2007**, *99* (14), 3–6. https://doi.org/10.1103/PhysRevLett.99.146101.

(6) Akiyama, T.; Sano, K.; Nakamura, K.; Ito, T. An Empirical Potential Approach to Wurtzite-Zinc blende Polytypism in Group III-V Semiconductor Nanowires. *Japanese J. Appl. Physics, Part 2 Lett.* **2006**, *45* (8–11). https://doi.org/10.1143/JJAP.45.L275.

(7) Dhaka, V.; Haggren, T.; Jussila, H.; Jiang, H.; Kauppinen, E.; Huhtio, T.; Sopanen, M.; Lipsanen, H. High Quality GaAs Nanowires Grown on Glass Substrates. *Nano Lett.* **2012**, *12* (4), 1912–1918. https://doi.org/10.1021/nl204314z.

(8) Rurali, R. Colloquium: Structural, Electronic, and Transport Properties of Silicon

Nanowires. *Rev. Mod. Phys.* **2010**, *82* (1), 427–449. https://doi.org/10.1103/RevModPhys.82.427.

(9) Ma, D. D. D.; Lee, C. S.; Au, F. C. K.; Tong, S. Y.; Lee, S. T. Small-Diameter Silicon. **2003**, *299* (March), 1874–1878.

(10) Akiyama, H. One-Dimensional Excitons in GaAs Quantum Wires. *J. Phys. Condens. Matter* **1998**, *10* (14), 3095–3139. https://doi.org/10.1088/0953-8984/10/14/004.

(11) Franceschetti, A.; Zunger, A. Free-Standing versus AlAs-Embedded GaAs Quantum Dots, Wires, and Films: The Emergence of a Zero-Confinement State. *Appl. Phys. Lett.* **1996**, *68* (24), 3455–3457. https://doi.org/10.1063/1.115791.

(12) Sheng, H.; Yin, T.; Xiao, B.; Jiang, X. Modeling the Lattice Expansion and Contraction of Nanocrystals in Different Interface Environments. *J. Nanoparticle Res.* **2022**, *24* (12), 1–9. https://doi.org/10.1007/s11051-022-05634-w.

(13) Jiang, Q.; Liang, L. H.; Zhao, D. S. Lattice Contraction and Surface Stress of Fcc Nanocrystals. *J. Phys. Chem. B* **2001**, *105* (27), 6275–6277. https://doi.org/10.1021/jp010995n.

(14) Leontyev, I. N.; Kuriganova, A. B.; Leontyev, N. G.; Hennet, L.; Rakhmatullin, A.; Smirnova, N. V.; Dmitriev, V. Size Dependence of the Lattice Parameters of Carbon Supported Platinum Nanoparticles: X-Ray Diffraction Analysis and Theoretical Considerations. *RSC Adv.* **2014**, *4* (68), 35959–35965. https://doi.org/10.1039/c4ra04809a.

(15) Aruna, I.; Mehta, B. R.; Malhotra, L. K.; Shivaprasad, S. M. Size Dependence of Core and Valence Binding Energies in Pd Nanoparticles: Interplay of Quantum Confinement and Coordination Reduction. *J. Appl. Phys.* **2008**, *104* (6).

https://doi.org/10.1063/1.2973682.

(16) Zhang, J. Y.; Wang, X. Y.; Xiao, M.; Qu, L.; Peng, X. Lattice Contraction in Free-Standing CdSe Nanocrystals. *Appl. Phys. Lett.* **2002**, *81* (11), 2076–2078. https://doi.org/10.1063/1.1507613.

(17) Tsunekawa, S.; Ishikawa, K.; Li, Z. Q.; Kawazoe, Y.; Kasuya, A. Origin of Anomalous Lattice Expansion in Oxide Nanoparticles. *Phys. Rev. Lett.* **2000**, *85* (16), 3440–3443. https://doi.org/10.1103/PhysRevLett.85.3440.

(18) Sun, C. Q.; Tay, B. K.; Zeng, X. T.; Li, S.; Chen, T. P.; Zhou, J.; Bai, H. L.; Jiang, E. Y. Bond-Order-Bond-Length-Bond-Strength (Bond-OLS) Correlation Mechanism for the Shape-and-Size Dependence of a Nanosolid. *J. Phys. Condens. Matter* **2002**, *14* (34), 7781–7795. https://doi.org/10.1088/0953-8984/14/34/301.

(19) Joyce, H. J.; Docherty, C. J.; Gao, Q.; Tan, H. H.; Jagadish, C.; Lloyd-Hughes, J.; Herz, L. M.; Johnston, M. B. Electronic Properties of GaAs, InAs and InP Nanowires Studied by Terahertz Spectroscopy. *Nanotechnology* **2013**, *24* (21). https://doi.org/10.1088/0957-4484/24/21/214006.

Chapter 6

Large-area epitaxial growth of InAs nanowires and thin films on hexagonal boron nitride

6.1 Introduction

Despite the increasing interest in the field of III-V NW and thin film growth on 2D substrates, there is limited research literature available on this topic. This chapter presents a novel approach for the catalyst-free growth of InAs NWs and thin films on few-layer hexagonal boron nitride (h-BN) transferred onto SiO_2/Si substrates.

Through systematic investigation of various growth conditions, this chapter demonstrates the possibility of achieving a high yield of vertically oriented NWs and uniform thin films growth on the h-BN surface. This finding represents a significant step towards realising the high-density growth of III-V NWs and paves a way to realise single-crystalline III-V thin films on 2D materials.

This study sets the groundwork for future research on advanced heterostructures and devices based on III-V semiconductors grown on 2D materials. The materials used in this study are summarised in Section 6.2 (6.2.1 and 6.2.2). Section 6.3 explains the growth procedure used to produce NWs and thin films with section 6.3.1 describing the experimental details of the growth of InAs NWs. The effect of growth parameters on NW morphology and vertical yield are discussed in sections 6.3.2 and 6.3.3, respectively. The crystal structure of NWs grown under different growth conditions is discussed in Section 6.5. Section 6.6 covers the detailed growth of InAs thin films on h-BN surfaces, while Section 6.7 explores the crystal structure and strain properties of the thin films. Optical characterizations and the effect of passivation are discussed in Section 6.8, and Section

6.9 covers the electrical characterisation of the thin film. Finally, Section 6.10 concludes the chapter and summarises the main findings of the study.

6.2. Materials

6.2.1 Hexagonal Boron Nitride (h-BN)

h-BN is a 2D layered material that shares a similar crystal structure and lattice parameter to graphene. However, h-BN exhibits distinct physical properties, such as band structure, optical properties and electrical characteristics. Recent studies have demonstrated that high-quality III-nitrides can be grown on h-BN substrates with exceptional crystalline quality. [1]The unique layered structure of van der Waals substrates permits the facile peel-off of as-grown micro- and nanostructures as well as thin films.

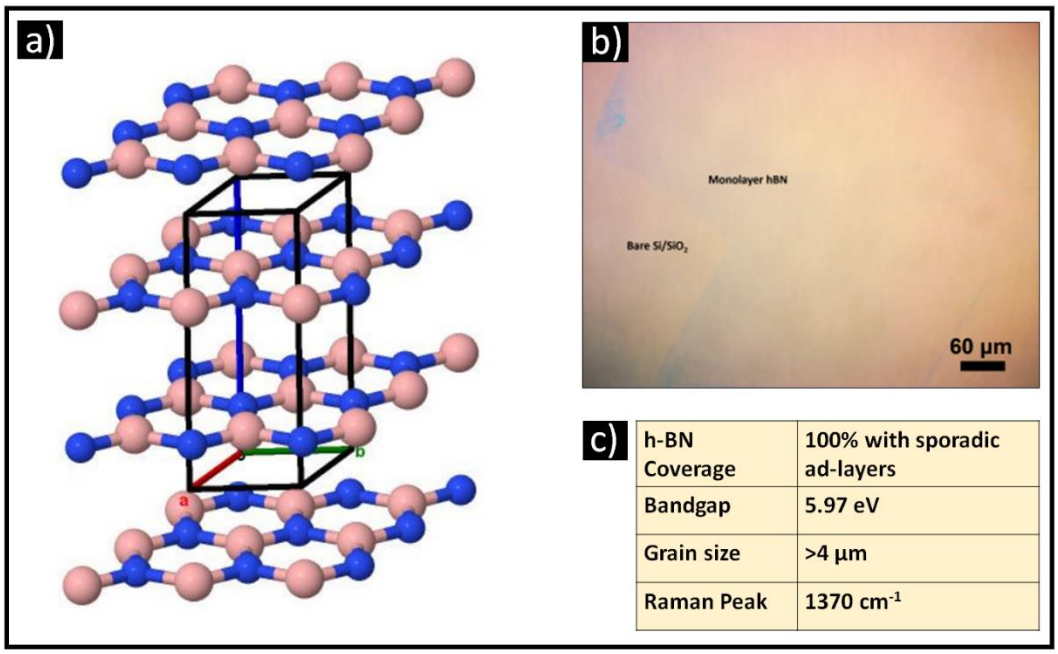

Figure 6.1 (a) Ball and stick model of h-BN crystal structure. (b) Optical microscope image of the monolayer h-BN transferred on SiO_2/Si substrate. (c) Key properties of h-BN (adopted from Grolltex company data sheet).

Crystal Structure: h-BN has a hexagonal crystal structure with a lattice constant of 2.5 Å. The boron and nitrogen atoms are arranged in a honeycomb lattice as shown in Figure 6.1 (a). The optical microscope image and the h-BN layer properties provided by the supplier are shown in figure 6.1 (b) and (c), respectively. Each boron atom bonded to three nitrogen atoms and each nitrogen atom bonded to three boron atoms. The crystal structure of h-BN is highly symmetrical, resulting in its high mechanical strength and chemical stability. [2]

Physical Properties: h-BN has excellent thermal conductivity (~ 600 W/(m·K)) and electrical insulation properties (~6 eV wide bandgap). It also exhibits high thermal stability (1000 °C in air, and 1400 °C in vacuum) with excellent chemical and oxidation resistance. [34] This unique combination of properties makes h-BN an attractive material for next generation high-temperature electronic and thermal management applications.

Mechanical Properties: h-BN is a highly robust material with excellent mechanical properties, such as high strength, stiffness, and toughness. The Young's modulus of monolayer h-BN is 0.865±0.073 TPa and has a fracture strength of 70.5±5.5 GPa.[5]

6.2.2 InAs

InAs is a III-V semiconductor material that has attracted a lot of attention due to its unique electrical, optical and mechanical properties. InAs can be synthesised using a variety of methods, including molecular beam epitaxy (MBE), metal-organic chemical vapor deposition (MOCVD) and chemical vapor deposition (CVD). MOCVD and CVD are suitable for large-scale production of InAs thin films and NWs but may require additional processing steps to achieve high quality.

InAs is a narrow-gap compound semiconductor (direct bandgap of 0.36 eV at room temperature) with a ZB crystal structure in bulk and a lattice constant of 6.058 Å. It has

a high electron mobility as high as 13,000 cm^2/Vs at room temperature.[6] This study attempts to grow InAs NWs and thin films with excellent optoelectronic properties.

6.3 Catalyst-free growth of InAs NWs and thin films

In this study, catalyst-free growth of InAs NWs and thin films on large-area few-layer h-BN on SiO_2/Si substrates was conducted in the horizontal-flow MOCVD reactor using trimethylindium (TMIn) and AsH_3 as the group III and group V precursors, respectively, with hydrogen as the carrier gas.

6.3.1 Experimental details:

The MOCVD reactor was first pumped down to a pressure of 100 mbar. To grow NWs and thin films, the reactor was heated to the desired growth temperature in a hydrogen atmosphere before introducing TMIn and AsH_3 to initiate growth. NW growth was carried out for 15 minutes, after which the reactor was allowed to cool under ambient AsH_3 until the temperature dropped below 350 °C. The effects of growth temperature (450-600°C) and V/III ratio (3-40) on NW density, length and diameter were investigated. The V/III ratio for NW growth was varied by keeping the group III flow rate at 6.206×10^{-6} mol/min and changing the group V flow rate correspondingly.

To achieve uniform thin film growth, the influence of both growth temperature and V/III ratio was also studied. Experiments to study the effect of V/III ratio on thin films growth were carried out to obtain maximum areal coverage of smooth thin films. This was done by varying the group V flow between 4.464×10^{-4} and 6.696×10^{-3} mol/min while keeping the group III flow rate constant at 1.241×10^{-5} mol/min (V/III ratio in the range of 40-540), and then by varying the group III flow rate between 5.820×10^{-5} and 1.241×10^{-5} mol/min while keeping the group V flow rate constant at 2.500×10^{-3} mol/min (V/III ratio in the range of 40-200).

Morphological and structural characterisations of the NWs and thin films were carried out using scanning electron microscopy (SEM, FEI Verios 460L), atomic force microscopy (Bruker ICON AFM) and transmission electron microscopy (TEM, JEOL JEM-2100F). Optical characterisations were carried out by infrared reflectance and photoluminescence (PL) measurements. Infrared reflectance was performed using a Fourier-transform infrared (FTIR) spectrometer (Frontier, Perkin Elmer) coupled with a microscope under ambient environment. A liquid nitrogen-cooled HgCdTe detector was used with a Cassegrain objective lens. Measurements were carried out over a 100×100 μm^2 area using a variable aperture. The spectra were acquired at a resolution of 4 cm^{-1} and referenced against a reflecting gold surface of the same area.

6.3.2 Effect of Growth temperature

The SEM images in Figure 6.2 (a)-(d) depict NWs grown at different growth temperatures. At a low growth temperature of 450 °C, there is mainly the formation of nanoislands, which suggests that adatom diffusion length on the h-BN surface is low at this growth temperature. As the temperature increases, the NWs grow denser, with the highest density of 2.1×10^9 /cm^2 at 500 °C. This density is an order of magnitude higher than that reported for InAs NWs grown on graphitic substrates using self-catalysed growth strategy. [7] As growth temperature increases further to 600 °C, NW density reduces. The NW morphology also changes with growth temperature. Figures 6.2 (e) and (f) show plots of the length, diameter, and NW density as a function of growth temperature. The length of the NWs is directly proportional and their diameter is inversely proportional to growth temperature. This morphology evolution is due to the competition between axial and radial growth. With increased growth temperature, the axial growth rate increases at the expense of the radial growth rate because the adatom diffusion length is enhanced, allowing migration to the top of the NWs. The non-tapered

NW morphology supports this explanation. Therefore, longer NWs with smaller diameters are observed with increasing growth temperature.

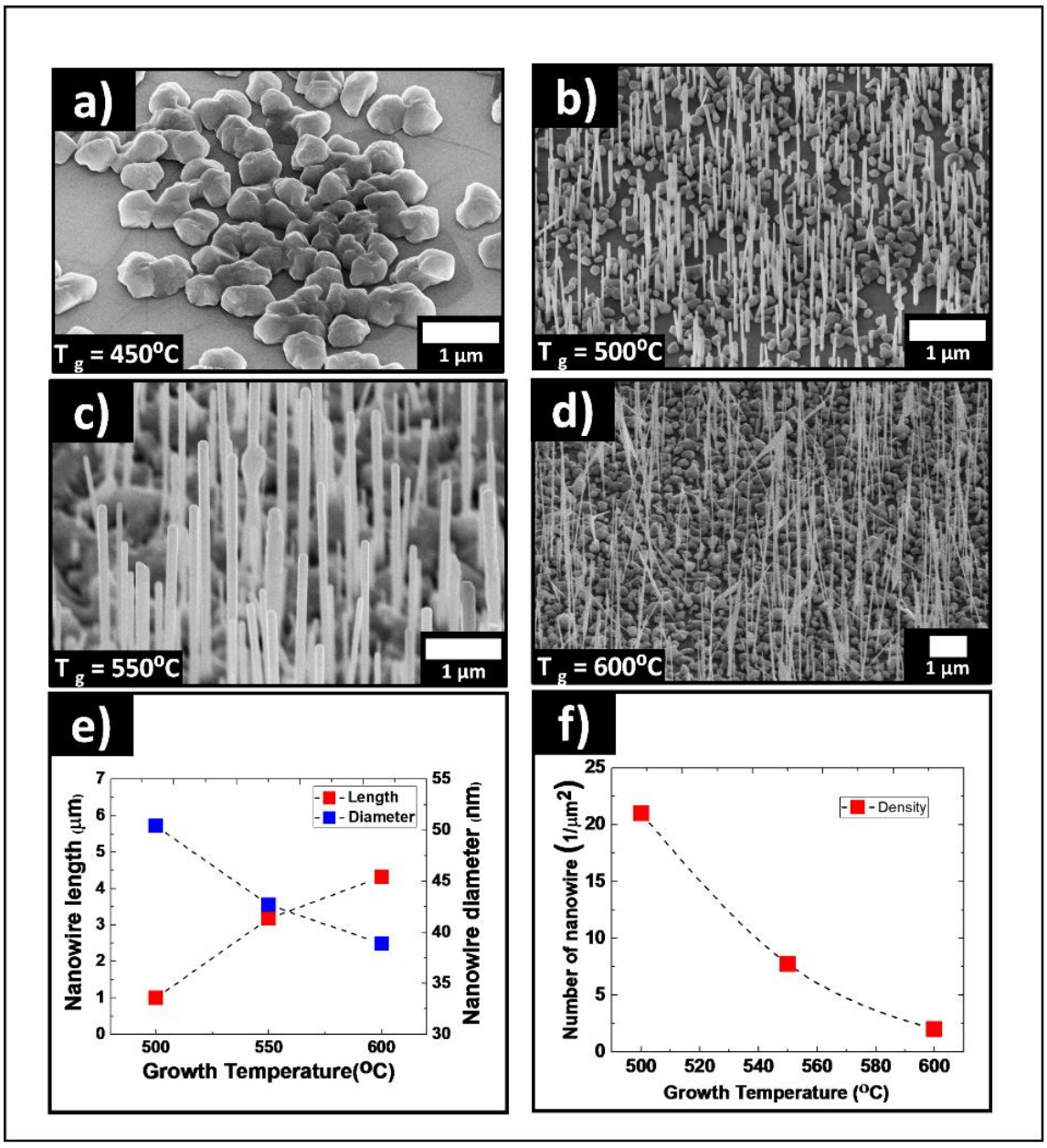

Fig 6.2. SEM images of InAs NWs grown on h-BN/SiO_2/Si at different growth temperatures: (a) 450 ºC, (b) 500 ºC, (c) 550 ºC and (d) 600 ºC. All scale bars are 1 µm. (e) NW length) and diameter as a function of growth temperature. (f) Density of NWs as a function of growth temperature.

The change in NW density is also caused by the same phenomenon. At higher growth temperature, the adatom mobility is high, so fewer adatoms can spontaneously nucleate to form NWs. Therefore, the NW density decreases at higher growth temperature. Additionally, the vertical orientation of InAs NWs grown on h-BN indicates a good epitaxial relationship between them. This relationship is similar to what has been reported for InAs NWs grown on graphene, where the authors suggested that the near-lattice-matching conditions between the InAs NWs and graphene are responsible for the epitaxial relationship.

6.3.3 Effect of V/III ratio

The SEM images in Figure 6.3 (a)-(d) illustrate the effect of V/III ratio on NW morphology at a constant growth temperature of 500 °C. The images correspond to V/III ratios of 3, 5.4, 10 and 40. The plots of NW density, length, and diameter as a function of V/III ratio are shown in Figures 6.3 (e) and (f). The NW density increases from a V/III ratio of 3 to 5 but decreases significantly thereafter. At low V/III ratios, there is less AsH_3 in the growth environment, resulting in less nucleation and fewer NWs. Conversely, at high V/III ratios, the mobility of In adatoms reduces, leading to more spontaneous nucleation on the h-BN surface. This results in the coalescence of nuclei, rather than NW formation, which reduces NW density. It is known that the activation energy for the heterogeneous reaction at the growth interface decreases with increased V/III ratio. The observed reduction in NW length and the considerable increase in NW diameter with V/III ratio is due to competition between radial and axial growth. This competition stems from reduced In adatom mobility at higher V/III ratios, leading to more prominent deposition on the NW sidewalls than at its tip. Consequently, NW coalescence occurs and nanoislands form on the h-BN surface during growth, as shown in Figure 6.3 (d).

This observation is interesting because further increasing the V/III ratio can lead to the formation of an InAs thin films on h-BN, which is explored later in this chapter.

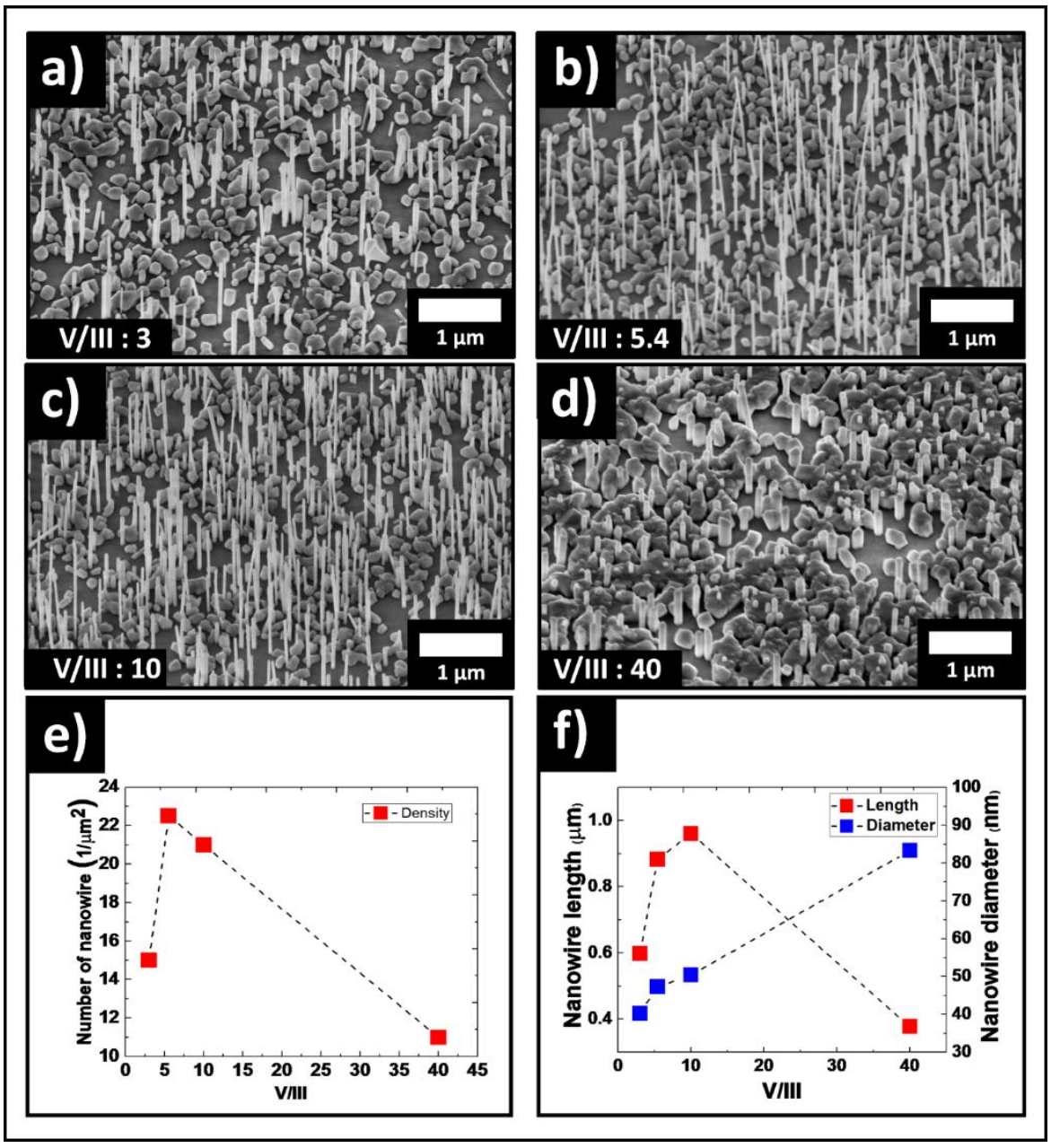

Fig 6.3 SEM images of InAs NWs grown on h-BN/SiO_2/Si with different V/III ratios: (a) 3, (b) 5.4, (c) 10 and (d) 40. All scale bars are 1 µm. (e) NW density as a function of V/III ratio. (f) NW length and diameter as a function of V/III ratio.

6.4 Crystal structure of NWs

The crystal structure of NWs grown at various growth temperatures and V/III ratios is studied using a high-resolution TEM. The crystal structure of NWs grown at 500, 550 and 600 °C at a V/III ratio of 10 is depicted in figures 6.4 (a)-(c), while figure 6.4 (d)-(f) show the crystal phase of the NWs as a function of V/III ratio at a constant growth temperature of 500 °C.

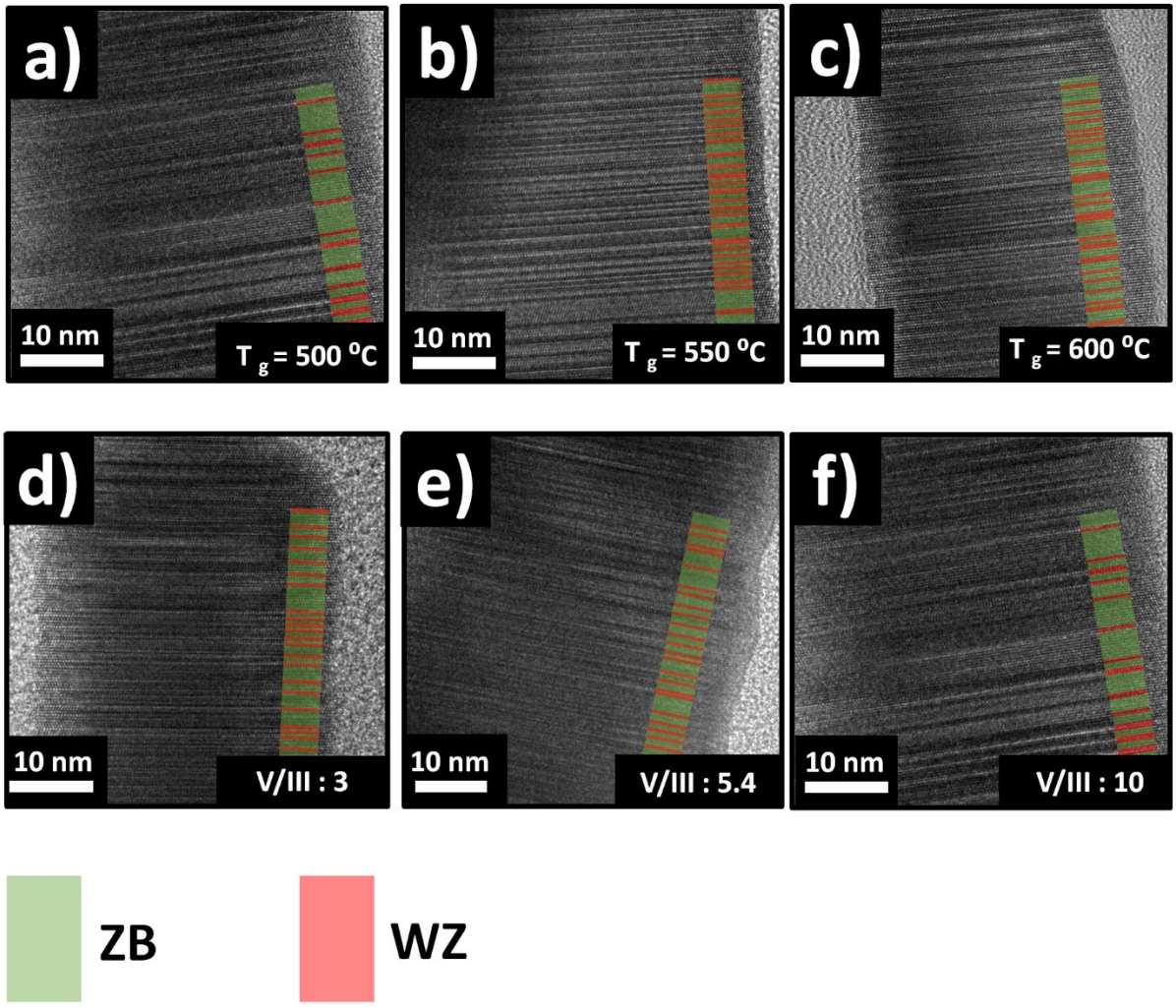

Figure 6.4. HRTEM images of NWs grown at different growth temperatures and V/III ratios. (a)-(c) Crystal structure of NWs grown at 500, 550 and 600 °C at a V/III ratio of 10. (d)-(f) Crystal phase of NWs grown at V/III ratio of 3, 5.4 and 10 at a fixed growth temperature of 500 °C. ZB and WZ phase are marked in green and red, respectively.

It is found that the grown InAs NWs are predominantly <111> oriented and had a mostly zinc blende (ZB) phase with rotational twins and stacking faults. The growth condition with the highest yield of NWs results in up to 20 monolayers of ZB segments with occasional rotational twins. This is an improvement compared to just 10 monolayers of ZB along with rotational twins when InAs NWs are grown on single-layer graphene.

The observed defective crystal structure suggests that the crystal structure of the NWs is mostly independent of the growth kinetics. This is consistent with literature reports on catalyst-free growth of InAs and InGaAs NWs on graphene and silicon substrates using catalyst-free growth methods. However, the catalyst-free heteroepitaxial growth of InAs and InGaAs NWs on substrates demonstrated a high density of defects in the as-grown NWs.[8,9,10]

III-V NWs tend to nucleate as ZB or WZ phases and grow along the <111>B direction for energetic reasons. Energy calculations carried out by Akiyama *et al* identified the origin of polytypism using empirical potential. The relative stability of WZ and ZB NWs is determined by the energy difference $\Delta E_{WZ\text{-}ZB} = E_{WZ} - E_{ZB}$, where E_{WZ} and E_{ZB} are the system energies of WZ and ZB NWs, respectively.[11] The energy calculations showed that the crystal structure of NWs with large diameters acted like that of bulk material, as the $\Delta E_{WZ\text{-}ZB}$ converged to ΔE_{Bulk} as the diameter increased. The contributions of electrostatic energy interaction due to valence-bond and ionic charges in the bulk form, along with the two- and three-coordinated atoms on the nanowire facets, determine the stability of ZB and WZ structures in NWs.

The calculations also explain the role of iconicity in determining bistability, where both ZB and WZ structures can form in NWs. For example, $\Delta E_{WZ\text{-}ZB}$ of arsenide and

antimonide NWs being smaller than the ΔE_{Bulk} indicates that the WZ structure can easily be incorporated in the stable ZB NWs.

Some studies have investigated the impact of surfactants on the crystal structure of NWs For example, researchers using MBE found that adding a bismuth flux to the growth process increased the proportion of WZ phase in the resulting NWs.[12] This is because the Bi acts as a wetting agent that affects the surface energy of the NWs to promote the growth of WZ crystal structure.

Other researchers have demonstrated the growth of defect-free WZ InAs NWs on a Ni-masked Si (111) substrate.[13] Our own work has focused on growing InGaAs NWs without a catalyst on a GaAs (111) substrate using SAE. By controlling the Ga composition during growth, we are able to tune the crystal structure from predominantly WZ to predominantly ZB phase.[14]

However, further research is needed to explore the possibility of tuning the crystal structure of NWs grown using catalyst-free methods on vdW substrates. These substrates are characterised by weak intermolecular interactions, which can complicate the growth process and affect the resulting crystal structure.

6.5 InAs thin films on h-BN/SiO_2/Si

The growth of III-V semiconductor thin films on 2D material templates typically involves modifying the vdW surface through etching techniques to create nucleation sites. A recent review of developments in vdW epitaxy of III-V semiconductors on 2D materials describes various surface treatments used to encourage and regulate growth.[15] However, these treatments have been shown to degrade the surface and alter its physical properties. Alaskar et al. were among the first to attempt to grow a continuous thin film of GaAs on graphene using MBE on multilayer graphene layers transferred onto SiO_2/Si substrates.[16]

Their report concludes that the low surface energy of 2D materials, combined with the low adsorption and migration energy of Ga, In, Al, As species on graphitic surface creates significant obstacles to achieving 2D growth of III-As materials on graphene, primarily due to high surface tension. In this section, we investigate how we can leverage the formation of nanoislands (illustrated in Figures 6.2 and 6.3) to produce a uniform InAs thin film on h-BN/SiO_2/Si. We achieve this by studying the growth parameters systematically while maintaining a constant growth temperature. By increasing the V/III ratio, as depicted in Figure 6.5 (a), we observe a significant reduction in the NW aspect ratio, resulting in their coalescence into nanoislands. SEM images shown in Figures 6.5 (b)-(d) demonstrate that a V/III ratio beyond 40 inhibits NW formation while simultaneously increases the size of the nanoislands.

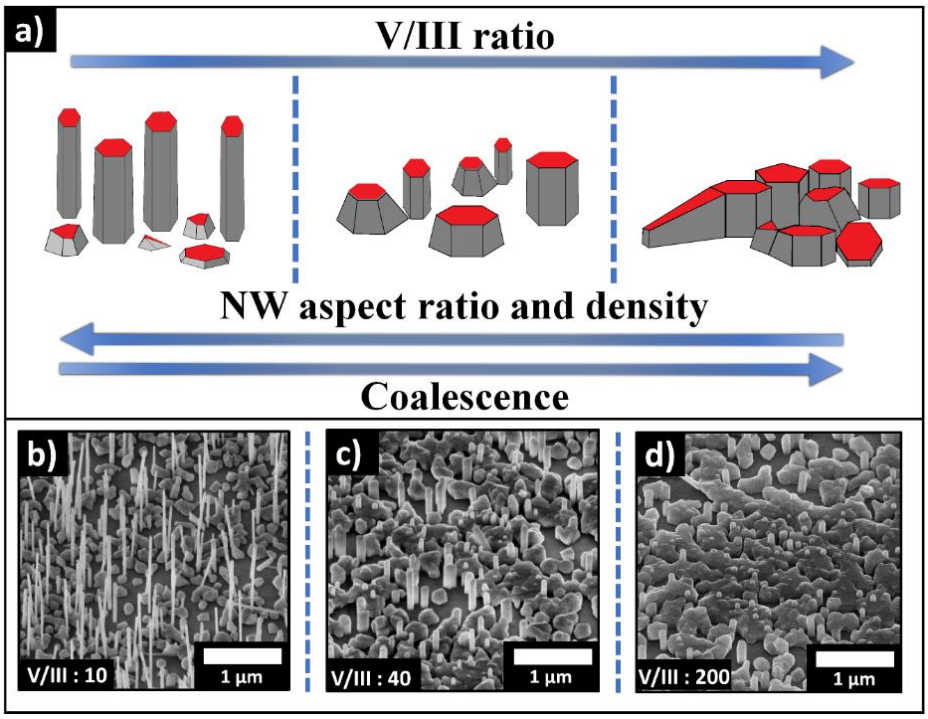

Fig 6.5. (a) Schematic illustrating the conditions for the suppression of NW axial growth and the coalescence of nanoislands. (b-d) 45⁰-tilted SEM images showing the morphology of NWs and nanoislands at different V/III ratios.

Results presented in figure 6.6 reveals that an optimum V/III ratio of 200 and growth temperature of 475 °C lead to a uniformly covered thin film. To maintain the same growth rate across the experiments, group III flow rate was held constant while the group V flow rate was varied. Dayeh *et al.* have demonstrated that the temperature profile of NW growth is heavily influenced by the input V/III ratio due to the fact that a high V/III ratio reduces the activation energy for planar growth and shortens adatom diffusion length.[17] Therefore, it can be concluded that at low growth temperature and relatively high V/III ratio, In adatom mobility is significantly reduced on the h-BN surface, resulting in crystallisation on the substrate surface rather than on the NW growth site.

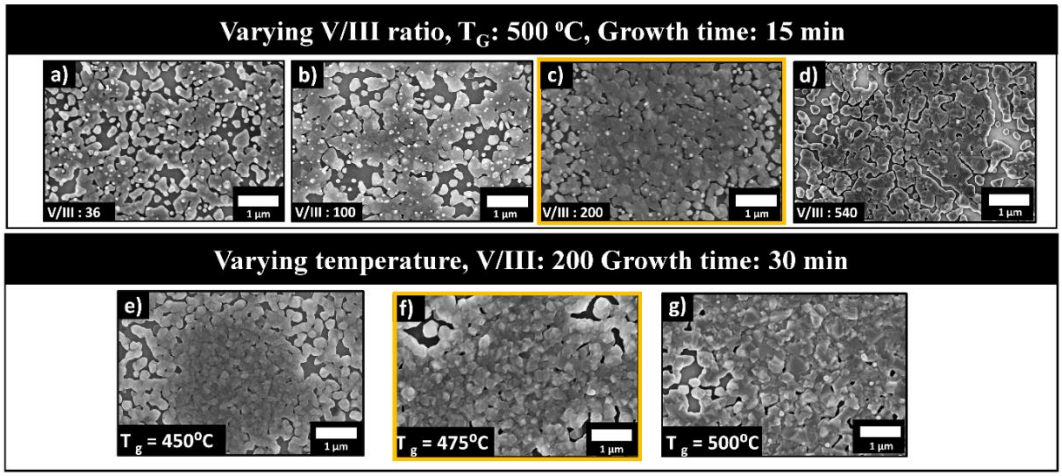

Figure 6.6. (a)-(d) shows the top-view SEM images of morphology evolution of InAs grown at 500 ℃ as a function of increasing V/III ratio of 40, 100, 200 and 540, respectively. Top-view SEM images of thin films grown at V/III ratio 200 and varying temperatures 450, 475and 500 ℃ are shown in (e)-(g), respectively.

The SEM images in figure 6.6 (a)-(d) show the morphology of the InAs thin films grown under different V/III ratios of 40, 100, 200 and 540 respectively. All the samples were grown at 500 ℃ for 15 min. The group III flow rate was kept constant while the group V flow rate was changed as described in the experimental section in the main text. It is

observed that at a V/III ratio of 200, a uniform and smooth morphology is achieved as highlighted with orange box in figure 6.6 (c). However, a further increase in the V/III to 540 roughens the surface and creates large voids in the thin films. It is likely that a high V/III ratio causes a reduction in diffusion length of adatoms hindering efficient coalescence and results in large voids and rough surface morphology of the thin films. To promote coalescence by completely suppressing nanowire growth and improve surface morphology, mainly to avoid large voids and rough surface, further temperature optimisation was carried out, keeping the V/III ratio a constant at 200. The top-view SEM images of the InAs thin films grown for 30 min at 450, 475 and 500 ℃ are shown in figures 6.6 (e) to (g), respectively. At the growth temperature of 475 ℃, the thin films have a greater areal coverage compared to those grown at 450 ℃ and 500 ℃. Thus, the optimised growth temperature and growth time was then used to achieve complete areal coverage of InAs thin films.

Figure 6.7 (a)-(c) depict the thin films growth at V/III ratios of 74, 100 and 200, respectively. These ratios were achieved by changing the group III flow rate while maintaining a fixed group V flow rate of 2.5×10^{-3} mol/min. The growth temperature was set at 475 ℃ and the growth times were adjusted to compensate for the growth rate variation, with the goal that all samples have the same total amount of group III precursor deposited (3.723×10^{-5} mol).

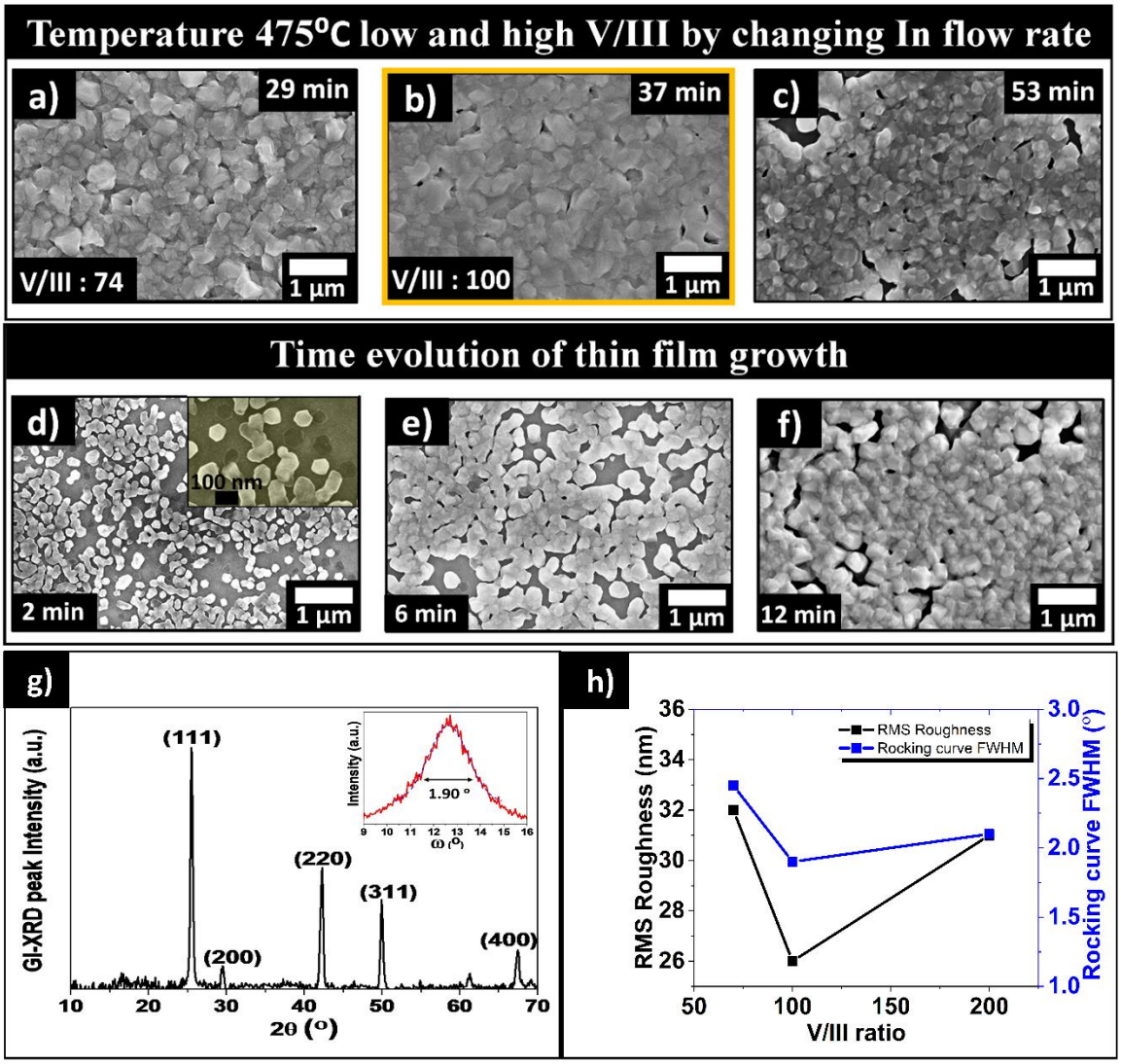

Fig 6.7. Top-view SEM images of the InAs thin films grown with a V/III ratios of (a) 74, (b) 100 (b) and (c) 200. Top-view SEM images showing the time evolution study of the thin films grown at 475 °C with a V/III ratio of 100 for (d) 2, (e) 6, and (f) 12 min. The inset in (d) shows a magnified image of the 2 min sample, clearly showing 2D platelets (layer-by-layer growth) and nano-island nucleation happening simultaneously. The GIXRD spectrum of the sample (a) is shown in (g), with the inset showing the rocking curve of the (111) peak. AFM RMS surface roughness and rocking curve FWHM obtained from the thin films grown with a V/III ratio of 74, 100 and 200 at a growth temperature of 475 °C are shown in (h).

Figure 6.7 (a)-(c) shows that the polycrystalline thin films have a smooth morphology and uniform coverage after growth. In particular, at a V/III ratio of 100, the thin films exhibit a relatively low RMS surface roughness and narrow rocking curve, which is better than other V/III ratios shown in Figure 6.7 (h). Therefore, the growth conditions with low temperature (475 °C) and high V/III ratio (100) shown in Figure 6.7 (b) are ideal for the growth of InAs thin films on h-BN surface.

Investigation of the thin films growth mode of InAs on h-BN surface was conducted from a time evolution study of the best sample obtained. Three growth modes were considered: layer-by-layer growth mode (Frank-Van der Merwe mode), island growth mode (Volmer-Weber mode) and Stranski-Krastanov mode. A layer-by-layer mode occurs when the substrate and the grown thin films are homogeneous materials, resulting in the smallest nuclei extending on the substrate due to weaker interactions between atoms/molecules than their bonding to the growth substrate. In contrast, an island growth mode occurs when the substrate and the thin films are heterogeneous, resulting in stronger bonds between atoms/molecules forming three-dimensional nucleus islands on the substrate. This mode results in a polycrystalline thin film with rough surface morphology. The third growth mode, the Stranski-Krastanov mode, occurs when the thin films initially grows in layer-by-layer mode and then transitions to island growth mode due to the stress generated after the initial layer-by-layer growth.

Figures 6.7 (d)-(f) depict the time evolution study with growth durations of 2, 6, and 12 minutes, respectively. Upon analysing the SEM images of the 2-minute growth sample (with a magnified view in the inset), it becomes evident that 2D hexagonal platelets and islands are formed simultaneously, indicating a coexistence of Volmer-Weber and

Stranski-Krastanov growth modes. However, to achieve a uniform thin film with smooth morphology, a layer-by-layer growth mode is ideal. Although local layer-by-layer nucleation can occur on a vdW surface, it becomes challenging to attain lateral growth above a certain nucleus size, due to the low surface energy and high surface tension properties of the underlying h-BN.

As growth proceeds, the Stranski-Krastanov growth mode starts to dominate over the island growth mode, as illustrated in Figures 6.7 (d)-(f), where nano-island structures merge with 2D platelet structures and other nano-islands.

6.6 Crystal structure and strain properties of the thin films

The cross-sectional TEM image of a focussed ion beam-cut TEM lamella of a thin film grown at 475 ℃ and V/III ratio of 100 is shown in Figure 6.8 (a). The thin films have an average grain size of approximately 0.45 μm with negligible thickness variation. Figures 6.8 (b) and (c) present two such HRTEM images of the thin films, which show the ZB and WZ/twin areas marked in green and red, respectively. From these images, it is evident that the thin films have a predominantly ZB crystal structure, but there are rotational twin defects and WZ areas predominantly in the grain boundaries.

To investigate the local strain at the interface between the thin films and h-BN, geometric phase analysis (GPA) was conducted on a HRTEM image of the interface captured along the [0 -11] zone axis shown in Figure 6.8 (d). GPA was performed in two non-parallel directions, [111] and [-111], to study the in-plane and out-of-plane strain, respectively. The results of the GPA are shown in Figures 6.8 (e) and (f) and indicate that there is no significant interfacial strain between h-BN and InAs. This is an important finding because it suggests that the interface is relatively defect-free.

Finally, Figure 6.8 (g) displays the fast Fourier transform (FFT) of the HRTEM image shown in Figure 6.8 (d). From this FFT, it can be inferred that the direction of InAs thin films growth is along [111]. This information is valuable for understanding the growth mechanism of the InAs thin films and can inform future experiments aimed at optimising their growth conditions.

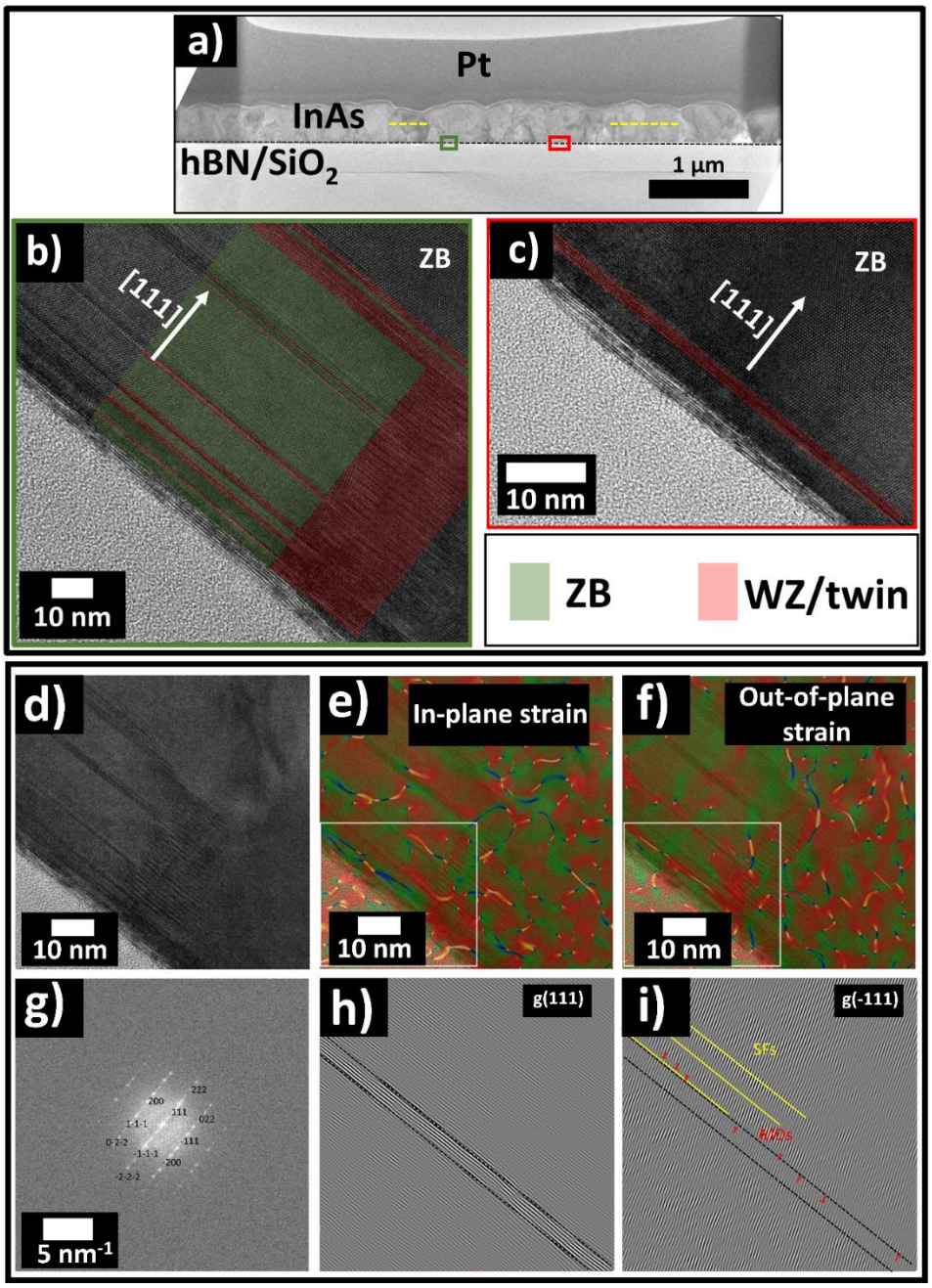

Fig 6.8. (a) FIB-cut TEM lamella of the polycrystalline InAs thin film grown on h-BN/SiO_2/Si substrate. (b)-(c) HRTEM images of InAs/h-BN interface from the areas indicated by the green and red boxes in (a). The ZB and WZ/twin sections are indicated by the colour scheme shown in (c). (d) HRTEM image for GPA strain analysis. (e) In-plane and (f) out-of-plane strain maps overlaid on the HRTEM image. (g) Fast Fourier transform of the HRTEM image in (d). Fast Fourier transform of (h) g(1 1 1) and (i) g(-111).

In order to gain a better understanding of the h-BN/InAs interface and the lack of sharp interfacial strain in GPA, we examined the inverse fast Fourier transform (IFFT) of the HRTEM images presented in Figure 6.8 (h) and (i). The IFFT analyses were performed using the (111) and (-111) diffraction spots shown in Figure 6.8 (g). Our analysis revealed the presence of some dislocations within the InAs layer near the h-BN/InAs interface in the out-of-plane results along the [111] growth direction. However, no dislocations were observed at the h-BN/InAs interface itself.

On the other hand, the in-plane IFFT results of g (-111) show the presence of several misfit dislocations within the h-BN layer and InAs near the interface (Figure 6.8 (i)). Moreover, stacking faults typically found in face-centered cubic crystals on {111} planes due to easy slip are detected and highlighted with yellow lines in Figure 6.8 (i). Our observation of stacking faults both near and away from the interface lead us to conclude that they result from non-optimal growth rather than originating from the h-BN/InAs interface.

Finally, the absence of a sharp interfacial strain in InAs grown on h-BN can be attributed to the presence of misfit dislocations at the h-BN/InAs interface. These dislocations act as an efficient strain relaxation mechanism.

Threading dislocations are defects that can occur in thin films when they are grown on a substrate with a different lattice structure, leading to strain in the film. However, when InAs is grown on a vdW substrate like h-BN, strain-induced dislocations are not expected due to the weak vdW bonding between the two materials. This is in contrast to conventional bulk substrates where strong covalent bonding can lead to the formation of dislocations.

In chapter 4, we described the growth of vertically-oriented GaAs NWs on synthetic mica, another 2D-layered material, and performed DFT calculations to investigate the bonding at the GaAs/mica interface.[18] The results showed that there was negligible charge transfer across the interface, and the lowest energy configuration indicated a physisorption-type bonding, which is also characteristic of vdW bonding. Based on these findings, we expected that threading dislocations would be absent in the InAs thin films grown on the h-BN surface, consistent with what is observed in vdW epitaxy.

6.7 Optical properties of the InAs thin films

Figure 6.9 presents the results of room temperature photoluminescence (PL) and reflectance measurements for the thin film sample grown under optimal conditions (growth temperature of 475 °C and a V/III ratio of 100). The PL emission peak for the sample is observed at 0.39 eV with a FWHM of 69 meV, while the reflectance spectrum shows an absorption peak centered at the same energy. Additionally, the sample displays

high reflectance (over 80%) at other wavelengths, indicating a relatively smooth surface morphology for the thin films.

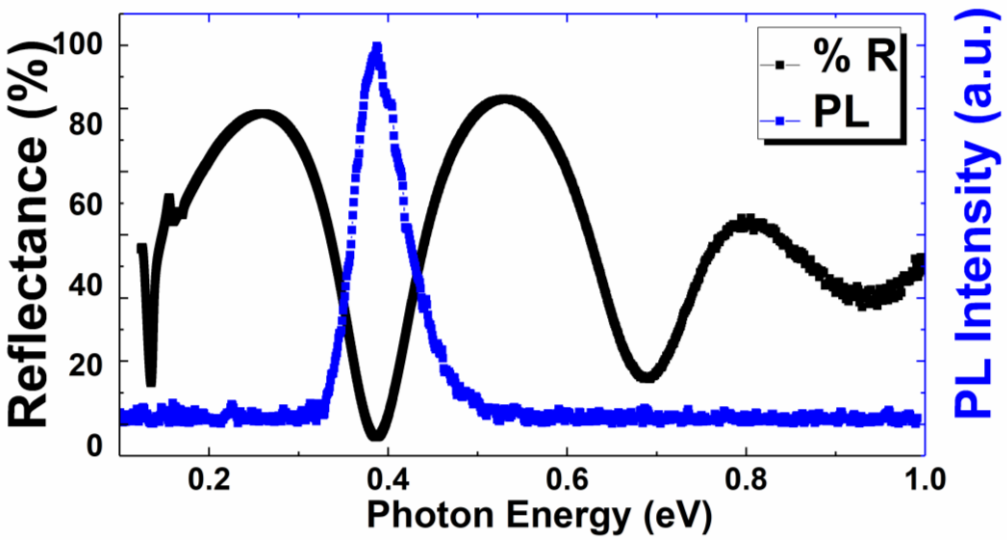

Figure 6.9 Room temperature PL (blue) and reflectance (black) spectra of InAs thin films grown on h-BN

It should be noted that the observed PL emission peak is located near the band edge emission of bulk (ZB) InAs, which has a bandgap energy of E_g = 0.36 eV. The observed redshift (~30 meV) in the PL emission peak, as compared to the bandgap energy of InAs, can primarily be attributed to the strain induced in the epi-layer during cooling after growth.

During heteroepitaxial growth, a biaxial strain is induced between two materials due to their lattice parameter difference. Once the thin films exceed their critical thickness, the biaxial strain is relieved by misfit dislocations, leading to the possibility of unstrained bulk-like material beyond the misfit dislocation region. This observation is supported by the misfit dislocations from the GPA analysis.

However, during the cool-down process from growth temperature, the biaxial strain in the thin films can be re-induced due to the significant difference between the coefficient of thermal expansion of the epi-layer and the substrate.

Previous research has shown that the PL peak of InAs thin films is redshifted when grown on a Si substrate as compared to a GaAs substrate. This redshift is attributed to the heteroepitaxy-induced strain, which causes a 14-19 meV redshift in the InAs PL peak due to the linear thermal expansion coefficient of Si being much lower than that of GaAs.[19]

We propose that the significant difference in linear thermal expansion coefficients between InAs (4.52×10^{-6} $^{o}C^{-1}$) and h-BN (-3.58×10^{-6} $^{o}C^{-1}$; negative values in the direction perpendicular to the plane) leads to a biaxial tensile strain in the InAs layer, causing a PL redshift of approximately 30 meV.

6.8 Effect of passivation

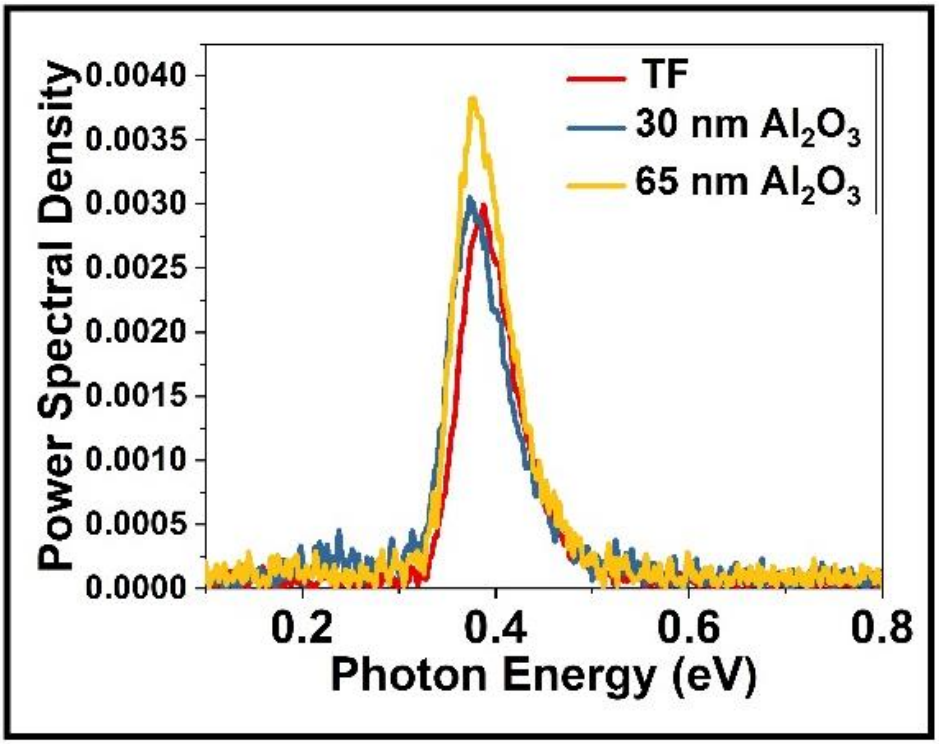

Figure 6.10. Room temperature photoluminescence from InAs thin films passivated a layer of Al_2O_3 with a thickness of 30 and 65 nm.

Surface passivation of InAs NWs and thin films were studied by depositing a layer of Al_2O_3. Such an encapsulation has been demonstrated as an effective method to passivate the surface and enhance radiative and thermal properties.[20] The deposition was done using plasma-enhanced atomic layer deposition (P-ALD: PicoSun - Sunale) at 110 °C. Trimethylaluminium and H_2O were used as the source of aluminium and oxygen, respectively. Different thicknesses (30 and 65 nm) of Al_2O_3 were deposited by tuning the number of ALD pulse and purge cycles. The PL intensity as shown in figure 6.10 is found to increase by 20% for the 65 nm Al_2O_3 passivation compared to the as-deposited thin films.

This strain was further characterised using Raman spectroscopy in backscattering geometry. The difference in the Raman peak position compared to that of unstrained bulk

InAs can help to determine the type of strain present in the film. A blueshift in Raman peak position would indicate compressive strain, while a redshift would indicate tensile strain. The average Raman peak position from at least 10 measurements taken from 10 different points on the as-grown thin films resulted in a peak position of 218.36 cm^{-1}, which is redshifted by 1.33 cm^{-1} compared to unstrained InAs bulk material with a Raman peak at 217.03 cm^{-1} obtained from literature.[20] This redshift in Raman peak position further confirms the presence of residual tensile strain in the thin films.

6.9 Electrical properties

6.9.1 van der Pauw Hall measurements

The electrical properties of the polycrystalline InAs thin films were determined using a van der Pauw Hall measurement system at room temperature. The thin films show an n-type behaviour with a resistivity of 1.62×10^{-4} Ohm-cm, a Hall mobility of 399 $cm^2/(Vs)$ and a carrier density of 9.51×10^{19} $/cm^3$. While pure InAs bulk material exhibits very high room temperature carrier mobility (13,000 $cm^2/(Vs)$), polycrystalline III-V Thin films reported in the literature exhibit carrier mobilities in the range of 100-150 $cm^2/(Vs)$.[21] As per the Matthiesen rule, major factors affecting carrier mobility in a polycrystalline thin film sample are phonon scattering, Coulomb interaction and surface roughness.[21] (what about grain boundary scattering. Generally grain boundary scattering is dominant in polycrystalline thin films) The InAs thin films presented in this work have better electrical characteristics compared to those typically grown at low temperatures (<500 °C) on amorphous substrates reported in literature.[22] We attribute this relative superiority to the greater areal coverage, low surface roughness and a higher average grain size of InAs thin films grown on h-BN surface. Thus, the thin films presented in this work serves as an excellent template for subsequent growth of other III-V layers.

6.10 Conclusions

InAs NWs and thin films are successfully grown on h-BN/SiO_2/Si vdW substrates without employing any catalyst or surface modification techniques. A very high density of NWs ($2x10^9$ /cm^2) is achieved by varying the growth temperature and V/III ratio. The NWs are found to have a mixed WZ/ZB phase across the range of growth parameters studied. A growth strategy to achieve uniform InAs Thin films on h-BN/SiO_2/Si by supressing the NW growth and increasing the radial growth of the nano-islands nucleated on the h-BN surface is reported. The effect of growth parameters, such as temperature and V/III ratio, on the surface morphology, structural and optical properties of InAs thin film are investigated. It is found that the structural properties of the InAs thin films are mostly affected by the temperature and not the V/III ratio. Cross-sectional TEM, which is supported by the XRD and GPA results, reveals a largely [111] oriented ZB structure. The redshift in PL is attributed to the tensile strain induced by the difference in thermal expansion coefficient between h-BN and InAs thin films. The vdW nature of the interface is further evident from the lack of threading dislocations extending to the top of the film. The uniform coverage of the polycrystalline InAs thin films combined with its room temperature PL and a relatively high Hall mobility of 399 cm^2/(Vs) indicate that this technique can be used to achieve large-area, low-temperature growth of III-V thin films directly on van der Waals substrate using MOCVD.

6.11 References:

(1) Sundaram, S.; Vuong, P.; Mballo, A.; Ayari, T.; Karrakchou, S.; Patriarche, G.; Voss, P. L.; Salvestrini, J. P.; Ougazzaden, A. MOCVD of GaN-Based Mixed Dimensional Heterostructures on Wafer-Scale Layered 2D Hexagonal Boron Nitride - A Key Enabler of III-Nitride Flexible Optoelectronics. *APL Mater.* **2021**, *9* (6).

https://doi.org/10.1063/5.0049306. article no.

(2) Pease, R. S. Crystal Structure of Boron Nitride. *Nature* **1950**, *165* (4201), 722–723. https://doi.org/10.1038/165722b0.

(3) Wang, Y.; Xu, L.; Yang, Z.; Xie, H.; Jiang, P.; Dai, J.; Luo, W.; Yao, Y.; Hitz, E.; Yang, R.; Yang, B.; Hu, L. High Temperature Thermal Management with Boron Nitride Nanosheets. *Nanoscale* **2018**, *10* (1), 167–173. https://doi.org/10.1039/c7nr07058f.

(4) Lin, Z.; Mcnamara, A.; Liu, Y.; Moon, K. sik; Wong, C. P. Exfoliated Hexagonal Boron Nitride-Based Polymer Nanocomposite with Enhanced Thermal Conductivity for Electronic Encapsulation. *Compos. Sci. Technol.* **2014**, *90*, 123–128. https://doi.org/10.1016/j.compscitech.2013.10.018.

(5) Falin, A.; Cai, Q.; Santos, E. J. G.; Scullion, D.; Qian, D.; Zhang, R.; Yang, Z.; Huang, S.; Watanabe, K.; Taniguchi, T.; Barnett, M. R.; Chen, Y.; Ruoff, R. S.; Li, L. H. Mechanical Properties of Atomically Thin Boron Nitride and the Role of Interlayer Interactions. *Nat. Commun.* **2017**, *8*, 15815. https://doi.org/10.1038/ncomms15815.

(6) Del Alamo, J. A. Nanometre-Scale Electronics with III-V Compound Semiconductors. *Nature* **2011**, *479* (7373), 317–323. https://doi.org/10.1038/nature10677.

(7) Hong, Y. J.; Lee, W. H.; Wu, Y.; Ruoff, R. S.; Fukui, T. Van Der Waals Epitaxy of InAs NWs Vertically Aligned on Single-Layer Graphene. *Nano Lett.* **2012**. 12, 3, 1431–1436. https://doi.org/10.1021/nl204109t.

(8) Hong, Y. J.; Lee, W. H.; Wu, Y.; Ruoff, R. S.; Fukui, T. Van Der Waals Epitaxy of InAs NWs Vertically Aligned on Single-Layer Graphene. *Nano Lett.* **2012**, *12* (3), 1431–1436. https://doi.org/10.1021/nl204109t.

(9) Mohseni, P. K.; Behnam, A.; Wood, J. D.; English, C. D.; Lyding, J. W.; Pop, E.; Li, X. InxGa1-Xas Nanowire Growth on Graphene: Van Der Waals Epitaxy Induced Phase Segregation. *Nano Lett.* **2013**. 13, 3, 1153–1161. https://doi.org/10.1021/nl304569d.

(10) Anyebe, E. A.; Sandall, I.; Jin, Z. M.; Sanchez, A. M.; Rajpalke, M. K.; Veal, T. D.; Cao, Y. C.; Li, H. D.; Harvey, R.; Zhuang, Q. D. Optimization of Self-Catalyzed InAs NWs on Flexible Graphite for Photovoltaic Infrared Photodetectors. *Sci. Rep.* **2017**, *7* (December 2016), 46110. https://doi.org/10.1038/srep46110.

(11) Akiyama, T.; Sano, K.; Nakamura, K.; Ito, T. An Empirical Potential Approach to Wurtzite-Zinc blende Polytypism in Group III-V Semiconductor NWs. *Japanese J. Appl. Physics, Part 2 Lett.* **2006**, *45* (8–11). https://doi.org/10.1143/JJAP.45.L275.

(12) Saleem, S.; Maryam, A.; Fatima, K.; Noor, H.; Javed, F.; Asghar, M. Phase Control Growth of InAs NWs by Using Bi Surfactant. *Coatings* **2022**, *12* (2), 250. https://doi.org/10.3390/coatings12020250.

(13) Sun, Q.; Gao, H.; Yao, X.; Zheng, K.; Chen, P.; Lu, W.; Zou, J. Au-Catalysed Free-Standing Wurtzite Structured InAs Nanosheets Grown by Molecular Beam Epitaxy. *Nano Res.* **2019**, *12* (11), 2718–2722. https://doi.org/10.1007/s12274-019-2504-7.

(14) Azimi, Z.; Gopakumar, A.; Ameruddin, A. S.; Li, L.; Truong, T.; Nguyen, H. T.; Tan, H. H.; Jagadish, C.; Wong-Leung, J. Tuning the Crystal Structure and Optical Properties of Selective Area Grown InGaAs NWs. *Nano Res.* **2022**, *15* (4), 3695–3703. https://doi.org/10.1007/s12274-021-3914-x.

(15) Anyebe, E. A.; Kesaria, M. Recent Advances in the Van Der Waals Epitaxy Growth of III-V Semiconductor NWs on Graphene. *Nano Sel.* **2021**, *2* (4), 688–711.

https://doi.org/10.1002/nano.202000142.

(16) Alaskar, Y.; Arafin, S.; Wickramaratne, D.; Zurbuchen, M. A.; He, L.; McKay, J.; Lin, Q.; Goorsky, M. S.; Lake, R. K.; Wang, K. L. Towards van Der Waals Epitaxial Growth of GaAs on Si Using a Graphene Buffer Layer. *Adv. Funct. Mater.* **2014**, *24* (42), 6629–6638. https://doi.org/10.1002/adfm.201400960.

(17) Dayeh, S. A.; Yu, E. T.; Wang, D. III-V Nanowire Growth Mechanism: V/III Ratio and Temperature Effects. *Nano Lett.* **2007**, *7* (8), 2486–2490. https://doi.org/10.1021/nl0712668.

(18) Saraswathy Vilasam, A. G.; Prasanna, P. K.; Yuan, X.; Azimi, Z.; Kremer, F.; Jagadish, C.; Chakraborty, S.; Tan, H. H. Epitaxial Growth of GaAs NWs on Synthetic Mica by Metal–Organic Chemical Vapor Deposition. *ACS Appl. Mater. Interfaces* **2022**, *14* (2), 3395–3403. https://doi.org/10.1021/acsami.1c19236.

(19) Grober, R. D.; Drew, H. D.; Chyi, J. I.; Kalem, S.; Morkoç, H. Infrared Photoluminescence of InAs Epilayers Grown on GaAs and Si Substrates. *J. Appl. Phys.* **1989**, *65* (10), 4079–4081. https://doi.org/10.1063/1.343339.

(20) Li, X.; Walhof, A. C.; Dai, W.; Arslan, I.; Liu, Y.; Toor, F.; Prineas, J. P. Enhanced Radiative and Thermal Properties from Surface Encapsulation of InAs NWs. *Opt. Mater. Express* **2021**, *11* (3), 719. https://doi.org/10.1364/ome.412956.

(21) Gocalinska, A.; Pescaglini, A.; Secco, E.; Mura, E. E.; Thomas, K.; Curran, A.; Gity, F.; Nagle, R.; Schmidt, M.; Michałowski, P. P.; Hurley, P. K.; Povey, I.; Pelucchi, E. Next Generation Low Temperature Polycrystalline Materials for above IC Electronics. High Mobility n- And p-Type III–V Metalorganic Vapour Phase Epitaxy Thin Films on Amorphous Substrates. *JPhys Photonics* 2020, 2, 025003. https://doi.org/10.1088/2515-7647/ab7557.

(22) Curran, A.; Gocalinska, A.; Pescaglini, A.; Secco, E.; Mura, E.; Thomas, K.; Nagle, R. E.; Sheehan, B.; Povey, I. M.; Pelucchi, E.; O'dwyer, C.; Hurley, P. K.; Gity, F. Structural and Electronic Properties of Polycrystalline Inas Thin Films Deposited on Silicon Dioxide and Glass at Temperatures below 500◦c. *Crystals* **2021**, *11* (2), 160. https://doi.org/10.3390/cryst11020160.

Chapter 7

Conclusions and Recommendations

7.1 Conclusions

Overall, this dissertation presents a detailed investigation of the fundamental aspects of epitaxial growth of III-V NWs and thin films on vdW substrates using the MOCVD technique. The research explores both experimental and theoretical approaches to gain a deep understanding of the growth process. By employing vdW epitaxy, this study overcomes the challenges associated with lattice and thermal mismatch typically encountered in heteroepitaxial growth of III-V materials on conventional substrates.

The primary focus of this thesis is the growth of GaAs NWs and InAs NWs, as well as thin film structures, on 2D atomic layered materials such as synthetic mica and h-BN. The interface between the as-grown III-V materials and the vdW substrate is thoroughly examined, and detailed characterisations of morphology, crystal structure, optical properties and electrical properties are performed. One significant achievement highlighted in this thesis is the synthesis of GaAs quantum wires with a record diameter as small as 5 nm. This represents a significant advancement in the field of heteroepitaxial growth of free-standing quantum wires.

In this thesis, successful synthesis of vertical GaAs NWs on synthetic mica substrates using Au-catalysed VLS growth using MOCVD is achieved. The impact of growth parameters, such as temperature and V/III ratio, on the NW yield and the influence of AsH_3 pre-flow on vertical yield are systematically investigated. The resulting NWs

exhibit high optical quality, confirmed by room-temperature PL measurements showing emission at 1.43 eV, corresponding to GaAs band edge emission.

Under optimal growth conditions, the NWs exhibit a ZB crystal structure with occasional stacking faults or inclined twin defects near the base. The NWs have a [111]B polarity. Theoretical investigations using DFT revealed that the bonding between GaAs NWs and mica follows a physisorption-type bonding, unlike the conventional covalent bonding observed with III-V substrates. Importantly, the NWs can be easily detached from the 2D layered mica substrate, making them suitable for flexible device applications. This presents an opportunity to develop NW-based optoelectronic devices that can be epitaxially grown on cost-effective 2D substrates. Additionally, direct growth on transparent substrates like mica allows further exploration of NW arrays, overcoming previous limitations imposed by substrate effects.

Furthermore, synthesis and characterisation of GaAs quantum wires with record dimensions as small as 5 nm in diameter is achieved using VLS growth method. The large-area samples exhibit excellent crystal morphology, with minimal tapering and a pure ZB structure. Lattice constant measurements reveal lattice relaxation in the GaAs quantum wires, with 10 and 20 nm diameter wires exhibiting enhanced negative stress compared to the 5 nm wires.

The electronic structure, surface properties and bandgap characteristics of the GaAs quantum wires are extensively investigated. XPS measurements indicate a shift in core-level binding energy towards higher energies and a narrowing of the valence band as the quantum wire diameter decreases. UPS spectra reveal an increasing work function with decreasing wire diameter, while the bandgap energy shifts towards higher

energies. This comprehensive analysis demonstrates the increased confinement effects and altered electronic properties in GaAs quantum wires with dimensions below the exciton Bohr radius.

Additionally, nanoscale simulations are performed using NextNano simulation software to examine the impact of quantum confinement on optical transition energies in both freestanding quantum wires and quantum wires embedded within an AlGaAs passivation layer. The simulation results demonstrate a more pronounced variation in the bandgap of freestanding quantum wires compared to passivated wires in the AlGaAs structure.

The growth of InAs NWs and thin films on h-BN/SiO_2/Si vdW substrates without the need for catalysts or surface modifications is studied systematically. By adjusting the growth temperature and V/III ratio, a high density of NWs ($2x10^9$ /cm^2) is achieved. The NWs exhibit a mixed WZ and ZB phase.

To achieve uniform InAs thin films on h-BN/SiO_2/Si, a growth strategy is implemented to suppress NW growth and promote radial growth of nano-islands on the h-BN surface. The influence of growth parameters, specifically temperature and V/III ratio, on surface morphology, structural properties and optical properties of the InAs thin films is investigated. It was found that the growth temperature has a significant impact on structural properties, while the V/III ratio has a minor effect.

Analysis using cross-sectional TEM and XRD study reveals a predominantly [111]-oriented ZB structure in the thin films. The redshift observed in photoluminescence is attributed to tensile strain induced by the mismatch in thermal expansion coefficients between h-BN and InAs thin films. The vdW nature of the interface is confirmed by the

absence of threading dislocations extending to the film's top in the TEM and GPA analysis.

The uniform coverage of polycrystalline InAs thin films, combined with room temperature photoluminescence and relatively high Hall mobility (399 $cm^2/(Vs)$), demonstrates the potential for large-area, low-temperature growth of III-V thin films directly on vdW substrates using MOCVD.

This research establishes a promising approach for achieving high-quality epitaxial growth of III-V materials on vdW substrates, paving the way for future device applications.

Overall, this thesis has added an in depth experimental and theoretical understanding of III-V epitaxial growth on 2D material templates along with systematic study on the material characterisations and analysis of the as-grown III-V materials. The findings serve as a foundation for experimental growth and characterisation of III-V NW and planar structures on 2D templates providing valuable insights for future research in this field. Moreover, the synthesis of GaAs quantum wires of record dimensions down to 5 nm diameter beckons more fundamental research in to their properties in order to understand their true potential in various applications.

Contributions:

- The thesis successfully demonstrates vdWE of GaAs NWs on synthetic mica using the VLS growth technique through a systematic exploration of various growth parameters.

  It also shows that the NWs can be readily peeled off from the 2D layered mica substrate, indicating their suitability for flexible device applications. This finding opens avenues

for the development of NW-based optoelectronic devices grown epitaxially on cost-effective 2D substrate materials.

- The thesis demonstrates the synthesis of GaAs quantum wires with record dimensions down to 5 nm diameter via gold seeded VLS growth technique on synthetic mica using MOCVD. The wires exhibit exceptional crystal morphology and pure zinc blende structure.

- Through careful tuning of the growth parameters and identifying a balance between nanowires and nanoisland growth, the thesis demonstrates a viable approach to achieving large-area thin film growth of InAs on 2D h-BN on SiO_2 substrates, laying a foundation for future device applications on CMOS compatible Si or SiO_2 substrates using h-BN as a sacrificial layer.

7.2 Recommendations for future research

The primary objective of this thesis is to advance the development and understanding of vdW epitaxy of III-V materials on 2D templates using the MOCVD technique, with a focus on their application in flexible optoelectronic devices.

Through a combination of experimental and theoretical investigations, this research has successfully achieved a high yield of vertically aligned NWs with exceptional morphological, structural, and optical properties over a large area. The next phase of the study involves exploring the growth of axial and vertical heterostructures with doping and quantum well/dot structures on 2D templates that can be easily peeled off after growth or after device fabrication, enabling the realisation of truly flexible optoelectronic devices.

Building upon the successful growth strategy for polycrystalline InAs thin films, a future investigation to expand the study to grow high-quality epitaxial layers suitable

for various optoelectronic applications is desirable. This could be done using the thin film growth strategy detailed in chapter 6 to achieve the first buffer layer and growing subsequent layers at higher temperatures and lower growth rates to achieve smooth morphology thin film. Once considerable quality epilayers are achieved, multi junction devices, thin film quantum well based devices could be epitaxially grown and peeled off after device fabrication step.

Furthermore, the quantum wires synthesised on synthetic mica provide a platform for exploring fundamental physics concepts, such as direct-to-indirect bandgap transition at a certain diameter threshold. NWs could be grown using Au particles size ranging from 2nm onwards. Surface sensitive work function study using scanning tunnelling microscopy or scanning kelvin probe microscopy could be performed to understand the electronic confinement effects on the band structure. Additionally, these quantum wires hold potential for indoor sensing applications. For this however, effective doping and device fabrication on such small dimensional NWs should be explored.

In summary, this thesis focuses on the development and understanding of vdW epitaxy for III-V materials on 2D templates using the MOCVD technique, with an emphasis on flexible optoelectronic device applications. The research has achieved remarkable results in growing vertically aligned nanowires and seeks to explore the growth of heterostructures, epitaxial layers and ultra-thin quantum wires for further advancements in the field.